UNIVERSITY OF COPENHAGEN
FACULTY OF SCIENCE

Morten Sales

Niels Bohr Institute

Development of Instrumentation for Spin-Echo Induced Spatial Beam Modulations

for Small Angle Scattering Investigations

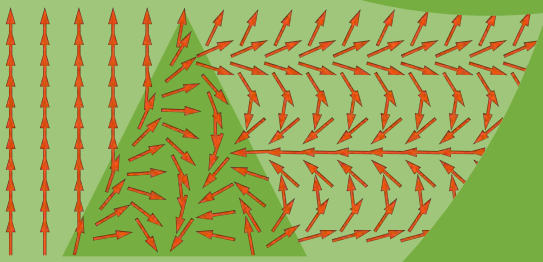

Supervisors: Kim Lefmann[1],
Klaus Habicht[2], and Markus Strobl[1,3]
[1]University of Copenhagen
[2]Helmholtz-Zentrum Berlin
[3]European Spallation Source

Sometimes, if you pay real close attention to the pebbles
you find out about the ocean
-Terry Pratchett

Acknowledgements

A grateful thank you is owed to my three supervisors, Kim Lefmann from the University of Copenhagen, Klaus Habicht from Helmholtz-Zentrum Berlin, and Markus Strobl from the European Spallation Source. They have guided and supported me from start to finish. Thank you for the valuable advise and aid you have given me.

The main experimental work for this thesis has been performed at the TUDelft, and would not have been possible without Jeroen Plomp, Wim Bouwman and Catherine Pappas. I am very thankful for the beamtime we have had at the Reactor Institute Delft at TUDelft. The hard work and experience of Jeroen has guaranteed the success of the experiments, and the knowledge of Wim has been invaluable in many aspects including analysis and modelling of the data. Which brings me to thank Anton Tremsin from the University of California, Berkeley, for without his unique detector we could never have measured what we set out to do.

Lastly, a big thank you is owed to all of my collaborators and colleagues, who have not only helped me professionally but also been there as motivators and friends.

This research project has been supported by the European Commission under the 7th Framework Programme through the 'Research Infrastructures' action of the 'Capacities' Programme, NMI3-II Grant number 283883.

Abstract

English

Spin-Echo Modulated Small Angle Neutron Scattering in Time-of-Flight mode (ToF SEMSANS) is an emerging technique extending the measurable phase space covered by neutron scattering. Using inclined magnetic field surfaces, (very) small angle scattering from a sample can be mapped into the spin orientation of the neutron as it has been shown in Spin-Echo Small Angle Neutron Scattering (SESANS). Taking this technique further we have shown that it is possible to perform quantitative Dark-Field Imaging, where the small angle scattering signal of individual areas in a neutron image can be obtained. This was done by using triangular shaped magnetic fields to create a spatially modulated beam after the spin analyser, and mapping the small angle scattering signal into a dampening of the amplitude of the beam modulation.

The first progress we made was to construct the SEMSANS instrument at the Reactor Institute Delft, TUDelft, and resolve the modulation using absorption gratings in front of a detector without spatial resolution, i.e. a simple counting detector. Combining this with a virtual copy of the instrument, built using the Monte Carlo Ray-Tracing simulation package McStas, we were able to expand our investigations beyond the instrumental limitations at the time in order to examine the effect of restoring the Spin-Echo condition.

The next step in our investigation was to use a position and time sensitive detector in order to directly record the spatial modulation for each wavelength in the neutron pulse. We then successfully recorded neutron images for a multi-sample set-up where we for each sample extracted the small angle scattering curve and observed that they were consistent with the theoretical models.

We thereafter developed a novel method for analysis of SEMSANS data and used it to show that the spatial resolution can be improved using the new method and that it is less computational heavy and hence time consuming.

And lastly we took the instrumental setup a step further by ramping the magnetic fields in the triangular coils in synchronisation with the neutron pulse such that the modulation period could become constant with neutron wavelength, which would open up the possibility of using

absorption gratings to achieve sub detector pixel spatial resolution even in Time-of-Flight mode, which is required in order to exploit the most powerful neutron sources.

The combination of our investigations has shown that SEMSANS can be a technique covering areas of investigation hitherto unreachable with neutron scattering, potentially providing a powerful new method for investigating a large range of length scales simultaneously by combining neutron imaging with (very) small angle scattering investigations through the use of Spin-Echo induced spatial modulation.

Danish

Spin-Ekko Moduleret Små-Vinkel Neutron Spredning i Flyvetids-opsætning (ToF SEMSANS) er en fremvoksende teknik, som udvider det parameterrum, der kan måles med neutronspredning. Ved brug af skrå magnetfeldtsoverflader kan man overføre informationen fra spredning i (meget) små vinkler, til orienteringen af neutronens spin, sådan som det er blevet påvist med Spin-Ekko Små-Vinkel Spredning (SESANS). Vi har videreført denne teknik til at vise, at det er muligt at udføre kvantitativ "Dark-Field-afbildning, hvor man kan måle små-vinkel spredningssignalet i individuelle områder fra et neutron-billede. Dette blev

gjort ved brug af magnetfelter i trekant-formede områder. Dette skabte en rumligt moduleret neutronstråle efter spin-analysatoren og overfører information fra små-vinkel spredningsignalet til en dæmpning af amplituden af den modulerede neutronstråle.

Det første vi gjorde, var at opbygge SEMSANS instrumentet på Reactor Institute Delft, TUDelft, og måle strålemoduleringen ved hjælp af absorptionsgitre foran en detektor uden rumlig opløsning. Dette blev kombineret med en virtuel udgave af instrumentet, opbygget ved brug af Monte-Carlo Ray-Tracing pakken McStas, hvor vi var i stand til at udvide vores undersøgelser udover de dengang instrumentelle begrænsninger, for på den måde at undersøge effekten af at bibeholde Spin-Ekko betingelsen.

Det næste skridt i vores undersøgelse var at bruge en på en gang tid- og rum-sensitiv detektor for direkte at kunne måle den rumlige modulering for hver enkelt bølgelængde i neutronpulsen. Derefter optog vi med succes neutron-billeder af et multi-prøve set-up, hvor vi uddrog små-vinkel spredningskurverne for hver enkelt prøve og observerede deres overensstemmelse med teoretiske modeller.

Derefter udviklede vi en metode til at analysere SEMSANS data og brugte den til at vise, at den rumlige opløsning kan forbedres ved brug af denne metode, og at den

kræver mindre regnekraft og derfor er mindre tidskrævende.

Til sidst tog vi det instrumentelle set-up et skridt videre ved at variere de magnetiske felter i de trekantede spoler synkroniseret med neutronpulsen, således at moduleringsperioden blev konstant i forhold til bølgelængden. Dette vil åbne op mulighed for at bruge absorptionsgitre til at opnå rumlig opløsning bedre en detektorens begræsning selv i flyvetids-opsætning, hvilket er nødvendigt for at udnytte de mest kraftfulde neutronkilder.

Kombinationen af vores undersøgelser har vist at SEMSANS kan være en teknik, der afdækker undersøgelsesområder, hidtil uopnåelige med neutronspredning. Dette kan potentielt levere en ny kraftfuld metode for samtidig undersøgelse af et bredt interval af længedeskalaer ved at kombinere neutron-afbilding med måling af spredning i (meget) små vinkler med Spin-Ekko induceret rumlig modulering.

Contents

List of Figures

Chapter 1

Introduction

The goal of the work described in this thesis has been to develop novel neutron scattering instrumentation useful for the investigation of sample types and/or properties in ways that have so far not been possible and to improve or expand the uses of conventional methods. Specifically, the use of Spin-Echo induced spatial beam modulation in Time-of-Flight mode has been investigated for (i) measuring (very) Small Angle Scattering possibly from magnetic samples and/or samples in magnetic sample environment and (ii) quantitative Dark-Field Imaging.

One of the strengths of using neutrons is their deep penetration depth, allowing them to probe not just surface properties, but the bulk of large samples and samples contained in complex sample environment. Moreover, neu-

trons can interact with light elements that are invisible to X-rays, and because of the magnetic moment of the neutron, they are sensible to magnetic sample properties. With contrast matching, where the "neutron-visibility" of different sample components can be enhanced, neutrons are a powerful probe for investigating organic matter in aqueous solution.

All this makes neutron scattering a well suited probe for a wide variety of non-destructive investigations of the structure matter from angstrom up to micrometre length scales. However, with conventional neutron scattering, the change in the velocity of a scattered neutron is determined by very precise measurements of the neutron scattering angles. This is limited by the divergence and the definition of the neutron beam. To overcome this constraint and thereby expand the usable range of neutron scattering even further, techniques using magnetic fields to encode scattering information into the orientation of the neutron spin, were first envisioned by Mezei in 1972 [28]. These methods have since been further developed from the studies of dynamics to more recently also cover elastic measurements such as very small angle scattering.

Spin-Echo Small Angle Neutron Scattering (SESANS) [36], opened up the possibility of measuring (very) small angle scattering from structures in the micrometre range, by encoding the small neutron scattering angle into the

polarisation of the neutron beam, by the use of inclined field surfaces, such that smaller scattering angles can be resolved. We have investigated a technique expanding upon SESANS, where the scattering information is further mapped from precession angles into an amplitude dampening of spatially modulated neutron beam. In this Spin-Echo Modulated Small Angle Neutron Scattering (SEMSANS) technique all spin manipulation can be performed before the sample such that depolarising effects from a magnetic sample and/or magnetic sample environment will not reduce the signal by depolarising the beam, which makes it possible for straight forward investigation of magnetic structures in the nanometre and micrometre range. Our technique utilises a pulsed polychromatic neutron beam, such that all wavelengths are used, and since the length scale probed scales with the wavelength, the entire (very) small angle scattering curve can be investigated without varying parameters in the instrumental set-up. Because of the way the small angle scattering signal is encoded in the spatial information we can with our technique extract small angle scattering signal for individual areas of a neutron neutron image. Such quantitative Dark-Field Imaging can be used to bridge the gap between small angle scattering and imaging, measuring both simultaneously, thereby covering length scales at several orders of magnitude in one measurement. To decouple the resolution from that

of the detector, we have sought to keep the spatial modulation period constant such that an absorption grating analyser can be used.

1.1 On this text

The following chapter introduces the relevant concepts in neutron scattering and then specifically presents the important Spin-Echo techniques. This leads up to the main part of this thesis, which is based on four articles presented in Chapters 3 to 6.

Chapter 3: "Investigating Time-of-Flight Spin Echo Modulation for Small Angle Neutron Scattering through experiments and simulation" describes the first experiments, where we investigated the instrumental capabilities of our Spin-Echo Modulated Small Angle Neutron Scattering (SEMSANS) set-up, measuring the spatially modulated beam using an absorption grating and a single-pixel time sensitive detector. Furthermore we build a virtual copy of the set-up using Monte-Carlo ray tracing software in order to expand our investigation beyond the limitations of the real set-up at the time.

In Chapter 4: "Quantitative Neutron Dark-field Imaging through Spin-Echo Interferometry" we take our investigations further, with the use of a both position and time

sensitive detector measuring the modulation directly, and giving us the opportunity to measure small angle scattering from a multi-sample set-up and compare the results to reference curves.

Chapter 5: "A Pixel Based Approach for Spatially Resolved Analysis of Time-of-Flight Spin-Echo Modulated Scattering Data" goes into detail with describing the data analysis of SEMSANS data, where we introduce a novel approach to the analysis, explaining its strengths and potential drawbacks and comparing it to the conventional methods.

Chapter 6: "Wavelength-Independent Constant Period Spin-Echo Modulated Small Angle Neutron Scattering" describes our pursuit in taking the SEMSANS instrumental set-up even further using ramped magnetic fields to keep the modulation period constant for all wavelengths, such that spatial resolutions higher than the detector limit can be obtained.

In each of the article-based chapters there are grey boxes with extra information adding to the article text. Additionally the figures have been altered to fit the common layout of this thesis and the article citations now refer to a common reference list. A few words and symbols have been changed as well so the articles use the same terminology and nomenclature.

The first three appendices each contain an article that has been part of my research but were beyond the scope of this thesis. The first describing investigations of remanent magnetisation in hemo-ilmenite and the following two reporting the results of simulations of instruments at long pulsed sources in order to optimise the time structure of the neutron pulse from a spallation source. The last appendix contains computer code relevant especially to Chapter 3.

This PhD has been a project in collaboration between the University of Copenhagen, Helmholtz-Zentrum Berlin, and the European Spallation Source with me being enrolled at the KU PhD school and employed for three years at HZB.

Chapter 2

Introduction to Neutron Scattering

This chapter introduces the basics principles and the theory behind using neutrons as a probe for studying structures with angstrom and nanoscale features.

2.1 Neutron properties and production

The neutron was discovered in 1932 and it is one on the most common particles in existence. Together with the proton it is what makes up the nuclei of mostly all atoms. It has a rest mass of $m_N = 1.675 \cdot 10^{-27}$ kg, it is charge neutral and it has a magnetic moment of $\mu = \gamma\mu_N =$

$\gamma e\hbar/(2m_p) = -1.913 \cdot 5.051 \cdot 10^{-27}$ J/T, with the direction of the magnetic moment defined by the neutron's spin vector.

Neutrons for scattering can be produced in several ways. They can be produced by radioactive decays in laboratory sources, e.g a Radium-Beryllium source. However, such a source is not powerful enough to produce the amount of neutrons needed for most scattering studies, so stronger sources are needed for these purposes. Experimental reactor sources produce neutrons in high amounts from controlled nuclear reactions in for example radioactive uranium. These sources demands a lot of security measures and maintaining, and facilities producing neutrons by fission are large with many users and applications. Another way to produce neutrons at high flux (neutrons/second/cm^2) is through spallation where protons are accelerated into a dense target wherein highly excited nuclei are created, subsequently decaying and in the process sending out a burst of nuclei.

Common for the different neutron production methods described above is that the resulting neutrons have too high energies and are unsuited for scattering purposes. Therefore a moderation of the neutrons is needed. This is done by surrounding the neutrons with moderating material such as water or liquid hydrogen. Within this material

the neutrons bounce around and are being slowed down by giving off energy to the atoms in the moderator.

In quantum mechanics particle-wave duality gives a relationship between the energy, E, and wavelength, λ, of a particle moving with constant velocity. The so-called de-Broglie wavelength is given by:

$$\lambda = \frac{h}{m_N v} , \tag{2.1}$$

where $h = 6.626 \cdot 10^{-34}$ Js is the Planck constant and v is the neutron velocity. The wave number is $k = 2\pi/\lambda$ and from this we get the energy (using the energy-momentum relation $E = p^2/(2m_N)$ and $\hbar = h/(2\pi)$):

$$E = \frac{\hbar^2 k^2}{2m_N} . \tag{2.2}$$

So by moderating the neutrons to lower energies we get neutrons with larger wavelengths. When investigating matter on length scales in the angstrom and nanometer range, neutron scattering can be a powerful tool. One of the reasons for this is that the wavelength of neutrons moderated at room temperature or lower temperatures is of the same order as the length scales investigated.

2.2 Scattering

Waves interact with matter through scattering, and the basic principle of neutron scattering is that by directing a neutron beam at a sample and measuring how the neutrons scatter, knowledge of the inner workings of the sample can be obtained. In basic neutron scattering, the neutrons interact with the nuclei of the sample through the strong nuclear force.

The description of neutron scattering in this chapter is based on the description in [21].

The magnitude of an incoming neutron beam can be described by the aforementioned flux, which is the number of neutrons on a given surface area perpendicular to the incoming neutron beam within a given time. The flux is denoted by Ψ. Neutron scattering works because different structures and materials scatter neutrons at different strength, and this is quantified by the neutron scattering cross section which can be visualised as the effective area of the the scattering nuclei 'seen' by the incoming neutron. It is given by:

$$\sigma = \frac{1}{\Psi} \left(\#\text{ of neutrons scattered per second}\right). \tag{2.3}$$

Knowing the direction of the scattered neutron is essential to neutron scattering and this is described by the differen-

tial cross section:

$$\frac{\mathrm{d}\sigma}{\mathrm{d}\Omega} = \frac{1}{\Psi}\frac{\left(\begin{smallmatrix}\text{\# of neutrons scattered}\\ \text{per sec. into solid angle d}\Omega\end{smallmatrix}\right)}{\mathrm{d}\Omega} \,. \tag{2.4}$$

In inelastic neutron scatting the incoming and the outgoing neutrons have different energies and it is necessary to describe the change in energy as well. This is done by the partial differential cross section:

$$\frac{\mathrm{d}^2\sigma}{\mathrm{d}\Omega dE_f} = \frac{1}{\Psi}\frac{\left(\begin{smallmatrix}\text{\# of neutrons scattered per sec. in}\\ \text{d}\Omega \text{ with energies } [E_f; E_f + dE_f]\end{smallmatrix}\right)}{\mathrm{d}\Omega \mathrm{d}E_f} \,, \tag{2.5}$$

where E_f is the energy of the outgoing scattered neutron.

2.2.1 Wave description of scattering

The incoming neutron can be described as a plane wave with wavevector $\mathbf{k}_i$:

$$\psi_i(\mathbf{r}) = \exp(i\mathbf{k}_i \cdot \mathbf{r}) \,, \tag{2.6}$$

where the normalisation constant is omitted for simplicity. From eq. (2.1) we get the speed of the plane wave, and

from this we get the flux of incoming neutrons:

$$v = \frac{\hbar k_i}{m_N} \tag{2.7}$$

$$\Psi_i = |\psi_i|^2 v = v \; . \tag{2.8}$$

The plane wave hits a fixed nucleus at the origin and is scattered as a spherically symmetrical wave:

$$\psi_f(\mathbf{r}) = \frac{-b}{\mathbf{r}} \exp(ik_f \mathbf{r}) \; , \tag{2.9}$$

where b is the the scattering length, which varies from isotope to isotope. The density of outgoing neutrons is:

$$|\psi_f|^2 = \left(\frac{b}{r}\right)^2 \; . \tag{2.10}$$

The number of outgoing neutrons passing through a small area, $\mathrm{d}A$, is $v|\psi_f|^2 \mathrm{d}A$ and the solid angle is given by $\mathrm{d}\Omega = \mathrm{d}A/r^2$. Now the differential cross section can be written as (2.11), since the nucleus is assumed to be fixed and therefore the neutron wave number (and energy) is preserved:

$$\frac{\mathrm{d}\sigma}{\mathrm{d}\Omega} = \frac{v b^2 \mathrm{d}\Omega}{\Psi_i \mathrm{d}\Omega} = b^2 \; . \tag{2.11}$$

A single nucleus scatters in all directions, and it therefore has the total scattering cross-section:

$$\sigma = 4\pi b^2 \,. \tag{2.12}$$

2.3 Diffraction

Neutron diffraction deals with elastic scattering, which describes the process where the neutron has the same energy going in to as coming out of the scattering event.

2.3.1 Scattering by several nuclei

In a real experiment, the samples investigated are composed of many nuclei, from which the scattered neutron waves interact in ways that can be measured and used to obtain knowledge on the inner structure of the sample.

Consider two identical nuclei at positions r_j and $r_{j'}$, being hit by a incoming plane wave $\psi_i(\mathbf{r})$. the outgoing wave is then:

$$\psi_f(\mathbf{r}) = -b\Bigg(\frac{\psi_i(\mathbf{r}_j)}{|\mathbf{r}-\mathbf{r}_j|}\exp(ik_f|\mathbf{r}-\mathbf{r}_j|)+ \tag{2.13}$$

$$\frac{\psi_i(\mathbf{r}_{j'})}{|\mathbf{r}-\mathbf{r}_{j'}|}\exp(ik_f|\mathbf{r}-\mathbf{r}_{j'}|)\Bigg) \,. \tag{2.14}$$

Choosing an origin close to the nuclei, an observer far away compared to nuclei distance ($|\mathbf{r} - \mathbf{r}_j| \ll r$) so that the denominators can be considered equal, and using (2.6), we get:

$$\psi_f(\mathbf{r}) = \frac{-b}{r}\Big[\exp(i\mathbf{k}_i \cdot \mathbf{r}_j)\exp(ik_f|\mathbf{r} - \mathbf{r}_j|) + \tag{2.15}$$

$$\exp(i\mathbf{k}_i \cdot \mathbf{r}_{j'})\exp(ik_f|\mathbf{r} - \mathbf{r}_{j'}|)\Big]\,. \tag{2.16}$$

Separating the nuclei co-ordinates into components parallel and perpendicular to $\mathbf{r}$ and using Pythagoras' theorem, we get $|\mathbf{r} - \mathbf{r}_j| = \sqrt{|\mathbf{r} - \mathbf{r}_{j\parallel}|^2 + |\mathbf{r}_{j\perp}|^2}$, where the second term in the square root can be left out, since it is insignificant compared to the neutron wavelength. This gives us:

$$k_f|\mathbf{r} - \mathbf{r}_j| = \mathbf{k}_f \cdot (\mathbf{r} - \mathbf{r}_{j\parallel}) = \mathbf{k}_f(\mathbf{r} - \mathbf{r}_j)\,, \tag{2.17}$$

where the wavevector $\mathbf{k}_f$ is parallel to $\mathbf{r}$. The outgoing wave can now be written as:

$$\psi_f(\mathbf{r}) = \frac{-b}{r}\exp(i\mathbf{k}_f \cdot \mathbf{r})\Big[\exp(i(\mathbf{k}_i - \mathbf{k}_f) \cdot \mathbf{r}_j) + \tag{2.18}$$

$$\exp(i(\mathbf{k}_i - \mathbf{k}_f) \cdot \mathbf{r}_{j'})\Big]\,. \tag{2.19}$$

As in (2.11), we can now calculate the differential cross-section to be:

$$\frac{\mathrm{d}\sigma}{\mathrm{d}\Omega} = b^2 |\exp(i\mathbf{q}\cdot\mathbf{r}_j) + \exp(i\mathbf{q}\cdot\mathbf{r}_{j'})|^2 \tag{2.20}$$

$$= 2b^2[1 + \cos(\mathbf{q}\cdot(\mathbf{r}_j - \mathbf{r}_{j'}))] \,, \tag{2.21}$$

where the scattering vector $\mathbf{q}$ is defined as:

$$\mathbf{q} \equiv \mathbf{k}_i - \mathbf{k}_f \,. \tag{2.22}$$

It can be seen that for some values of $\mathbf{q}$ the cosine term becomes 1, and differential cross section is then four times larger than for a single nucleus, see (2.11). For other $\mathbf{q}$-values the differential cross section completely vanishes. This is the effect of interference between waves from multiple scatterers. For more than just two scatterers, with possibly different scattering lengths, the elastic differential cross-sections is:

$$\frac{\mathrm{d}\sigma}{\mathrm{d}\Omega} = \left| \sum_j b_j \exp(i\mathbf{q}\cdot\mathbf{r}_j) \right|^2 \,. \tag{2.23}$$

2.3.2 Bragg's Law

Consider a number of nuclei arranged in a periodic structure. A plane wave hits the structure and in a certain direction there is constructive interference. The distance

between the atomic layers is d. The wavelength of the neutron wave is λ, and it enters at an angle, θ, with respect to the atomic planes. The neutron ray taking the path where it is being reflected by the second layer, has a travelled a distance $2d \sin\theta$ longer, and if this path length difference is equal to a whole number, n, of wavelengths, constructive interference will occur [5, 31]. This is the principle of Bragg's Law:

$$n\lambda = 2d \sin\theta \tag{2.24}$$

What this means is that by measuring a sample consisting of periodically arranged scatterers and varying θ and λ you can find the values that result in constructive interference, and from this calculate the characteristic distances, d, in the sample. This is illustrated in Fig. 2.1, *top*.

2.4 Small Angle Scattering

In small angle scattering we deal with length scales larger than atomic distances and in such cases the scattering vector, q, becomes small enough compared to the interatomic structure size, a, so that the condition

$$qa \ll 2\pi \tag{2.25}$$

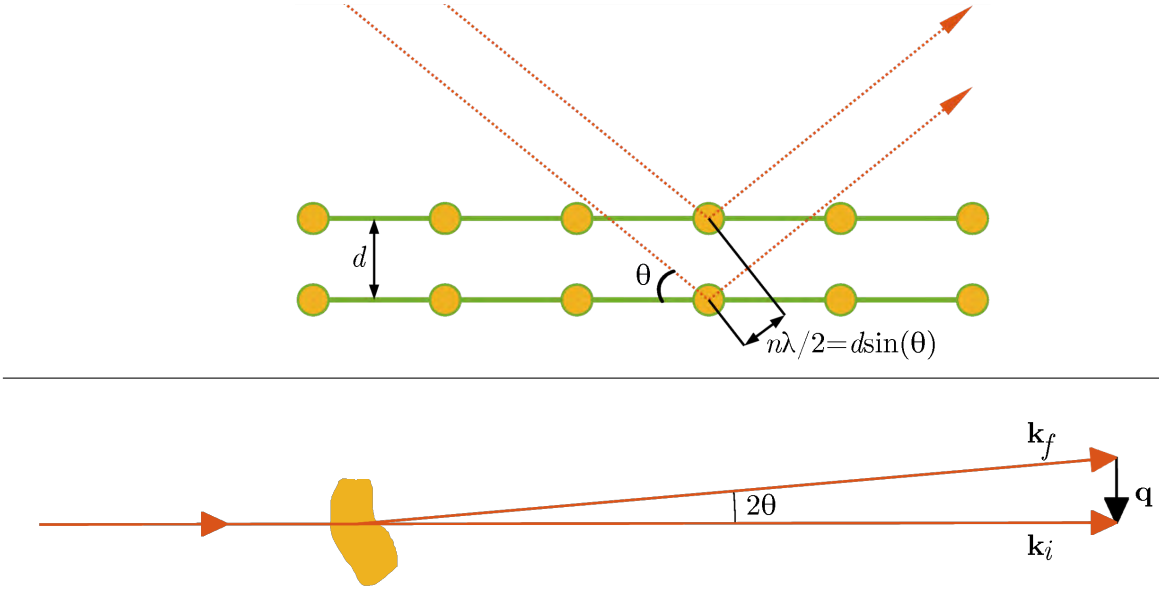

Figure 2.1 *top*, illustration of Bragg's Law, $n\lambda = 2d \sin\theta$, describing the diffraction of short waves by a crystal. The length of the path taken by the ray diffracting off the bottom atomic layer has to be an integral number of wavelengths longer than the upper path in order for constructive interference to occur. *bottom*, in conventional Small Angle Neutron Scattering measurements the incoming neutron beam has to be controlled very precisely in order to resolve the scattering angle, which is of the order of a few degrees.

is met. Given this, the sum in eq. (2.23) can be transformed into an integral over the sample volume as scattering from individual nuclei is indistinguishable. With N nano-sized objects in the sample, the location of each scatterer can be expressed by the sum of its location in the nano-sized object and the location of the object itself: $\mathbf{r'}_j = \mathbf{r}_j + \mathbf{R}_J$ [21]:

$$\frac{\mathrm{d}\sigma}{\mathrm{d}\Omega} = \left| \sum_J \exp(i\mathbf{q} \cdot \mathbf{R}_J) \right|^2 \left| \int_V \rho_b \exp(i\mathbf{q} \cdot \mathbf{r}) \mathrm{d}V \right|^2 \tag{2.26}$$

$$= N \left| S(\mathbf{q}) \right|^2 \left| \int_V \rho_b \exp(i\mathbf{q} \cdot \mathbf{r}) \mathrm{d}V \right|^2 . \tag{2.27}$$

For random dilute systems, the structure factor, $S(\mathbf{q})$, is equal to one (see also Chapter 4 where the hard-sphere structure factor has been taken into account). ρ_b is the scattering length density, defined as the sum of scattering lengths, b, in a formula unit of the sample material, divided by the volume of the unit. It can be seen that it is inhomogeneities in ρ_b that give rise to small angle scattering. Very small angle scattering is when the size of the scattering structures in the sample are so large that the scattering angles becomes so small that they can be difficult to measure with conventional SANS instruments. Here, the scattering angles are resolved by having very precise, highly collimated neutrons beams, in order the reduce the uncertainty of the measured scattering angle (see Fig. 2.1, *bottom*).

2.5 Imaging

Basic neutron imaging, called radiography, measures the attenuation of a neutron beam passing through a sample with spatial resolution. This provides real-space information on the macroscopic structure of the sample [45]. As the neutrons pass through the sample, the beam is attenuated by neutrons being absorbed or scattered such that transmitted intensity after the sample is reduced compared to the incident intensity.

$$I(x,y,E)_T = I(x,y,E)_I \exp\left[-\int \mu(x,y,z,E)\mathrm{d}s\right] \ , \quad (2.28)$$

the neutrons travel along z and for each (x,y) position of the neutrons passing through the sample, and each energy, E, of the neutrons, there is an attenuation of the intensity, the extend of which is governed by the integral of the attenuation coefficient over the path of the neutron, s, through the sample. The total attenuation coefficient, μ, is the sum of the absorption and scattering coefficients: $\mu = \mu_A + \mu_S$, and varies between different elements and isotopes. The spatial resolution of a neutron imaging set-up is generally in the order of 10 μm-100 μm [25]. An overview of a radiography set-up is shown in Fig. 2.2, *left*.

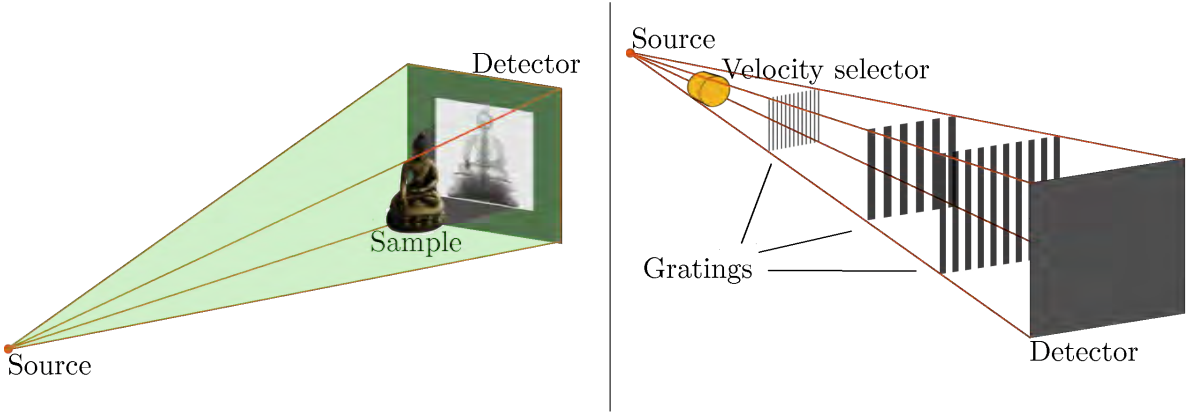

Figure 2.2 *left*, radiography set-up. The difference of attenuation in the different sample components result in a shadow image on the detector. (Neutron image from [24]). *right*, grating interferometry set-up, where gratings are used to extract the small-angle scattering information from different parts of the sample.

2.5.1 Dark Field Imaging

In Dark Field Imaging (DFI) the signal from the scattered neutrons is isolated in order the measure small angle scattering from the sample. This can be done using a grating interferometer [32, 43], where a diffraction grating "splits" the neutrons from individually coherent "sources", created by an absorption grating upstream, into a periodic interference pattern such that at specific distances from the grating a spatially modulated beam with a specific period arises. Since the period is below what neutron detectors can resolve, this is measured by scanning a third grating transversely across the neutron beam. See Fig. 2.2, *right*, for a depiction of a grating interferometer.

For small angle scattering the scattering angle, θ_S, can also be expressed as a position shift perpendicular to the incoming neutron beam, x, of the scattered neutron at a distance, L_S, further downstream [43]:

$$\theta_S \sim \frac{x}{L_S} \,. \tag{2.29}$$

Therefore, the result of small angle scattering will smear out the modulation of the beam, thereby reducing the modulation amplitude. By measuring the visibility, V:

$$V = \frac{I_{\max} - I_{\min}}{I_{\max} + I_{\min}} \,, \tag{2.30}$$

and normalising with the empty beam visibility measurement, the recorded signal can be modelled in the same way as in Spin-Echo Small Angle Scattering (see section 2.4).

The method requires monochromatic neutrons with a relatively relaxed wavelength resolution of the order of $\delta\lambda/\lambda \sim 10\%$.

2.6 Time-of-Flight neutron scattering

In neutron scattering it is in general necessary to know the wavelength of the neutron (which is related to the neutron speed and energy through eqs. (2.1) and (2.2)). One way to do this is to use a pulsed neutron source such as a pulsed spallation source, or to cut the neutron beam of a continuous source into pulses (see sec. 2.8.1). By measuring the Time-of-Flight (ToF) it takes a neutron to travel a given distance, L, one can calculate the neutron wavelength:

$$t_{\mathrm{ToF}} = \alpha L \lambda \ , \tag{2.31}$$

where $\alpha = m_N/h = 2.528 \times 10^{-4}$ s/m/Å.

This was used to calculate the wavelengths from the ToF in Chapter 4, where we first inserted a polycrystalline beryllium filter into the beam. The attenuation due to scattering of neutrons passing through such a filter, where the crystal planes are randomly oriented, is strongly depen-

dent on wavelength, as Bragg's Law, (eq. (2.24)), for a given atomic plane distance can no longer be fulfilled above a certain neutron wavelength corresponding to a Bragg angle of $\theta = 180^\circ$. The result is that the filter will have much higher transmittance for wavelengths above this so-called Bragg edge. For Beryllium this Bragg edge is located at 3.97 Å, which is indicated in Fig. 2.3 **a**, where the measured Intensity vs ToF with the Beryllium filter in the beam is shown. The time-location of Beryllium Bragg edge was found and using eqs. (2.1) and (2.31), the wavelength can be calculated from the ToF data with an unknown time offset. The obtained wavelength spectrum in Fig. 2.3 **b** matches well with a previously recorded reference spectrum of the same neutron source.

2.7 Spin-Echo techniques

As described in section 2.1, the neutron has a magnetic moment, with the direction defined by the spin. The idea of neutron spin-echo techniques is to map scattering information into the orientation of these magnetic moments, so that by measuring the polarisation of the neutron beam one can obtain knowledge of the structure and/or dynamics of the probed sample [28, 29].

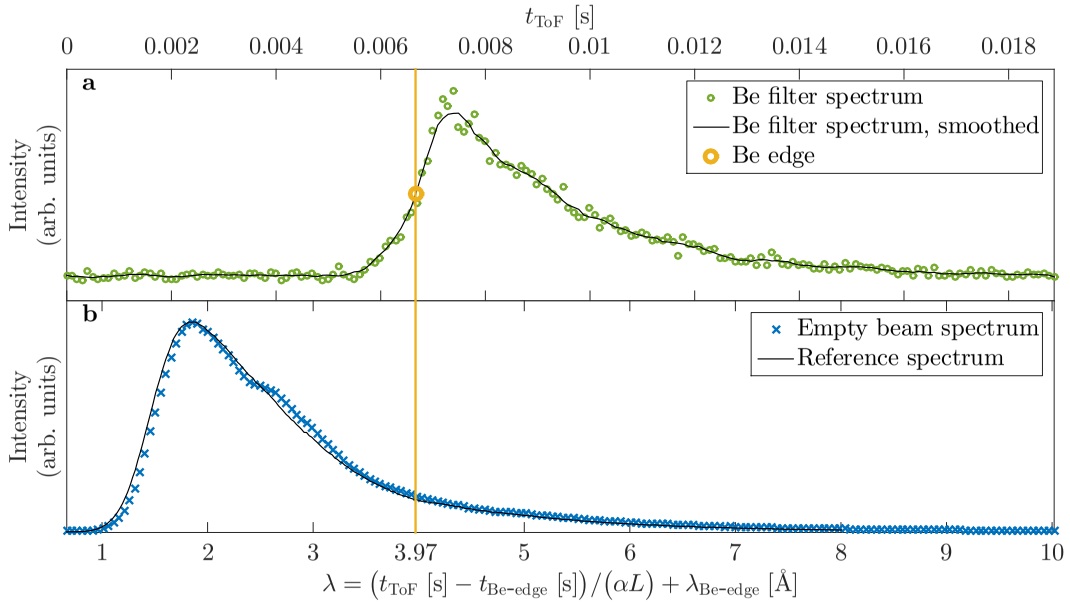

Figure 2.3 (Used for data treatment in Chapter 4). In a ToF experiment with an unknown time offset, a Beryllium filter is used to calculate the wavelengths from the recorded ToFs, since the wavelength for the Bragg edge of the Beryllium filter is well known (**a**). **b** shows the recorded wavelength spectrum. Distance from pulse-creating choppers to detector, L, was 7.98 m.

Moving through an external magnetic field, the neutron spin will Larmor precess, and the final precession angle gained after exiting the field will be proportional to the magnetic field strength and the time spent in the field by the neutron:

$$\phi_I = c\lambda BL \,, \tag{2.32}$$

where ϕ_I is the precession angle, λ is the neutron wavelength, B is the strength of the magnetic field, and $c = 4.632 \times 10^{14}\ \mathrm{T^{-1}m^{-2}}$ is the Larmor constant. Having a second identical magnetic field area with the field in the opposite direction of the first, will effectively reverse the effect of the first field and return neutrons of all wavelengths to their initial spin orientation, thereby achieving the so-called Spin-Echo. This can also be accomplished by having the two fields symmetric in the same direction and flipping the neutrons 180° in between them. If a sample placed between the fields alters the neutron velocity, the second field will no longer cancel out the effect of the first, thereby encoding the velocity change into the neutron spin angle, making it possible to register very small energy changes down to neV [30].

Neutron Spin-Echo can be used to measure a wide range of signals from spectroscopy, as described above, and quasielastic scattering to small angle scattering and re-

flectometry. In this thesis the focus will be on the Spin-Echo techniques used in elastic scattering. Defining a quantisation direction, z, the neutron spin can be described as either pointing up or down, and the measured quantity in an experiment is the polarisation, P_z, along z. The polarisation of a neutron beam, P_z, is defined as the average over all spin-vectors divided by their modulus, and can be calculated from measurements of the intensity with initial spin direction up ($I_\uparrow$) and initial spin direction down ($I_\downarrow$):

$$P = \frac{I_\uparrow - I_\downarrow}{I_\uparrow + I_\downarrow} \,. \tag{2.33}$$

2.7.1 Spin-Echo Small Angle Neutron Scattering

Spin-Echo Small Angle Neutron Scattering (SESANS) is a technique where magnetic fields with inclined surfaces with respect to the optical axis are used to encode scattering angle into neutron spin precession angle (see Fig. 2.4).

A spin-up polarised neutron beam passing through both identically shaped precession field regions with fields in opposite directions at a straight line will regain its original polarisation at the exit of the second field, which means that for un-scattered neutrons the Spin-Echo will be achieved. However, if a neutron is small angle scattered by

Figure 2.4 SESANS schematics. Two identically shaped precession field regions with fields in opposite directions and inclined field surfaces with respect to the optical axis. The scattering angle is encoded in the precession angle of the scattered neutron's spin.

the sample in between the fields, the neutron spin angle precession in the second field region will no longer cancel out the precession in the first field region, because of the altered trajectory. The resulting polarisation will in this case be different from the un-scattered neutron, and the scattering angle will be encoded in the polarisation [13, 36]. The precession angle, ϕ_1, of the spin gained by the neutron passing through the first precession region in Fig. 2.4 is given by eq. (2.32) assuming a non-divergent beam. The spin of the neutron scattered by θ_S from the sample will gain a precession angle of:

$$\phi_2 = c\lambda BL\frac{\sin\theta_0}{\sin\left(\theta_0+\theta_S\right)} \cong c\lambda BL(1+\theta_S\cot\theta_0) \qquad (2.34)$$

in the second precession region. The component of scattering vector perpendicular to the optical axis and the direction of the magnetic field ("up" in Fig. 2.4) is given by:

$$q_z = \frac{2\pi\theta_S}{\lambda}\,, \qquad (2.35)$$

and the Spin-Echo length, δ^{SE}, which is the length at which the density correlations in the sample are measured, is given by [20]:

$$\delta^{SE} = \frac{c\lambda^2 BL\cot\theta_0}{2\pi}\,. \qquad (2.36)$$

With the inclusion of divergence of the neutron beam the $\cot\theta_0$ factor has to be averaged over the divergence in the z-direction. The net precession angle, $\phi = \phi_1 - \phi_2$ (see Fig. 2.4), is not measured directly, instead the measured quantity is the polarisation along z normalised by the empty beam polarisation [37]:

$$P(\delta^{SE}) \equiv \frac{P_z(\delta^{SE})}{P_0} = \cos\phi = \cos(\delta^{SE} q_z) \; . \tag{2.37}$$

In order to model $P(\delta^{SE})$ data obtained through a SESANS experiment, we use the SESANS correlation function, $G(\delta^{SE})$, which is the projection along the optical axis of the density-density autocorrelation function of the sample (which in turn is proportional to the Fourier Transform of the intensity measured in conventional SANS) [1]. The relationship between P and G is given by:

$$P(\delta^{SE}) = \exp\left(\Sigma t \left[G(\delta^{SE}) - 1\right]\right) \; , \tag{2.38}$$

where, Σ and t are the macroscopic total scattering cross section per unit volume and the sample thickness respectively. Examples of data modelled using G can be found in Chapter 4, as the correlation functions used in SESANS and SEMSANS are indentical.

2.8 Neutron instrumentation

This section contains a brief description of the relevant neutron instrumentation components used in the experiments on which this thesis is based.

2.8.1 Choppers

In order to create and control the ToF of the neutrons choppers are used. Choppers are rotating neutron absorbing discs with transmitting cut-outs (see Fig. 2.5, *left*). By adjusting the rotation frequency and direction, the chopper position, the cut-out size and number, the chopper phase and possibly using multiple choppers, the time structure of the generated neutron pulse can be tailored to satisfy the required wavelength-band, time resolution, etc.

2.8.2 Spin polarisation and spin analysis

Our methods for inducing a spatial modulation through the use of Spin-Echo techniques is based on manipulating the neutron spin orientation. In order to do this the initial polarisation of the neutron beam must be known and controlled.

Neutrons coming from the source of a neutron scattering facility have their spins randomly oriented, so in order

to properly control the spin angle the neutrons need to be polarised so that (most of) the neutrons have their spins pointing in the same direction to begin with.

Several methods exist to polarise the neutrons. Some use polarised Helium-3 gas, which has a neutron spin dependent absorption, such that most neutrons with spin in one direction are absorbed while neutrons with the opposite spin are transmitted [7]. The method chosen for our experiments was to use supermirror polarisers. A supermirror reflects neutrons hitting the mirror at a relative wide range of wavelengths and incident angles by being composed of multiple atomic layers of different d-spacing (see eq. 2.24 and Fig. 2.5, *middle*). By magnetising the material of the mirror the scattering length density will be highly different for spin-up neutrons compared to spin-down neutron, thereby polarising the neutrons interacting with the mirror [11, 19]. When analysing the polarisation of the neutron beam a second supermirror polariser was used.

2.8.3 Spin rotators/flippers

Being able to control and manipulate the spin direction of the polarised neutrons is vital in Spin-Echo experiments. In our set-ups we needed to rotate the spins by $\pi/2$ from the vertical plane is which they were polarised to the horizontal plane in which they precess, and back again to the

vertical plane at the end of the precession regions before the neutron polarisation analysis. Furthermore, in some set-ups we needed to flip the neutron by π, in order to have magnetic fields regions on each side of the flipper to be in effectively opposite directions.

In our case we used pairs of adiabatic $\pi/2$-rotators, called Delft V-coils [17, 18, 33]. A V-coil consists on one side of wires evenly spread in a current screen, whereas on the other side the wires are packed together closely at the top and bottom of the coil, thereby creating the name-giving V-shape of the coil (see Fig. 2.5, *right*). The result is a magnetic field rising from zero at one end of the V-coil to maximum at the current screen end. Placing such a coil after the polariser with the current screen end facing downstream, the tail of the polariser field will slowly go to zero while the perpendicular V-coil field picks up, thereby rotating the neutrons by $\pi/2$. The sign of the V-coil field will choose wether spin up or spin down neutron are used. A second V-coil upstream with the current screen perpendicular to the first will start the precession of the neutrons. Using the V-coil pair as if neutrons were traveling in the reverse direction, will stop the precession of the neutrons and rotate them $\pi/2$ into the vertical plane of the neutron analyser. Two V-coils with the current screens facing each other and the fields anti-parallel will act as a π-flipper for the neutron spins.

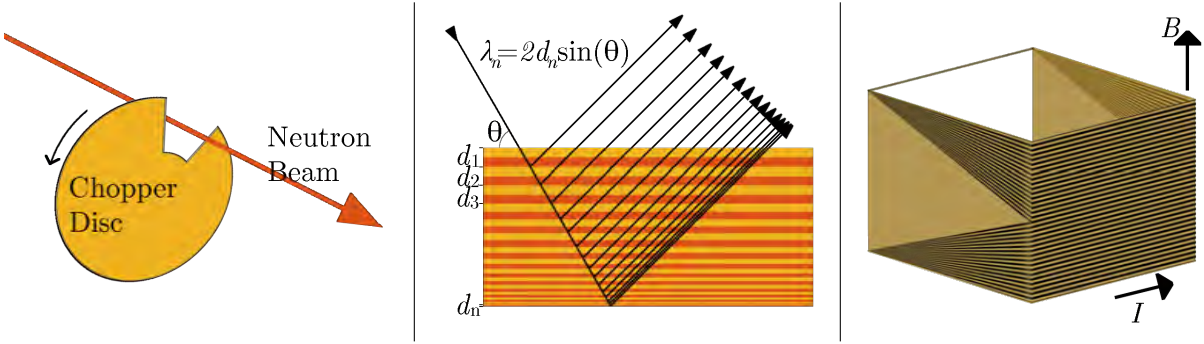

Figure 2.5 *Left*, a rotating chopper disc cuts a continuous neutron beam into pulses, such that the ToF can be recorded. *Middle*, a supermirror consists of layers of varying thickness such that Bragg's Law (eq. (2.24)) is fulfilled for multiple wavelengths and scattering angles. *Right*, a Delft V-coil $\pi/2$-rotator, used for manipulating the neutron spin direction.

2.8.4 Detectors

Many different kinds of neutron detection system are used in neutron scattering. For our fist experiment in Chapter 3 we only measured the ToF of the neutrons using a single pixel detector consisting of a ^{3}He+Ar gas filled tube across which a high voltage is applied. A neutron entering the tube can interact with a gas particle producing a charged particle that will ionise other atoms in the gas, resulting in a flow of current between the cathode and anode of the detector.

For the rest of the measurements presented in this thesis a detector capable of both spatial and temporal sensitivity was needed, and for this a currently one of a kind microchannel plate with detector high speed readout was used [51, 52]. Such a detector consists of tiny pores each one acting as an electron multiplier for a charged particle created by a neutron hitting a material with high neutron capture cross section (in our case ^{10}B) covering the microchannel. This provides the spatial resolution since each channel can be regarded as a single pixel detector.

2.9 Monte-Carlo ray-tracing simulations

To support our measurements in Chapter 3 a virtual version of the instrumental set-up was created using the Monte-Carlo neutron ray-tracing simulation software package McStas [22, 56]. With a neutron instrument consisting of multiple complicated components, analytical calculations of the resulting neutron wavelength band, divergence, position, ToF, polarisation, etc., becomes too complicated. In McStas neutron rays from a virtual source are propagated through virtual components, with each component altering the neutron properties according to the component definition. At the source, the neutrons are randomly generated with initial velocities, spin orientations and wavelengths within chosen limits. With enough neutron rays simulated, the output from the virtual detector will approximate the output from a real instrument, though limited by simplifications in the virtual components descriptions. Such virtual instruments can aid to investigate properties and go beyond the capabilities of real set-ups. The meta-language of McStas allows for a straightforward virtual instrument (and component) design (see appendix D.1), with components, such as choppers, spin-rotators, and detectors, described in the order by which the are reached by neu-

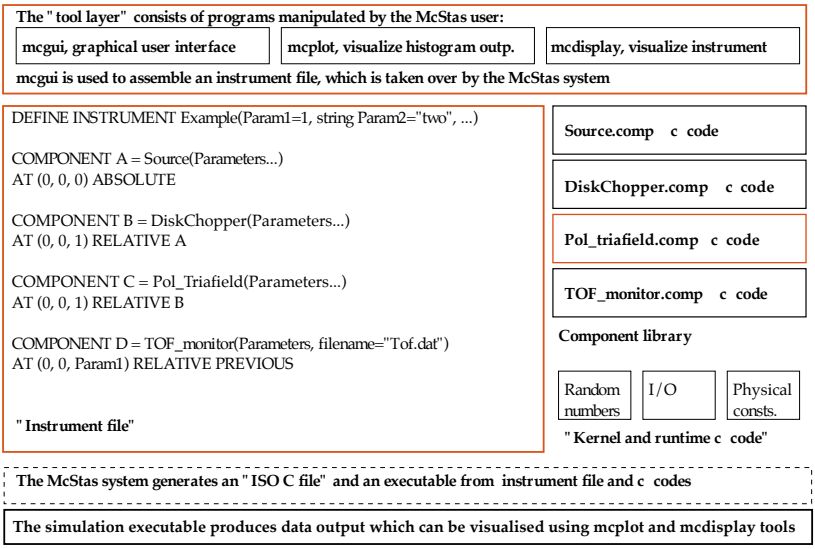

Figure 2.6 Structure of the McStas package. We have worked in the "tool", "instrument file", and "component" layers for this project (marked in red). Adapted from [55].

tron coming from the virtual neutron source. The McStas simulations performed in relation to this thesis include instrument design by using the available components from the McStas library with an additional component for triangular magnetic fields created specifically for this project (see appendix D.2). The deeper layers of the McStas package, that run the actual simulations based on the user input, have been used as they are provided by the McStas group (see Fig. 2.6).

Chapter 3

Investigating Time-of-Flight Spin Echo Modulation for Small Angle Neutron Scattering through Experiments and Simulation

Authors: Morten Sales[a,b], Jeroen Plomp[c], Klaus Habicht[a] and Markus Strobl[d]

Affiliations: [a]Helmholtz-Zentrum Berlin für Materialen und Energie GmbH, Germany, [b]Nano-Science Center, Niels Bohr Institute, University of Copenhagen, Denmark, [c]Faculty of Applied Sciences, Delft University of Technology, The Netherlands, and [d]European Spallation Source ESS-AB, Science Division, Sweden.

Journal: J. Appl. Cryst. (2015). **48**, 92–96

Link: http://dx.doi.org/10.1107/S1600576714025916

Introduction to Article

The work presented in the article below is based on experiments performed at the Reactor Institute Delft, The Netherlands. The bulk of the experimental work was performed by Jeroen Plomp and myself, though it was based on previously performed experiments [47]. I performed the data reduction and analysis, created the article figures, and wrote the article with inputs from the other authors. Furthermore I carried out all the Monte-Carlo Ray Tracing simulations including the writing of a new triangular magnetic field component.

The figure layout and the terminology used have been altered for consistency throughout this thesis.

3.1 Abstract

A Spin-Echo Modulated Small Angle Neutron Scattering (SEMSANS) instrument in a time-of-flight (TOF) mode will be able to excel at pulsed neutron sources such as the European Spallation Source (ESS) currently under construction.

In this work we compare experimental data from a TOF SEMSANS set-up, where a spatial beam modulation of a white beam is obtained using triangular field coils, with Monte Carlo ray tracing simulations.

Our experiments and simulations in accordance demonstrate that a good contrast can be achieved, using a constant field in the triangular coils. In our set-up only neutrons with certain wavelengths rotate by a Larmor precession angle that spatially modulates their polarisation to be coinciding with the period of a grating installed at the detector position. This is shown by measuring with a broad wavelength range while scanning the echo condition.

3.2 Introduction

Spin-Echo SANS (SESANS) is a technique [36, 4, 37, 34] that has proven to be well suited for investigating structures with large correlation lengths (up to the μm range). The de-coupling of beam collimation and structure size resolution allows a non-collimated neutron beam and hence higher intensities than in angular dispersive methods to be exploited. Magnetic field areas with inclined surfaces with respect to the neutron beam are used to map wave vector transfer into beam polarisation values, through manipulation of the neutron spin. The shortcoming of this technique is that, without complicated magnetic field arrangements, the signal is destroyed by e.g., ferromagnetic samples and sample environment with remanent magnetisation. To overcome this, a technique to use similar magnetic field areas to spatially modulate the beam and measure SANS was proposed by Gähler [8]. In this case spin manipulation and even polarisation analysis can be performed before the sample. The scattering information is obtained from analysing the amplitude damping induced by SANS in a spatially modulated beam which is hence decoupled from potentially de-polarising effects of the sample and sample environment. A SEMSANS instrument [2, 48, 47] is in principle able to measure structures in the same range

as SESANS, however, it includes uncomplicated measurements on magnetic samples.

Beam modulation of this kind has first been demonstrated [2] with a monochromatic set-up and subsequently the method could be tested successfully recovering SANS information in a monochromatic [48] as well as in a TOF SEMSANS measurement [47]. The latter set-up was used for the measurements in the present work as well.

3.3 Experimental set-up

Experiments were performed at the Reactor Institute Delft (RID) using main installations of the WESP beam line including a double-disk chopper system to create neutron pulses, super mirror multi-channel neutron polariser and analyser as well as V-coils (adiabatic $\pi/2$ rotators) [17], guide fields and finally a ^{3}He tube detector capable of the required time resolution (of 40 μs). Cadmium absorption gratings of varying periodicity were produced and used in front of the detector in order to resolve spatial beam modulation. The schematic layout of the experimental set-up is shown in detail in Figure 3.1.

The neutron beam is chopped into pulses by the two chopper discs, who each have two 180° separated openings and co-rotate at 25 Hz in an optically blind mode [54] pro-

viding a constant wavelength resolution of about 5% $\delta\lambda/\lambda$ at the detector with a chopper detector distance of about 6.22 m. Neutrons in the resulting pulsed beam are further downstream vertically polarised (in the y-direction). A first V-coil pair rotates the neutron spin into the horizontal xz-plane and starts the precession in the precession field, which together with the triangular fields is in the -y-direction. By the first V-coil pair the polarisation direction (+x or -x) can be chosen by changing the direction of the current in the first coil, which equals a 180° difference in initial spin orientation. Without current in the isosceles triangular coils [47], the neutrons would precess in one direction until they are π-flipped by the middle V-coil pair, whereafter they rotate 'back' to their original orientation at the end of the precession field yielding a Spin-Echo. The last V-coil pair acts as precession stopper (flip to vertical and flip back to horizontal orientation) before the neutrons reach the analyser, which analyses in the horizontal x-direction before the neutrons are detected.

3.3.1 Triangular fields

The triangular coils create a field parallel to the precession field and a neutron passing through such coil with a trajectory parallel to the optical axis will experience extra spin

precession dependent on the x-position given by [2]:

$$\phi = \frac{2c\lambda B_i x}{\tan\theta_0} \,, \tag{3.1}$$

where $c = 4.632 \times 10^{14}\ \mathrm{T^{-1}m^{-2}}$ (the Larmor constant), λ is the wavelength, B_i is the magnetic field in the triangular coil and θ_0 is the inclination angle between the leg and the base of the triangle. The base is aligned in the yz-plane and in the given set-up $\theta_0 = 20^\circ$. With L_1 (L_2) being the distance from the first (second) triangular coil to the detector (in our case the position of the absorption gratings) the fields of these coils (B_1 and B_2) have to be chosen fulfilling [3]:

$$B_1 L_1 = B_2 L_2 \,. \tag{3.2}$$

With this condition met for neutrons which travel through the triangular coils with finite divergence [2], the final precession angle is a function of the x-position in the detector (absorption grating) plane only. However, a π-flip is required in the V-coils between the triangular coils, in order to assure that B_1 and B_2 are effectively in opposite directions with respect to the precession plane. The period of the spatially sinusoidally modulated beam after the analyser

is then given by [47]:

$$\zeta = \frac{\pi \tan \theta_0}{c\lambda \left(B_2 - B_1\right)} \,. \tag{3.3}$$

The used triangular coils reached fields up to 4.44 mT which corresponds to achievable modulation periods of down to 3.34 mm at $\lambda = 4$ Å when L_1 and L_2 were 3.24 m and 1.89 m respectively. See Table 3.2 for corresponding magnetic field strengths, modulation periods and wavelengths used in the experiment.

The modulation periods were measured by placing a grating at the position given by eq. (3.2), and in such a case the actual position of a detector behind the grating is not relevant. In our measurements the detector was placed 20 cm further downstream. The Spin-Echo condition was scanned using a translation stage to move the middle V-coil pair responsible for the π-flip. That varies the balance of precessions experienced before and after the spin flip and only with the π-flipper in a certain position, is full echo achieved. Measuring intensity as a function of wavelength for a range of flipper positions will give maximum intensity modulation contrast when the beam modulation period matches that of the grating. The absorbing parts of the grating were approximately twice as wide as the transmitting parts which is close to the optimal choice in

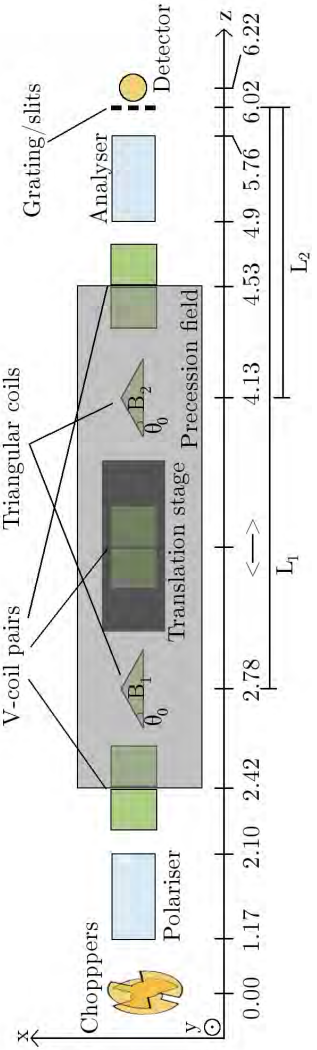

Figure 3.1 SEMSANS set-up viewed from above with neutron beam in z-direction. Not to scale.

Table 3.2 Corresponding wavelengths for different modulation periods and fields in the triangular coils. Note that the top row field values that were used in the experiment fulfil eq. (3.2) so that the signal "focuses" on the grating. The bottom row value for the B_1 field used in the experiment was 0.03 mT lower than the theoretical value set by eq. (3.2).

B_1 [mT]	B_2 [mT]	ζ (mm)	λ [Å]
1.75	3.00	4.50	4.39
		7.55	2.62
2.56	4.44	4.50	2.92
		7.55	1.74

the trade-off between transmitted intensity and contrast of the modulation signal, since wider grating openings (while keeping the grating period the same) will result in less modulation contrast and narrower grating openings will result in a stronger loss of intensity. This can be shown by calculating the Figure-Of-Merit: $FOM = I \cdot P^2$, where I is the transmitted intensity and the P is the contrast. The intensity increases linearly as a function of the transmitting fraction of the grating and is given by: $I = I_+ + I_-$, where the $+$ and $-$ denotes the up and down transmitted intensities respectively with: $I_\pm = \int_0^{\pi/f}(1 \pm \cos\phi)\mathrm{d}\phi$, where f is the transmitting fraction of the grating. The contrast is given by: $P = \frac{I_+ - I_-}{I_+ + I_-}$, so we get a maximum FOM at approximately $f = 0.37$, which is very close to the ratio used in our experiment.

Since the two triangular fields were of different strengths, it was necessary to compensate for this asymmetry in the field integral by moving the central V-coil pair with the translation stage and adjusting the strength of the field in the second V-coil of the first V-coil pair.

3.3.2 Simulations

The simulations were carried out using McStas 2.0 [56, 16]. A simple source with a flat energy spectrum was used. A special component describing the triangular field regions was written for the Monte Carlo simulations described here. Code for the component and the instrument can be found in Appendix D and on the McStas website [27]. The adjustments of the second V-coil [15] to obtain an echo were simulated by adding to the field strength of the precession field before the first triangular coil. Choppers and detector were simulated using the experimental values for opening angles, size, rotation frequency and time bin size, so that the virtual instrument was near-identical to the real one with respect to wavelength resolution. The simulated fields as well as polariser and analyser were all perfect with respect to field homogeneity and field boundaries. To approximate the non-perfect initial polarisation, depolarising effects caused by non-perfect fields and alignments in the experiment and coarseness of the grating, an initial

polarisation of 80% for all wavelengths was chosen in the simulations by comparing them with the experimental results. It was done by combining simulations with opposite initial polarisation in the right ratio.

3.4 Results

Figure 3.3 shows an overview of our main experimental results for different combinations of three triangular field strengths and three grating/slit periods at the detector position. The x-axis is the position of the flipper coil (scanned with movement of the translation stage), the y-axis is the wavelength of the neutrons (recovered from the TOF at the detector) and the colour scale corresponds to the attenuation corrected signal, calculated using $M_C = \frac{I_\uparrow - I_\downarrow}{I_\uparrow + I_\downarrow}$, where $I_\uparrow$ ($I_\downarrow$) is the intensity measured in the detector when the neutrons exit the first V-coil polarised in the x (-x) direction. It can be seen in Figure 3.3 that with no current in the triangular coils and/or a single slit in front of the detector, the attenuation corrected signal is equally strong for all wavelengths since this corresponds to a normal TOF Spin-Echo measurement [30, p. 25]. When a beam modulation and a grating (or double slit) is introduced in front of the detector at the "focal point" defined by eq. (3.2), only certain wavelengths will still lead to a signal in the detector and will

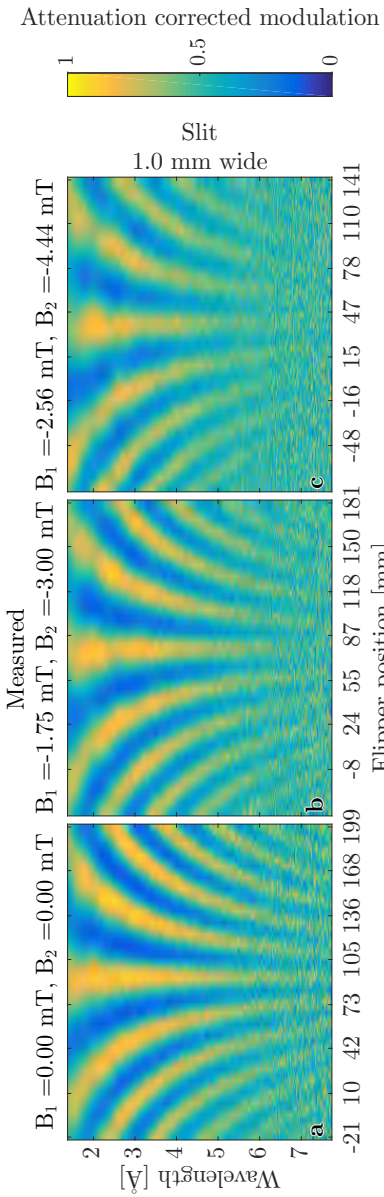

Figure 3.3 Part 1/2. Experimental results. Columns are different fields (different modulation periods). 1.0 mm wide single slit.

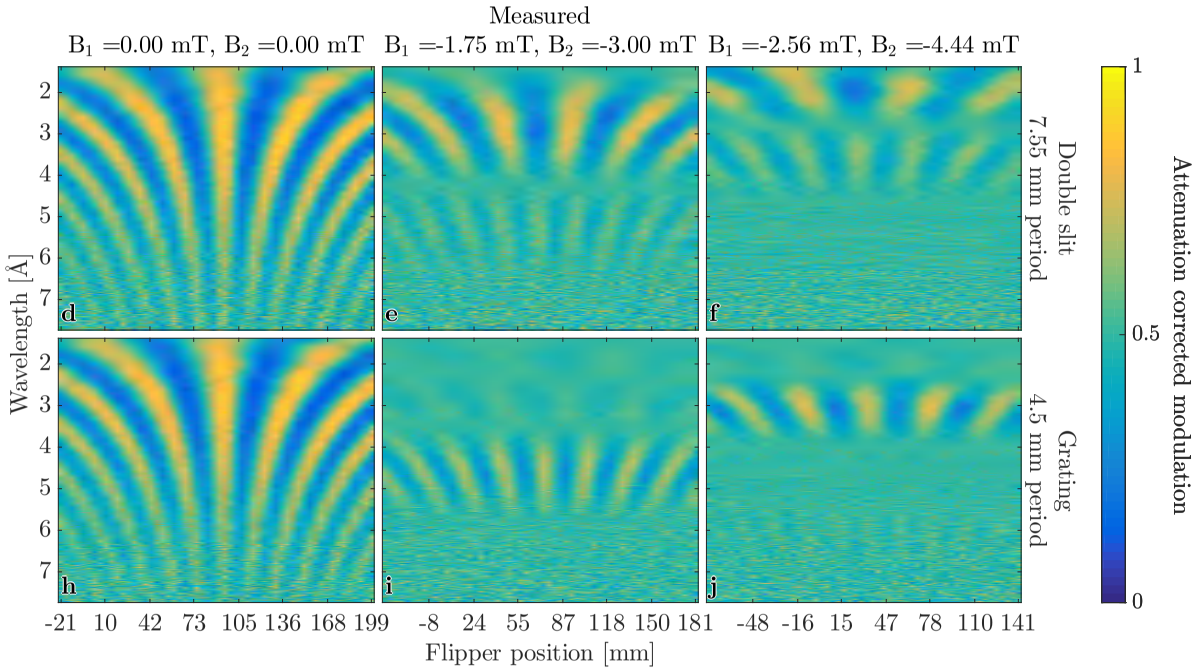

Figure 3.3 Part 2/2. Experimental results. Columns are different fields (different modulation periods) and rows are different gratings or slits (grating with 4.5 mm period or double slit with 7.55 mm period).

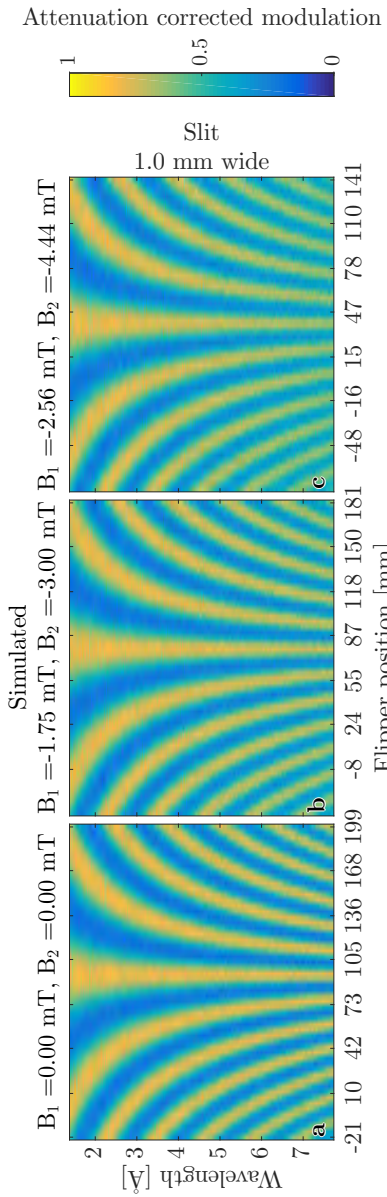

Figure 3.4 Part 1/2. Simulation results. Columns are different fields (different modulation periods).1.0 mm wide single slit. Experimental depolarising effects are approximated by having an initial polarisation of 80% for all wavelengths in simulations.

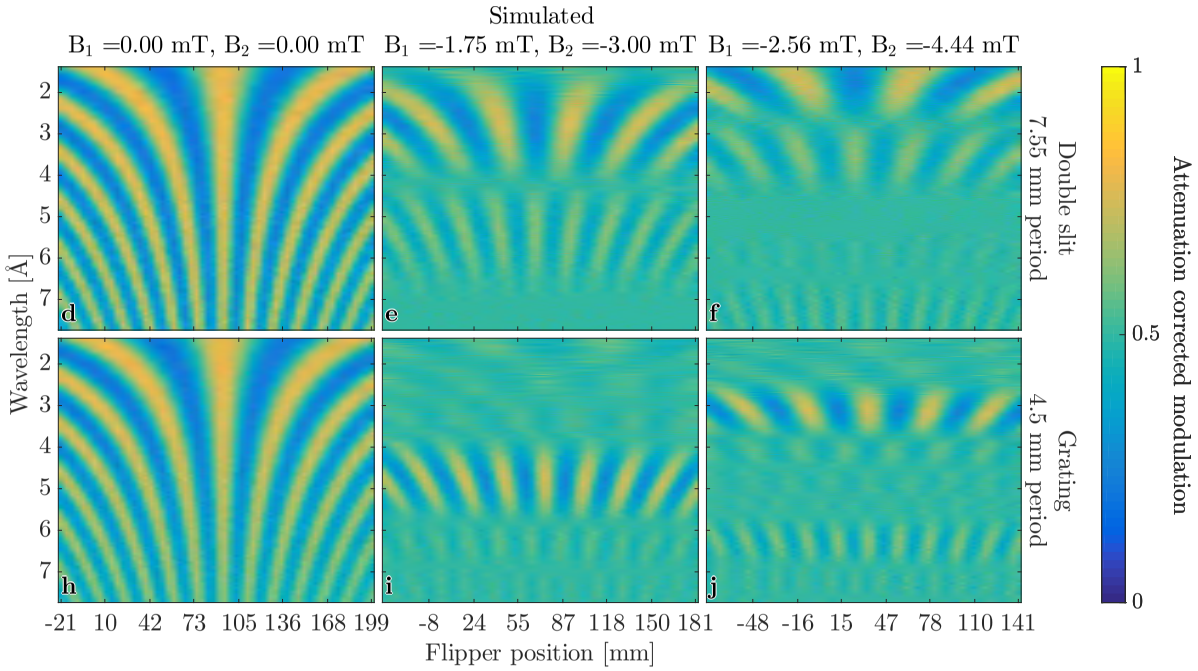

Figure 3.4 Part 2/2. Simulation results. Columns are different fields (different modulation periods) and rows are different gratings or slits (grating with 4.5 mm period or double slit with 7.55 mm period).

produce a modulation as the modulation pattern is shifted over the corresponding grating by scanning the echo. This is displayed in Figure 3.3 (e), (f), (i) and (j), where also a second order signal can be found, since neutrons with twice the wavelength are spatially modulated with half the modulation period (eq. (3.3)), which is indeed also a match in creating modulation in the detector response. This signal is seen since the transmitting parts of the gratings where narrower than the absorbing parts.

As shown in Figure 3.4 the simulation results replicate the measurements. Comparisons for selected wavelengths are shown in Figure 3.5, and underline a very good agreement between measurements and simulations. The selected wavelengths were chosen based on Table 3.2 or the mean simulated wavelength, 4.56 Å. In Figure 3.3 a), b), c), d) and h) it can be seen that there is little difference between these five results since they were at zero field in the triangular coils and/or with only a single slit in front of the detector therefore only displaying a normal TOF Spin-Echo signal. The slight signal difference still present is a result of differences in the strength of the precession field, π-flip location and – in the experiment – the adjustments of the second V-coil.

In Figure 2-3 of Strobl et al. [47] experimental images and integrated line profiles of a spatially modulated neutron beam are shown both for empty beam and measure-

ments on a sample. All these figures exhibit an asymmetry of the beam profile where the modulation amplitude is dropping from one side of the beam to the other. Figure 3.6 shows simulated outputs of an x-position and TOF sensitive detector in and out of echo. It is evident that when the Spin-Echo condition is met the resulting signal is symmetric and of higher contrast, and the simulation results suggest that the Spin-Echo not being met is the reason for the asymmetry found in Fig. 2-3 of Strobl et al. [47], which we are hence able to understand and explain based on the presented results. The only difference between the two simulations in Figure 3.6 is the position of the flipper (middle V-coil pair).

3.5 Conclusion

Good agreement between simulation and experiment proves that the simulation model describes the instrument well and both measurements and simulation are in good agreement with theory. Monte Carlo ray-tracing simulation counterparts to real instruments helps to decouple the instrument signal and the imperfections of it from the one created by an investigated sample.

The combination of real and virtual investigations of a SEMSANS instrument has allowed us to gain insightful

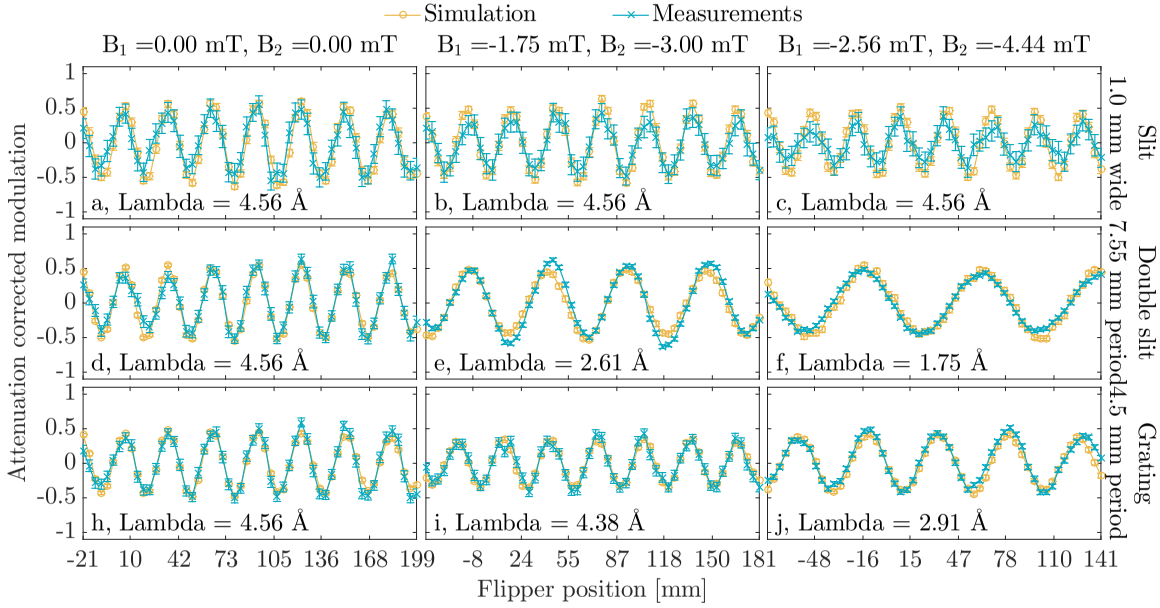

Figure 3.5 Comparison between experimental and simulation results for selected wavelengths. Wavelengths for e), f), i), and j) were chosen as they correspond to neutrons being spatially modulated with periods that matches that of the grating/double slit (see eq. (3.3) and Table 3.2). 4.56 Å is the mean of the wavelength range measured/simulated and was chosen for a), b), c), d) and h).

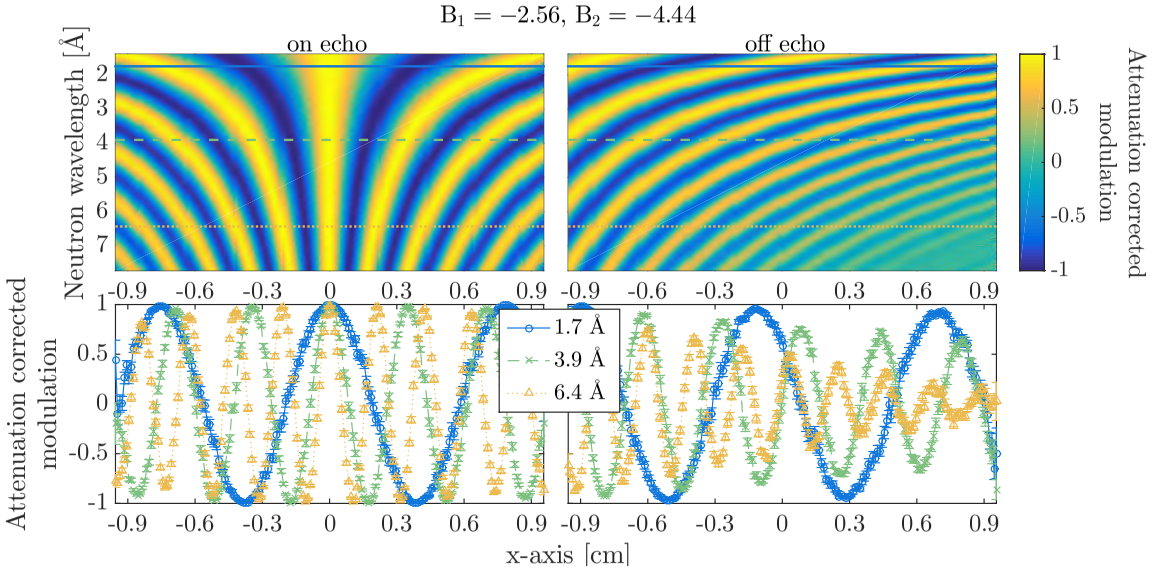

Figure 3.6 Simulation with a x-position sensitive TOF monitor at the "focus" position. Left is when the Spin-Echo condition is met and right is off echo. Top is wavelength vs x-position at the detector with the colour scale corresponding to the polarisation. Bottom is polarisation vs x-position for selected wavelengths. It can be seen that an asymmetry and loss of contrast is introduced when the Spin-Echo condition is not met (e.g., by adjusting the position of the spin-flipper composed of the middle V-coil pair).

knowledge on the modulation patterns' dependency on the field settings. Specifically, the importance of tuning the set-up to keep the signal in the Spin-Echo condition was found as an important factor in avoiding asymmetries or other drawbacks for the instrumental function such as losses of signal, i.e., as function of TOF modulation amplitudes of the magnetic fields in the triangular coils in this case. It has also been shown how SEMSANS experiments can be performed by combining absorption gratings with a detector without spatial resolution even in TOF mode, though the efficiency is reduced by the limited useful wavelength ranges in such case.

For future TOF SEMSANS experiments, which will be a powerful tool at high brilliance pulsed spallation sources, the found importance of keeping the echo condition has significant implications especially for cases when absorption gratings have to be used, because of the spatial detector resolution being insufficient to resolve the modulation spatially. In order to keep the modulation period constant for such a measurement to be efficient, it is now obvious that not only the triangular fields will have to be ramped corresponding to the pulse, but also a corresponding additional phase has to be added by an additional ramped field region.

Such set-ups are considered for use not only as a SANS instrument but also for spatially resolved SANS investi-

gations in a quantitative dark-field imaging [48, 47, 46] mode e.g., at the European Spallation Source [44]. Also such approaches can be modelled and simulated based on the presented work.

Chapter 4

Quantitative Neutron Dark-field Imaging through Spin-Echo Interferometry

Authors: Markus Strobl[a,b], Morten Sales[b,c], Jeroen Plomp[d], Wim G. Bouwman[d], Anton S. Tremsin[e], Anders Kaestner[f], Catherine Pappas[d] and Klaus Habicht[c].

Affiliations: [a]European Spallation Source AB, Sweden, [b]University of Copenhagen, The Niels Bohr Institute, Denmark, [c]Helmholtz Centre Berlin for Materials and Energy (HZB), Germany, [d]Delft University of Technology, Reactor Institut Delft, The Netherlands, [e]University of California at Berkeley, Space Sciences Laboratory, USA, [f]Paul Scherrer Institut, Switzerland.

Journal: Sci. Rep. (2015). **5**, 16576

DOI: 10.1038/srep16576

Link: http://dx.doi.org/10.1038/srep16576

Introduction to Article

The work presented in the article below is based on experiments performed at the Reactor Institute Delft, The Netherlands. The experimental work was performed by Jeroen Plomp, Wim G. Bouwman, Anton S. Tremsin, Klaus Habicht and myself and was based on previous work described in Chapter 3. I performed the data reduction and analysis, with image filters from Anders

Kaestner, and created the article figures. Markus Strobl drafted the article with inputs from myself and the other authors. The figure layout has been altered for consistency throughout this thesis.

4.1 Abstract

Neutron dark-field imaging constitutes a seminal progress in the field of neutron imaging as it combines real space resolution capability with information provided by one of the most significant neutron scattering technique, namely small angle scattering. The success of structural characterisations bridging the gap between macroscopic and microscopic features has been enabled by the introduction of grating interferometers so far. The induced interference pattern, a spatial beam modulation, allows for mapping of small-angle scattering signals and hence addressing microstructures beyond direct spatial resolution of the imaging system with high efficiency. However, to date the quantification in the small angle scattering regime is severely limited by the monochromatic approach. To overcome such drawback we here introduce an alternative and more flexible method of interferometric beam modulation utilising a spin-echo technique. This novel method facilitates

straightforward quantitative dark-field neutron imaging, i.e. the required quantitative microstructural characterisation combined with real space image resolution. For the first time quantitative microstructural reciprocal space information from small angle neutron scattering becomes available together with macroscopic image information creating the potential to quantify several orders of magnitude in structure sizes simultaneously.

4.2 Introduction

The promise of neutron dark-field imaging [46] is to provide access to structural features from the macroscopic range probed with image resolution to the microscopic range in the micrometer and sub-micrometer range and hence beyond direct spatial resolution of the order of 10 micrometers [57]. This can be provided through the registration of scatter signals in the (ultra)-small angle neutron scattering ((U-)SANS) regime which allows to close the gap between real space and reciprocal space methods. The corresponding size range is of significant importance to hierarchical structures and when probing real systems, be it in soft matter, biology or engineering and non-destructive testing of devices. Accordingly neutron dark-field imaging with grating interferometers [46], the first corresponding

method offering an efficiency suitable for the relatively low phase space density of neutron sources, has experienced a remarkable impact, especially in engineering [10] and magnetic structure characterisations [26, 9], strongholds of neutron applications. The fact that such wealth of results could be obtained up to now with only qualitative information in the scattering regime underlines the outstanding potential as well as the explicit need for quantitative solutions [43]. Therefore we are introducing a novel interferometer method for imaging based on neutron spin-echo principles, that is analogue to the grating interferometry approach, but, due to its higher flexibility, can provide full quantitative SANS characterisation in the dark-field regime and is well suited for time-of-flight (ToF) measurements. ToF is a neutron technique, which requires a pulsed beam and allows for intrinsic neutron energy resolution and hence for coverage of a significant scattering range simultaneously. Therefore our method will be able to take advantage of the most powerful new generation of pulsed neutron sources. However, the present proof-of-principle has been undertaken at the low-flux thermal neutron source of the Reactor Institute of Delft Technical University (RID/TUD) and could be quantified successfully despite of the low available brightness, which in turn is proving the efficiency of the method. The principle of interferometric dark-field imaging with a spatially modulated beam is that scatter-

ing to small angles will spatially redistribute intensities between the maxima and minima and hence dampens the amplitude of the beam modulation. Attenuation and differential phase signals can be recorded simultaneously but are well separated from the dark-field effect as these generally decrease the mean intensity or shift the modulation phase, respectively. Hence a systematic study of the effects on the spatial modulation allows for extracting attenuation, differential phase and the dark-field signal as a measure of small angle scattering separately. While Talbot Lau grating interferometers induce a cosine spatial beam modulation through phase and absorption gratings [32], in Spin-Echo-Modulation SANS (SEMSANS) such modulation is introduced by interference conditions induced by spin precession devices for a polarised neutron beam [3, 47]. It has been demonstrated earlier that such an approach can provide quantitative SANS characterisations in analogy to the well-established Spin-Echo SANS (SESANS) technique [35] even in a highly efficient ToF mode [47, 39], and that in analogy to grating interferometry also a grating analyser can be utilised when required in order to resolve the beam modulation [48]. It has in turn been demonstrated that in principle corresponding quantification is equally possible with grating interferometric dark-field imaging [43]. However gratings must be optimised for a single wavelength [32], a condition, which seems to severely limit straight-

forward broad application. For the work presented here a ToF SEMSANS instrument was modified in order to enable simultaneous real space image resolution. In contrast to earlier set-ups the sample position has been moved to behind the spin analyser and hence closer to the detector. Together with the beam collimation defined by a narrow entrance slit into the spin manipulation devices and a ToF imaging detector [52] this set-up allowed to achieve the additionally required spatial resolution. However, the new sample position also enables investigations of magnetic samples, which might depolarise the beam, as beam polarisation is not relevant anymore at that location of the sample.

The basic set-up depicted schematically in Figure 4.1 consists of a polariser and polarisation analyser, between which the spin polarised neutrons pass through two key precession fields which are directed in opposite directions. These precession field regions have a triangular shape, which guarantees, that (i) neutrons arriving at the same point in the detector have experienced the same total spin rotation and that (ii) this final rotation angle is to a first approximation a linear and continuous function of the lateral position across the beam on the detector. Hence the polarisation analyser located downstream of the second precession field induces a one-dimensional cosine modulation of the beam on the detector. To achieve such regular

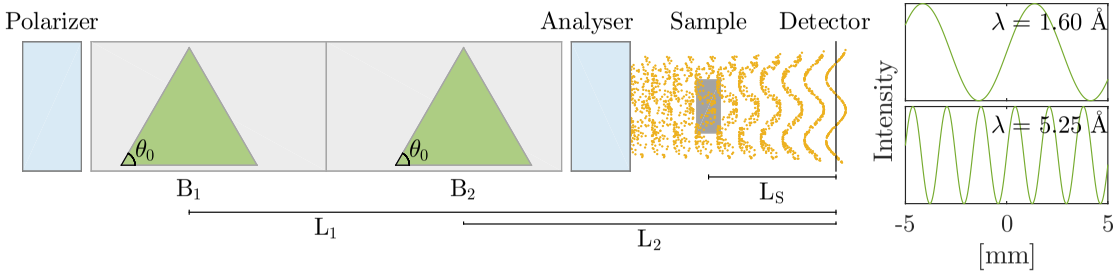

Figure 4.1 Schematic illustration of experimental set-up for SEMSANS-imaging including the polariser and analyser as well as triangularly shaped magnetic field regions and the induced spatial beam modulation in the area of the sample and detector. On the right hand side an example of beam modulations is given for two particular wavelengths.

modulation the focusing condition $L_1 B_1 = L_2 B_2$, where L_1 and L_2 and B_1 and B_2 are the distances to the detector and the field values of the two precession devices, respectively, has to be satisfied. The period, ζ, of the modulation can then be shown to be [3, 47]

$$\zeta = \frac{\pi \tan \theta_0}{c\lambda(B_2 - B_1)} , \tag{4.1}$$

with θ_0 the inclination of the precession field surfaces to the beam, λ the wavelength and $c = \gamma_n m_n / h = 4.632 \cdot 10^{14}\ \mathrm{T^{-1}m^{-2}}$ with γ_n and m_n the gyromagnetic ratio and the mass of the neutron and h the Planck constant. Together with the sample to detector distance L_S a spin-echo length δ^{SE} in analogy to SESANS [35] can be defined to be

$$\delta^{SE} = \frac{c\lambda^2 L_S (B_2 - B_1)}{\pi \tan \theta_0} = \frac{\lambda L_S}{\zeta} , \tag{4.2}$$

and denotes the correlation length probed with the corresponding settings. This establishes not only a complete analogy with SESANS on the one hand but also to grating interferometry with respect to the corresponding autocorrelation length that can be defined accordingly [43]. Both parameters, the period and the spin echo length are wavelength dependent with a linear and square dependence, respectively. Consequently, in a ToF configuration, intrinsi-

cally varying the wavelength over a certain range, allows to probe corresponding ranges of correlation lengths, i.e. structure sizes in the sample in the SANS regime. On the other hand also the magnetic fields and distances can be used to tune correlation lengths correspondingly and to tailor the range to the experimental requirements. This way the method provides an extensive flexibility which is required to probe a large range of length scales and which is lacking in the case of grating interferometers.

4.3 Measurements

For this work a ToF approach was chosen utilising optical blind pulse shaping choppers providing a wavelength resolution for the given instrument length of about $\delta\lambda/\lambda = 5\%$ [47]. The thermal source spectrum provided sufficient neutron flux for data recorded for wavelengths from 1.6 Å to 5.25 Å, and hence spin-echo lengths δ^{SE}, i.e. a structure size range, from about 15 nm to 180 nm could be probed. This corresponds to distances and magnetic fields set to $L_1 = 5$ m, $L_2 = 1.7$ m, $L_S = 0.55$ m and $B_1 = 1.43$ mT, $B_2 = 4.22$ mT. In contrast to conventional grating interferometry operating in the micrometer range, the corresponding modulation periods from 5.7 mm to 1.6 mm could be resolved directly by the spatial resolution of the detector

[52]. However, for smaller modulation periods and longer spin-echo lengths achieved e.g. with higher magnetic fields or longer wavelengths, also grating analysers like in the Talbot Lau interferometer case can be used. This has been demonstrated earlier for SEMSANS measurements [48]. For the presented case data analysis and image formation require intense post processing, as the real space image is superposed by the modulation. On the other hand no scanning approach like in the case of the utilisation of grating analysers is required. It can be shown that the relative modulation visibility with respect to the empty beam measurement V_S/V_0, with the visibility being V=(Imax-Imin)/(Imax+Imin), can be written, again in analogy to the grating interferometer case [43] and SESANS [3, 35] as

$$\frac{V_S(\delta^{SE})}{V_0(\delta^{SE})} = \exp\left(\Sigma t\left[G(\delta^{SE}) - 1\right]\right) \ . \tag{4.3}$$

Here, Σ and t represent the scattering power (total scattering cross section) and the sample thickness, respectively, while G is the real space correlation function of the scattering structures or particles [43, 47]. Hence, the normalised visibility V_S/V_0 is depending on the spin-echo length and thus is a direct measure of the scattering power Σ and real space correlation function G representing the scattering structures. Therefore analysing the visibility locally in the

recorded images allows full structural characterisation in the SANS range probed in real space for any lateral location in the sample.

For the measurements we used a sample consisting of two quartz cuvettes on top of each other (Figure 4.2). The top cuvette contained a magnetic metal powder (Ferroxdure YXF1, $BaFe_{12}O_{19}$, Yuxiang Magnetic Materials Ind. CO Ltd) with a probed thickness of 2 mm and an average grain size of the order of micrometers according to the producer. The lower cuvette was lying on its side and contained a solution of spherical polystyrene (PS-DVB) particles with defined monodispersive diameters of 136 nm in D_2O with a weight concentration of 12.4% and a sample thickness of 5 mm. Note that the metal pieces (Cd) visible in the photograph in Figure 4.2a have been removed after alignment of the sample which they aided. Additionally, the liquid sample displayed a significant meniscus between the walls of the cuvette, with a correspondingly reduced effective sample thickness in these areas, which is clearly represented in the attenuation contrast image (Figure 4.2b), but also in the dark-field SEMSANS image (Figure 4.2c). Measurements were performed for spin-up , $I_{\uparrow}$, and spin-down, $I_{\downarrow}$, neutrons, i.e. two opposite incoming spin polarisations, which corresponds to a modulation phase shift of π between the two measurements. Hence, using the sum of the two measurements the attenuation

Figure 4.2 Sample images. **(a)** Sample set-up photo with the exposed area highlighted **(b)** Attenuation contrast image of exposed region **(c)** Dark-field SEMSANS image displaying the visibility of the spin-echo modulation at a certain spin-echo length. Three areas of interest are highlighted in **(b)** and **(c)**: powder sample **(i)**, empty beam area **(j)** and Polystyrene dispersion **(k)**.

contrast image $I_a = I_\uparrow + I_\downarrow$ can be extracted straightforwardly (Figure 4.2b). Despite the overlaying beam modulation with wavelength dependent periods, and integrating over all time bins, i.e. the full utilised neutron spectrum, an image that can be referred to as a "white beam" radiography is provided. In addition the two opposite images in terms of the modulation can be used to calculate an attenuation corrected modulation signal (Figure 4.3 part 1). Open beam visibilities V_0, mainly limited by the polarisation quality, but also by experimental conditions like e.g. the detector resolution, have been found to be between 65% at 1.6 Å and 20% at 5.25 Å in the measurements. Measurement times for each of the two empty beam and sample measurements were of the order of 3.5 hours and can be performed much faster e.g. at state-of-the-art spallation neutron sources with several orders of magnitude higher pulsed brightness.

4.4 Results

The resulting image data sets were analysed in terms of the local modulation, in particular their local visibility. For this purpose a cosine fitting routine has been developed, which is capable of shifting the area of interest, typically the width of one period for the shortest utilised wavelength

(i.e. longest spatial period for a specific measurement) pixel by pixel over the full image. This way the modulation parameters can be extracted pixel by pixel as a running average over the given width, which in turn limits the spatial resolution achievable with such approach. However, due to the image blur introduced by the geometry of the setup, especially by the relatively long sample to detector distance with respect to a conventional imaging experiment, the spatial resolution was in any case limited to about 1 mm. In contrast to that the high pixel resolution of the detector of 55 micrometer was required to resolve the beam modulation. The results of corresponding fitting routines are displayed in the first part of Figure 4.3, while the second part displays the extracted relative visibility as a function of the spin-echo length probed by the ToF approach for several individual but representative image locations. To achieve quantitative results the latter have to be corrected by the sample thickness and wavelength dependence of the total scattering, which leads to the results in Figure 4.3 part 3 for three areas of interest in the sample, namely the powder sample (left), a sample-free area (middle) and the PVC dispersion (right). These final curves show good agreement with the complimentary SESANS measurements and theory curves describing the structural features of 1 μm and 136 nm for the metallic powder and the PS dispersion, respectively. The theoreti-

cal curves were derived with respect to the best fit using models for highly concentrated spheres (eq. 61 in [1]), taking into account next neighbour correlations in the case of the dilution of 12.4% PS in D_2O (eq. (23) in [14]) and for simple random two-phase media (eq. (53) in [1]) as well as random two-phase media with Hurst exponent based on eq. (56) in [1] for the powder sample. These are conventional models used to interpret small-angle scattering data, but adapted to Spin-Echo SANS. Applying these models to the data (Figure 4.3 part 2,3) suggest structure sizes of around 1 μm, as implied by the manufacturer, for the powder and between 110 nm and 160 nm for the PS particles with nominal diameters of 136 nm. The total scattering values deduced are in good agreement with the 12.4 wt.% concentration of the particles.

4.5 Conclusion

From these seminal results which unambiguously prove the principle and potential of the method, we conclude that the presented method not only unlocks the access to an intermediate size range for structural investigations, but also bridges an unprecedented size range between the macroscopic and microscopic scales, which is invaluable for the investigation of real systems and components as

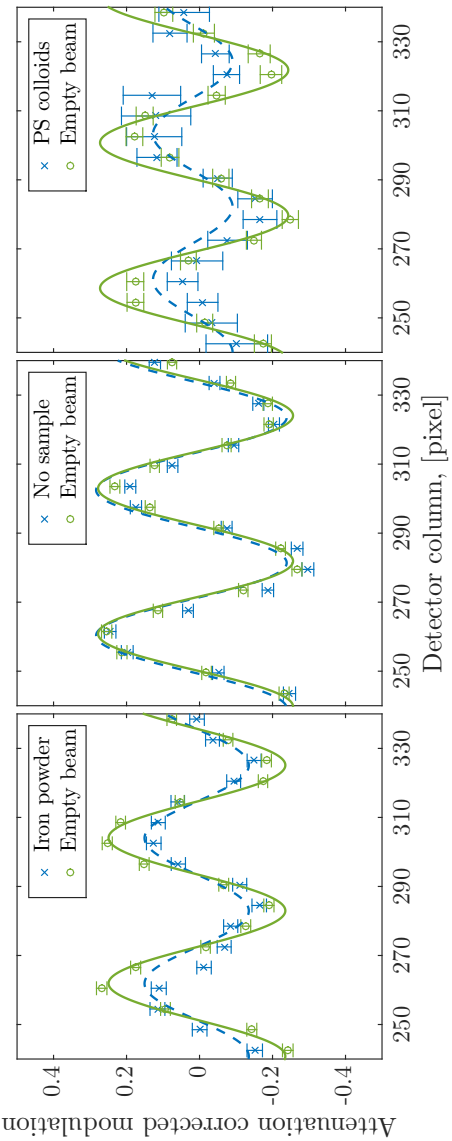

Figure 4.3 Data and results. Part 1/3: Examples of local fits of normalised data at $\delta^{SE} = 890$ Å. The plots from left to right correspond to the powder sample, open beam area and PVC dilution and hence to (parts) of the areas marked in Figure 4.2 as **a**, **b** and **c** respectively.

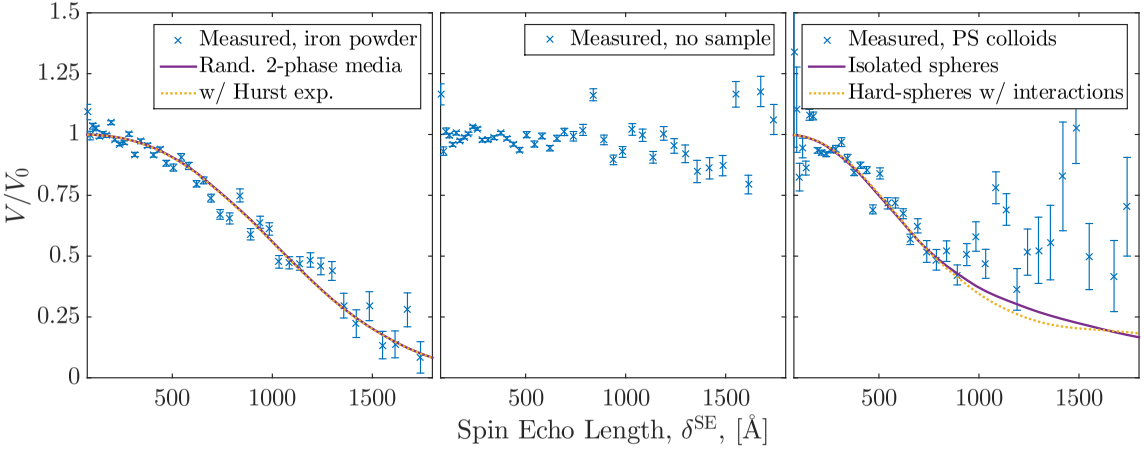

Figure 4.3 Data and results. Part 2/3: Extracted local visibility behaviour and corresponding model fits.

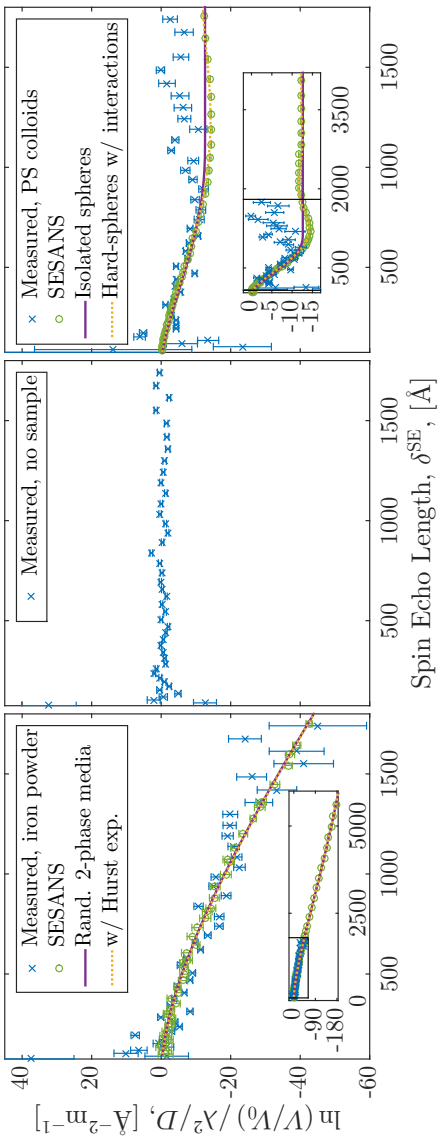

Figure 4.3 Data and results. Part 3/3: Corrected local SEMSANS curves compared to SESANS measurements which provide the correct sample parameters in terms of scattering cross section Σ and real space correlation function.

in contrast to homogeneous model samples of materials required for corresponding microscopic investigations otherwise. These proof-of-principle measurements with low flux at a thermal source and the limited capacity of the prototype magnetic set-up allow to extrapolate to an optimised set-up in the sense that at a powerful state-of-the-art pulsed source of cold neutrons the gap between real space and Fourier space investigations through scattering can be closed with a single set-up and even tomographic 3D structural investigations in this range might prove feasible. A correspondingly available flux increase of about 3 to 4 orders of magnitude in particular for longer wavelengths and magnetic fields tunable to values of about one order of magnitude higher, together will allow not only for improved statistics, shorter exposure times and for extending the covered size range of the SE analyses from the nanometer into the micrometer range, but also for extending the real space resolution from the millimetre to the micrometre range, like it is state of the art at dedicated instruments. This will pave the way for unprecedented observations of microstructural evolutions and inhomogeneities. The ToF approach, covering orders of magnitude in size simultaneously also enables kinetic studies of structural developments as neutrons enable a wide range of sample environments, applying pressures, temperatures, fields, strains, and shear like required in many fields of en-

gineering, soft matter and magnetism investigations. The evolution of magnetic domains, crystallographic grains, pores and voids as well as precipitates or coagulation and clustering on the corresponding microscopic length scales can be studied with simultaneous macroscopic resolution of process inhomogeneities. Kinetics and structure evolutions can be separated into local ones versus global in a sample, depending on external parameters and inherent structural features, and hence also studies of complex assemblies like biological or engineering systems and components become feasible in this range.

Chapter 5

A Pixel Based Approach for Spatially Resolved Analysis of Time-of-Flight Spin-Echo Modulated Scattering Data

Authors: Morten Sales[a], Jeroen Plomp[b], Wim G. Bouwman[b], Anton S. Tremsin[c], Klaus Habicht[d] and Markus Strobl[a,e].

Affiliations: [a]University of Copenhagen, The Niels Bohr Institute, Denmark, [b]Delft University of Technology, Reactor Institut Delft, The Netherlands, [c]University of California at Berkeley, Space Sciences Laboratory, USA,[d]Helmholtz Centre Berlin for Materials and Energy (HZB), Germany, [e]European Spallation Source AB, Sweden.

Journal: J. Appl. Cryst. (Submitted).

Introduction to Article

The work presented in the article below is based on experiments performed at the Reactor Institute Delft, The Netherlands. The experimental work was performed by Jeroen Plomp, Wim G. Bouwman, Anton S. Tremsin, Klaus Habicht and myself. I was responsible for performing the data reduction and analysis and creating the article figures. I drafted the article with inputs mainly from Markus Strobl and Jeroen Plomp. The figure layout has been altered for consistency throughout this thesis.

5.1 Abstract

Spin-Echo Modulated Small Angle Neutron Scattering with spatial resolution, i.e. quantitative Spin-Echo Dark Field Imaging, is an emerging technique combining neutron imaging with spatially resolved quantitative small angle scattering information. Earlier reported results were based on curve fitting of the sinusoidal spatially modulated intensities in order to obtain the scattering signal in the the modulation amplitude of the spatially modulated beam. This work compares such sine-fitting approach with a local analysis of the relative visibility of the modulation, by scaling the signal with the open beam measurements.

This allows in contrast to the fitting method a pixel-wise and hence highly spatially resolved analysis, which is key for imaging applications. However, this method comes with potential drawbacks which will be outlined and discussed in detail.

5.2 Introduction

While Spin-Echo Small Angle Neutron Scattering (SESANS) [36] is an established neutron small angle scattering technique extending the range of Small Angle Scattering (SANS) to very small (VSANS) and ultra small (USANS) angles,

Spin-Echo Modulated Small Angle Neutron Scattering (SEMSANS) has been introduced only recently [8, 2, 3, 48, 47]. SEMSANS can be seen as a variation of SESANS, using less precession regions and providing the option to place the sample behind the spin-manipulation region, hence in a field free region where also magnetic samples can be measured. In contrast to SESANS, not the final beam polarisation, but a spatial beam modulation is measured, the damping of which provides the same information content as a SESANS polarisation measurement [43]. While for SEMSANS a spatially resolved detection is required, it offers on the other hand the potential for spatially resolved SANS studies in an imaging configuration, because the sample can be placed close to the detector and in both techniques a reasonable beam divergence can be used, allowing for a useful field of view for imaging. In fact, with the spatially modulated intensity on the detector, SEMSANS resembles the highly successful method to measure dark-field images and differential phase contrast with grating interferometers in neutron imaging instruments [32, 46]. It has been shown recently that both methods are equivalent to SESANS in their capability to measure quantitative small angle scattering [43]. However, the higher flexibility of the magnetic set-up of SEMSANS in contrast to a grating set-up, which is optimised for a single wavelength, makes it much more efficient for quantitative SANS studies with spatial reso-

lution and in particular in a Time-of-Flight (ToF) mode, taking advantage of modern pulsed spallation sources. A particular drawback for Spin-Echo Modulated Dark-Field imaging (SEM-DF) [49], especially in the very small angle region, in which it has been demonstrated, is a limitation in spatial resolution imposed by the analysis of the spatial modulation with periods up to the mm range. Here we shall introduce an alternative approach of analysing corresponding ToF data, which decouples the spatial resolution from the modulation period. A pixel-by-pixel ToF analysis will utilise the full spatial resolution of the set-up and detector, only limited by scattering functions of different regions of interest that overlap.

5.3 Analysis of SEMSANS data

SEMSANS uses inclined field surfaces to map neutron small angle scattering information into the amplitude dampening of a spatially modulated beam [8, 2, 3, 48, 47]. Horizontally polarised neutrons moving (close to) parallel to the optical axis and passing through a triangular magnetic field region, with the field direction vertical, will gain a spin angle due to Larmor precession dependent on the position of intersection between the neutron path and the triangular coil. Two triangular coils with fields in opposite

directions, B_1 and B_2, are placed at distances L_1 and L_2 from the detector. With a spin analyser downstream from the coils, the result will be a spatially modulated intensity in the horizontal direction at the detector position, which even with a divergent neutron beam, will have a period of modulation given by [3]:

$$\zeta = \frac{\pi \tan\theta_0}{c\lambda(B_2 - B_1)} , \tag{5.1}$$

with $c = 4.632 \times 10^{14}\ \mathrm{T^{-1}m^{-2}}$, λ the neutron wavelength and θ_0 the inclination angle between the leg and base of the isosceles triangular face of the two triangular coils. If a small angle scattering sample is inserted in the beam, it will cause a dampening of the amplitude of the spatial modulation as the scattering function will redistribute intensities between the minima and maxima, which can be seen as a convolution of the modulation function with the scattering function. The Spin-Echo approach also allows for two measurements with opposite initial spins and hence opposite modulation phases. Normalising such two measurements with eq. (5.2) to obtain the attenuation corrected modulation, one can easily remove not only the sample attenuation contribution to the signal but this also constitutes as an inherent correction for beam imhomogeneities. When calculating the attenuation corrected modulation,

M_C:

$$M_C = \frac{I_\uparrow - I_\downarrow}{I_\uparrow + I_\downarrow} \,, \tag{5.2}$$

The visibility is given by:

$$V = \max(M_C) = |\min(M_C)| \tag{5.3}$$

and the modulation curve will be centred around $M_C = 0$ with a maximum possible amplitude of 1 (when visibility is 1). V (V_0) is the visibility of the spatially modulated signal, M_C ($M_{C,0}$), with (without) sample in the beam. The probed correlation length, or size-parameter, can similar to SESANS be given as the Spin-Echo length, δ^{SE}, [3] with:

$$\delta^{SE} = \frac{c\lambda^2 L_S (B_2 - B_1)}{\pi \tan\theta_0} = \frac{\lambda L_S}{\zeta} \,, \tag{5.4}$$

with L_S being the sample-detector distance. The normalised visibility (V/V_0) can then be modelled by the SESANS correlation function, G, [36, 20, 1, 43]:

$$\frac{V(\delta^{SE})}{V_0} = \exp\left\{\Sigma t\left[G(\delta^{SE}) - 1\right]\right\} \,, \tag{5.5}$$

where t is the sample thickness and Σ is the total scattering cross section of the sample, which for a two-phase system is given by: $\Sigma = \lambda^2 (\Delta\rho)^2 \phi (1-\phi) \zeta$, [1, 42], with $\Delta\rho$ being

the scattering length density contrast, ϕ the volume fraction of one phase, and ξ the correlation length perpendicular to the neutron beam. In order to model our data by the real space correlation function we normalise by sample thickness and – since we are doing ToF experiments with a white beam – by wavelength, such that the data is of the form:

$$\frac{\ln\left[\frac{V(\delta^{SE})}{V_0}\right]}{\lambda^2 t} = \Sigma\left[G\left(\delta^{SE}\right) - 1\right] \ . \tag{5.6}$$

Figure 5.1 shows the relationship between the horizontal position on the detector and the modulation signal for three different wavelengths/periods. With a small angle scattering sample in the beam the modulation is dampened by a factor depending on the scattering power of the sample and the correlation length with respect to the Spin-Echo length. When using the reported [49] sine curve fitting of the visibility signal to obtain the scattering information, the smallest spatial unit that can be analysed, and hence any direct spatial image resolution, is limited to a minimum horizontal width of one modulation period. However, it can be seen that in principle the visibility information can be extracted from every point in the modulation curve except at $M = 0$, when directly dividing the sample modulation by the open beam modulation. This in contrast

to the earlier spatial fitting method allows for extracting visibility values with full pixel resolution, and hence obtaining the scattering signal for every pixel analysed. The quality of the signal is, however, somewhat dependent on the phase of the modulation and decreases towards phases with $M = 0$, where such signal vanishes.

The location of areas with limited or no visibility information in such analysis depends on the wavelength and hence Spin-Echo length. If the spatial resolution is sufficiently good compared to the modulation frequency, the "dead spot" area (but not their spatial distribution) will be independent of the modulation period. In principle the problem of local information gaps can be overcome by multiple measurements and the use of a phase coil, adjustment of the relationship between fields in precession arms, change of a π-flipper position, or even movement of the sample such that the echo is moved horizontally a quarter of a period. However, this will increase the measuring time. As the position of information depleted areas in the image shifts with neutron wavelength, i.e. Spin-Echo length, only a negligible range will be missing in the scattering curves derived in each pixel, which will in general not hinder fitting and hence quantification. This is shown in Figure 5.2 where calculated scattering curves in single pixels at different detector locations are shown with their "dead spots". Especially the "dead spots" which are located closest to the

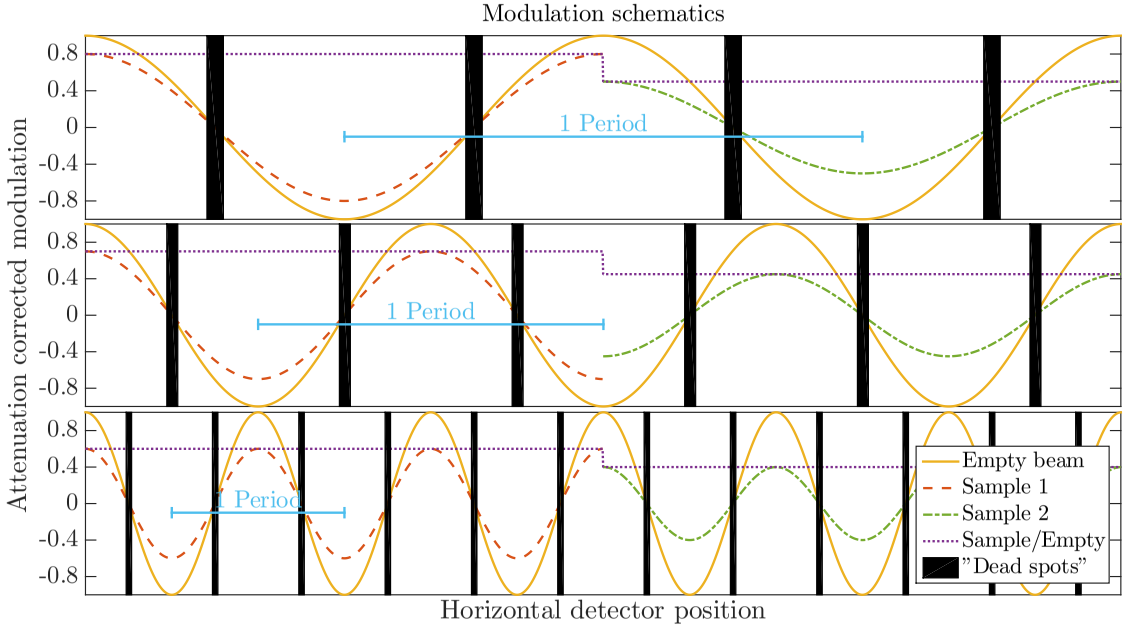

Figure 5.1 Depiction of the modulation for three different modulation periods. The empty beam curve has a maximum visibility, and when a sample is inserted the amplitude is dampened. To obtain the amplitude information through the fitting of sinusoidal functions, a full modulation period is used, indicated by the horizontal blue bars. The "dead spots" marks areas where there is no information for the pixel-by-pixel analysis.

echo position can be desirable to move, since at this location a single "dead spot" covers the largest Spin-Echo range and therefore might hide features of the scattering curve (see Figure 5.2 and vertical white lines in Figure 5.3 at approximately the 200th horizontal detector pixel). However, the modulation signal is strongest closest to the echo [39], so moving far away from echo is not advantageous.

We have in our work analysed the same data set using the sinusoidal curve fitting approach [49] and the pixel-by-pixel division of visibility, in order to compare the methods and reveal their strengths and weaknesses. The pixel-by-pixel division of visibility will decouple the resolution from the modulation period, however, it will not decrease the resolution to the pixel size even if the divergence of the neutron beam is ignored. The fundamental limit is the overlap of scattering functions of different regions of interest. The size of this overlapping range, or resolution, depends on the particle sizes, sample-detector distance (L_S) and used neutron wavelength. In the most simple case of a hard sphere the scattering function is described by:

$$F(q) = \left(\frac{3}{qR} \frac{\sin(qR)}{(qR)^2} - \frac{\cos(qR)}{qR} \right)^2 , \qquad (5.7)$$

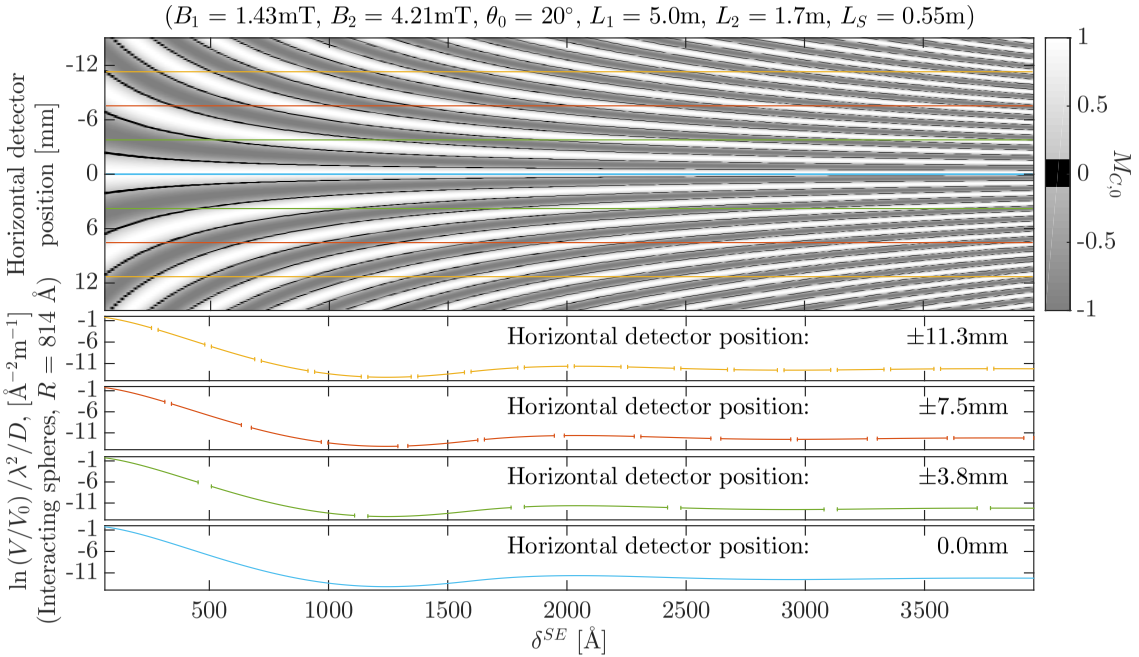

Figure 5.2 Calculations of scattering curve "dead spots" at different detector positions for a sample of hard spheres in high concentration investigated by SEMSANS using pixel-by-pixel analysis. Each curve corresponds to the signal in a 55×55 μm^2 pixel and it can be seen that at the echo position a scattering signal can be extracted for the full Spin-Echo range, whereas at positions away from echo losses of signal occur when $M_{C,0}$ gets close to zero.

where R is the radius of the particle and

$$q = \left(\frac{4\pi}{\lambda}\right) \sin\left(\frac{\theta}{2}\right) . \tag{5.8}$$

With θ being the scattering angle and x the position on the detector, $x = L_S \tan(\theta)$. If for an arbitrary resolution limit, a value of 10% of the intensity is taken where the scattering signal can be neglected, a value for $(qR) = 3.1$ is found in eq. (5.7). This will result in an "effective scattering range" x_1 on the detector for a single particle with radius R_1,

$$x_1 = 2L_S \tan\left(\arcsin\left[\frac{3.1\lambda}{4\pi x_1}\right]\right) . \tag{5.9}$$

In practice a resolution σ will be defined by the minimal distance of two regions with different scattering functions, or different radii, R_1 and R_2.

$$\sigma = 2L_S \tan\left(\arcsin\left[\left(\frac{3.1\lambda}{4\pi}\right)\left(\frac{R_1 + R_2}{R_1 R_2}\right)\right]\right) . \tag{5.10}$$

In our case with particles of about $R_1 = 500$ nm and $R_2 = 80$ nm and for a wavelength of 3 Å, a resolution of about 1.2 mm is found, which is significantly smaller than the modulation period of 3 mm.

5.4 Measurements

Our measurements were performed at the Reactor Institute Delft at TUDelft on the SEMSANS setup described in [49], at a thermal source, where the pulsed beam was created using two co-rotating choppers in optically blind mode providing a wavelength resolution of $\sim$ 5% $\delta\lambda/\lambda$ [54]. The triangular field coils were placed at $L_1 = 5.0$ m and $L_2 = 1.7$ m from the detector, with fields of $B_1 = 1.43$ mT and $B_2 = 4.21$ mT and inclinations angles of $\theta_0 = 20^\circ$. Our sample setup, which consisted of a combination of three different sample types, was placed at $L_S = 0.55$ m in front of the detector. The supermirror multi-channel polariser was oriented so that initial polarisation was vertical whereafter two adiabatic $\pi/2$-rotators were used to choose between spin up or down setting and to rotate the neutron spin into the horizontal plane. Two vertical precession fields were used between polariser and analyser to control the neutron spin and before the analyser a second adiabatic $\pi/2$-rotator pair was used to rotate the neutron spins back to the vertical plane. The supermirror multi-channel analyser was oriented in this plane, such that effects from the structure of the analyser (and polariser) would be perpendicular to the modulation and therefore having no influence on the observed modulation. The Spin-Echo range covered was from about 75 Å to 1750 Å.

Since our proof-of-principle measurements were performed at a low-flux instrument, we examined three different regions of interest (ROIs) covering areas with iron powder, no small angle scattering sample, and dispersed polystyrene colloids in D_2O respectively. Each ROI corresponds roughly to a detector area of approximately 50 mm^2 with a detector-pixel size of 55×55 μm^2 [51, 52]. Measurement time for one initial spin direction with or without samples in the beam was of the order of 3.5 hours, making the total measurement time approximately 14 hours.

5.5 Results

To improve the quality the obtained images for each Spin-Echo length the images were first filtered using an inverse scale space filter [12] to reduce noise and were averaged over the vertical direction of the ROI, i.e. perpendicular to the modulation direction, which was horizontal. Obviously at an instrument with sufficiently high flux and quality of components the vertical resolution can be as good as the collimation and detector resolution allow.

Figure 5.3 shows the modulation as a function of Spin-Echo length and horizontal detector position. The normalised modulation, $M_C/M_{C,0}$, was calculated and as

shown in Figure 5.3 Part 2 **h-j**, where white stripes indicate the positions in time and space with missing information.

As it can be seen in Figure 5.3 **h-j** the normalised visibility and the modulation expectedly decreases with increasing Spin-Echo length when there is a small angle scattering sample present. It can also be seen that for long Spin-Echo lengths (long wavelengths) there is a drop in statistics due to the reduced flux of the neutron source at these wavelengths. However, having a higher flux and/or a longer measuring time (possibly in combination with a cold instead of thermal neutron source) will improve statistics and the accessible range of correlations lengths in this regime.

For each Spin-Echo length (time frame) and ROI the 1D modulated data vs horizontal detector position was fitted with a sinusoidal function thereby obtaining the $V(\delta^{SE})$ and V_0 information [49] displayed as the "sine fitting" curves in Figure 5.4, where they are compared to curves obtained through our novel approach of dividing the modulation functions directly. Reference curves for the three sample types (iron powder, no sample, and polystyrene colloids) are shown as well. In order to obtain the "modulation curve division" curves of the relative visibility as a function of Spin-Echo length for a given ROI we averaged first along the vertical detector position, calculated $M_C/M_{C,0}$, and averaged along the horizontal detector position for each time frame. $V_0 < 0.1$ was set as the threshold

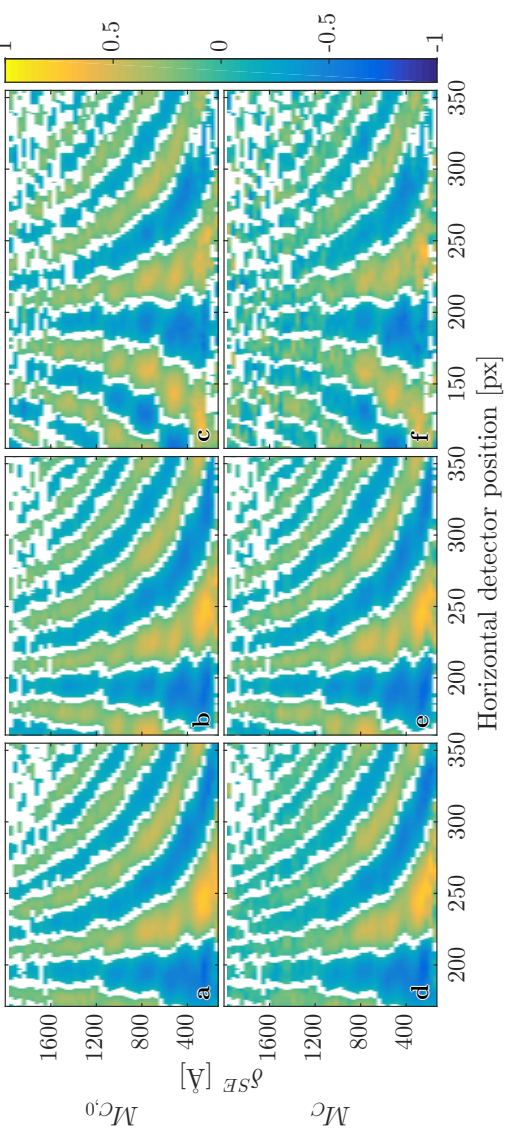

Figure 5.3 Part 1/2: Images **a-f** show data from the ROIs which has been averaged along the vertical direction on the detector, where the colorscale corresponds to the attenuation corrected modulation and white areas are without information due to either "dead spots" or low counting statistics. The columns corresponds to the three different sample areas, and images **a-c** (**d-f**) are without (with) the sample in the beam.

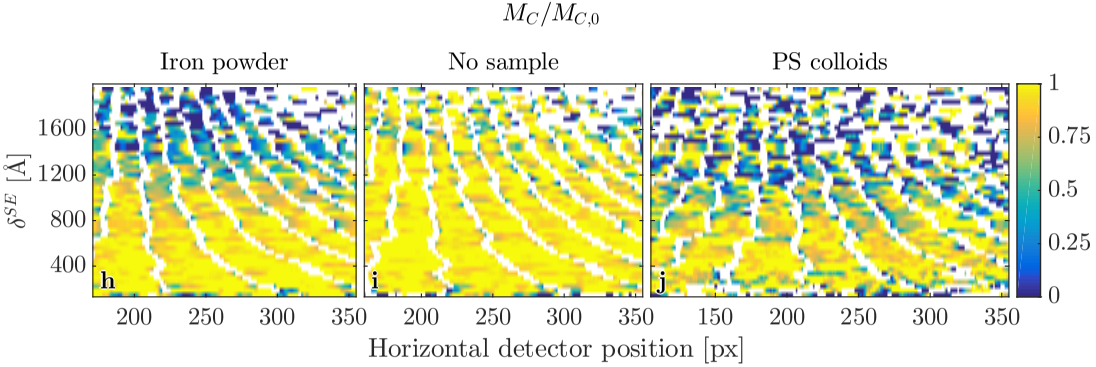

Figure 5.3 Part 2/2: Images **h-j** show the normalised visibility (eq. (5.2)-(5.3)). The columns corresponds to the three different sample areas.

for determining the location of "dead spots". There is a high level of agreement between the curves from the two different methods of data analysis, though at long Spin-Echo lengths our novel approach seems to be more robust with respect to noisier data and shows better precision and better correspondence with the reference curves.

5.6 Conclusion

With our novel data analysis approach it was demonstrated that the ratio of modulation amplitudes measured in each pixel for spin up and spin down configurations can provide the most accurate information on the scattering signal, and most importantly with full pixel resolution of the detector. Additionally this approach is more straight forward and less time consuming and computational intense than the previously used fitting routines. This makes it not only attractive for quantitative SEM dark-field imaging but also for conventional measurements of (very) small angle scattering.

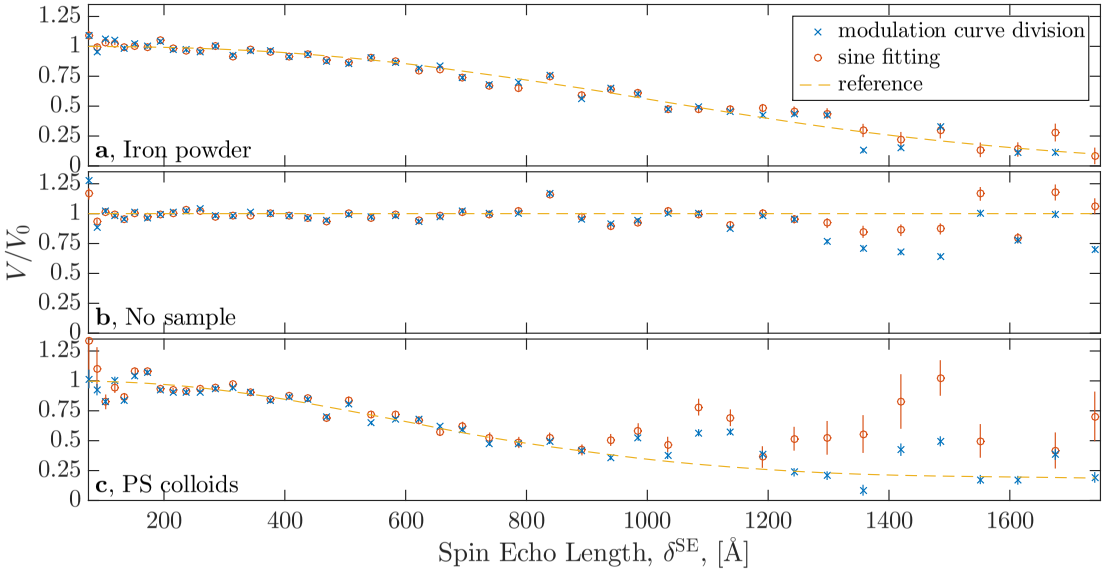

Figure 5.4 Comparison of relative visibilities dependent on the Spin-Echo length obtained through sine fitting and modulation curve division. The reference curves in **a** and **c** are based upon fits of higher resolution SESANS measurements performed individually on the same samples at RID. The model used for the reference curve in **a** is of a random two-phase media [1] and the model used for the reference curve in **c** is for hard spheres [14]. For the reference curve in **b**, V/V_0 is equal to 1 for all Spin-Echo lengths as there is no small angle scattering sample present.

Chapter 6

Wavelength-Independent Constant Period Spin-Echo Modulated Small Angle Neutron Scattering

Authors: Morten Sales[a], Jeroen Plomp[b], Wim G. Bouwman[b], Anton S. Tremsin[c], Klaus Habicht[d] and Markus Strobl[a,e].

Affiliations: [a]University of Copenhagen, The Niels Bohr Institute, Denmark, [b]Delft University of Technology, Reactor Institut Delft, The Netherlands, [c]University of California at Berkeley, Space Sciences Laboratory, USA,[d]Helmholtz Centre Berlin for Materials and Energy (HZB), Germany, [e]European Spallation Source AB, Sweden.

Introduction to Article

This article is to be submitted. The data reduction and analysis and the figures have been created by me with input from Markus Strobl. The text was co-written by Markus Strobl and me with input from the other authors.

6.1 Abstract

Spin-Echo Modulated Small Angle Neutron Scattering (SEMSANS) in Time-of-Flight (ToF) mode has been shown to be

a promising technique for measuring (very) small angle neutron scattering (SANS) signals and performing quantitative Dark-Field Imaging (DFI), i.e. SANS with 2D spatial resolution. However, the wavelength dependence of the modulation period in the ToF Spin-Echo mode has so far limited the useful modulation periods to those resolvable with the limited spatial resolution of the detectors available. Here we present our results of an approach to keep the period of the induced modulation constant for the wavelengths utilised in ToF. This is achieved by ramping the magnetic fields in the coils responsible for creating the spatially modulated beam in synchronisation with the neutron pulse, and hence in dependence of the wavelength in the set-up at each specific time, in order to keep the modulation period constant for all wavelengths. Such a set-up enables to decouple spatial detector resolution from the resolution of the modulation period by the use of slits or gratings in analogy to the approach in grating-based neutron DFI.

6.2 Introduction

SEMSANS has been proven to be possible and a useful SANS tool for both utilising either a monochromatic beam [48], or a pulsed neutron beam [47, 39], just as in conven-

tional SANS [50]. It has also been shown that the method holds the outstanding potential to measure SANS with additional spatial resolution on the macroscopic scale of neutron imaging [49, 38] in analogy to grating based DFI [43].

In general SESANS and in particular SEMSANS-based DFI is highly analogous to the grating interferometer based dark-field method. However, to date the two methods operate at very different ranges of modulation periods and correspondingly also scattering vector and resolvable size ranges. For monochromatic SEMSANS just as for grating interferometry the period of the spatial beam modulation during an exposure is constant. This allows for analysis of the modulation utilising a phase-stepping, i.e. scanning, approach with an absorption grating matching the period of the modulation in front of the detector [32]. Either the modulation or the analyser grating is shifted across the beam and a number of images are recorded over one period. This in turn enables periods to be resolved which are smaller than the detector resolution, like usually done in DFI with grating interferometers. In SEMSANS the periods are currently also limited by the magnetic field set-ups, but in particular the ToF realisation and the spatial detector resolution constitute the main limitations.

For SEMSANS a polarised neutron beam is laterally modulated in the detector plane by modulating the po-

larisation with two triangular field regions [8, 2, 3] with fields in opposite directions, since the precession angle of the neutron spin will depend on the horizontal position of neutron trajectory through the triangular fields. The modulated polarisation across the beam is turned into an intensity modulation by the use of a polarisation analyser.

Downstream from the analyser at the detector position the now spatial modulation has a period given by [8]:

$$\zeta = \frac{\pi \tan \theta_0}{c\lambda \left(B_2 - B_1\right)} \,, \tag{6.1}$$

with B_1 and B_2 being the fields in the triangular coils, θ_0 the inclination angle of the triangular coils with respect to the optical axis, the Larmor constant $c = 4.632 \times 10^{14}$ T^{-1}m^{-2}, and λ the wavelength. It can be seen that for a constant angle, θ_0, and fields, B_1 and B_2, in the triangular coils, the period will decrease with increasing wavelength. Hence, throughout a neutron pulse in a ToF instrument, where neutrons with higher energy (velocity) and hence shorter wavelengths arrive at the detector first, the modulation period is becoming inversely smaller proportional to the specific ToF of a neutron. The time, t, it takes for a neutron to travel the distance, L, (from pulse generating choppers to detector), is, using the de-Broglie equation, given by:

$t_{TOF} = \alpha L\lambda$, where $\alpha = m_N/h = 2.528 \times 10^{-4}$ s/m/Å, and m_N is the neutron mass and h is the Planck constant.

As the length scale probed, which is characterised by the Spin-Echo length, δ^{SE}, is given by:

$$\delta^{SE} = \frac{\lambda L_S}{\zeta} = \frac{c\lambda^2 L_S(B_2 - B_1)}{\pi \tan\theta_0}\,, \tag{6.2}$$

the probed scale is proportional to the wavelength, and hence also ToF, squared. This is the case because both the period, which defines the scattering angle probed, and the scattering angles, which relate to the scattering structure sizes, are linearly wavelength dependent.

In SEMSANS the magnetic fields in the two triangular precession regions and their distances to the detector have to fulfil the focusing condition $B_1L_1 = B_2L_2$ in order to achieve an optimised modulation in the detector plane. This condition is wavelength independent, and hence the method can be exploited efficiently in ToF mode. In contrast to neutron grating interferometry the set-up is optimised to a specific wavelength because the induced phase shift in the phase gratings as well as the fractional Talbot distance, at which an optimised modulation can be achieved, are wavelength dependent [53, 32]. Therefore, although it has been shown that contrast can still be achieved over a range of a few angstroms [26], the set-up is

generally not well suited for ToF applications, in particular with respect to a significant range to be probed efficiently.

When, however, considering to keep the modulation period constant in a ToF SEMSANS experiment either the magnetic field in the precession coils or their angular set-up has to be adapted in synchronisation with the ToF pulses. Given the frequencies of about 10 Hz to 50 Hz in most neutron ToF applications and the potential to adapt and synchronise the magnetic fields remotely by the supplied electrical currents, such option was chosen over a mechanical adaptation of the angles of the field regions. In order to keep the modulation period constant, the required field value of e.g. B_1 can easily be calculated by:

$$B_1 = B_2 \frac{L_2}{L_1} = \frac{1}{\lambda} \frac{\pi \tan\theta_0 L_2}{c\zeta(L_1 - L_2)} = \frac{\alpha L}{t} \frac{\pi \tan\theta_0 L_2}{c\zeta(L_1 - L_2)} \,. \quad (6.3)$$

With this ToF – and hence wavelength – dependence of the field and (see Fig. 6.1 **a**) the therefore constant modulation period, the Spin-Echo length will now scale linearly with wavelength and not anymore with the square of the wavelength as shown in Fig. 6.1 **b**. The result of this is that for a given wavelength spectrum the range of length scales probed will be smaller when keeping the period constant. This drawback, however, will for the right purposes be more than compensated by the possi-

bilities offered. Moreover, the broader Spin-Echo length range possible with constant fields in the triangular precession regions is only attainable if the correspondingly decreasing modulation period is resolvable by the detector (see Fig. 6.1 **c**). It can bee seen in Fig. 6.1 that in order to gain the broader Spin-Echo length range using constant fields, lower field strength but higher detector resolution is needed compared to the ramped field set-up, which on the other hand is limited by the maximum field strength achievable in the triangular precession coils. While the detector resolution limit concerns the long correlation lengths, the high field requirement for the constant period case concerns the short spin echo lengths.

6.3 Measurements

The measurements were performed at the Reactor Institute Delft, TUDelft, The Netherlands. The pulsed beam was created using a co-rotating optically blind double chopper set-up [54], with about 5% $\delta\lambda/\lambda$ at the detector and a pulse frequency of 50 Hz. The neutrons were polarised and analysed using multi-channel supermirrors, and the neutron spin-rotations were controlled using V-coils (Delft $\pi/2$-rotators [18]). The current in the triangular coils was controlled with a pulse generator for each coil with a peak mag-

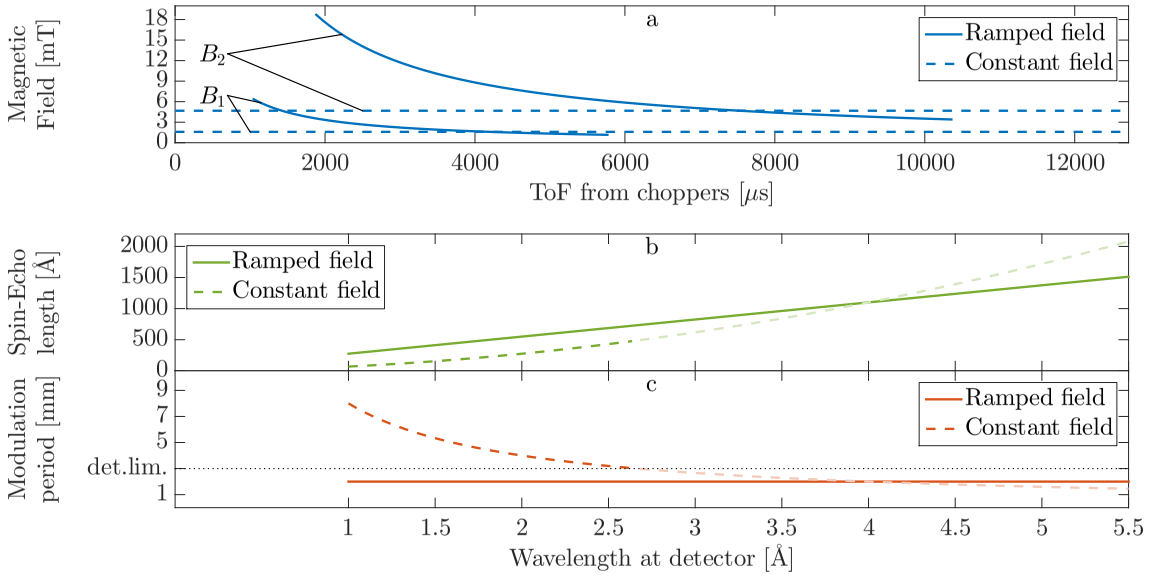

Figure 6.1 Calculated exemplifying curves. **a**: ToF dependence of magnetic fields in ramped field set-up. Curves for constant fields set-up shown for comparison. **b** and **c**: Spin-Echo length, δ^{SE}, and modulation period, ζ, as a function of wavelength for ramped and constant field set-ups. The limit of a detector being able to resolve a minimum modulation period of 3 mm is marked in **b** and **c**. ($L_S = 0.55$ m, $L_1 = 5.0$ m, $L_2 = 1.7$ m, $L = 9.15$ m, $\theta_0 = 20°$).

netic field of about 3 mT. The data was recorded using a microchannel plate detector with a pixel size of 55×55 μm^2 and timepix readout [51, 52] with time frame exposure of 48 μs (rebinned into 96 μs).

Measurements with constant magnetic fields in the triangular coils, and therefore wavelength dependent modulation period, were recorded as well for comparison.

6.4 Results

Fig. 6.2 shows the measurements of the spatial modulation with and without ramped fields as a function of wavelength. It can be seen that with constant magnetic field in the triangular precession coils the modulation period decreases with increasing wavelength. When the magnetic fields are ramped the period could be stabilised but still small changes are observed with the current set-up. Furthermore, it can be seen that when ramping the magnetic fields, the modulation pattern shifts across the detector surface, since the magnetic field strengths scale with the distance from coil to detector and therefore the Spin-Echo position is being moved horizontally across the detector surface during the neutron pulse. This means that in order to keep the modulation stationary as well as with a constant period, a third ramped precession field without

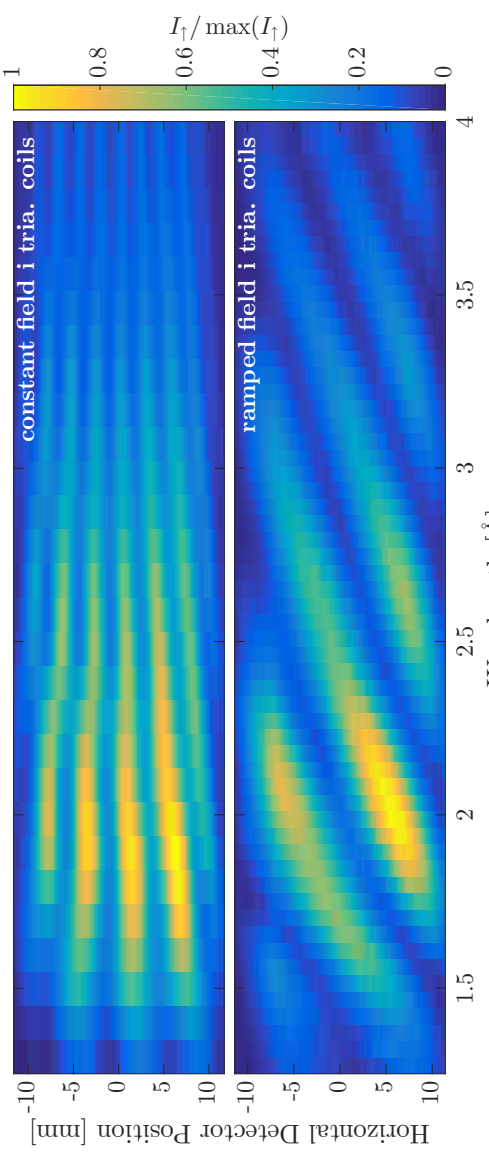

Figure 6.2 Spin-Echo induced spatial modulation without and with neutron pulse synchronised ramped magnetic fields in triangular coils.

inclined field surface is necessary to compensate for the difference in field strength between B_1 and B_2.

In Fig. 6.3 **a, b, c** examples of the modulation pattern for three different wavelength are shown for both the ramped field and the constant field set-up. It can be seen that we succeeded in reducing the wavelength dependence of the modulation period significantly. It is kept constant first, in a range where field differences are large (see Fig. 6.2), but accuracy in synchronisation was not sufficient for longer wavelengths, where the sensitivity of period versus field value increases. As also further illustrated in Fig. 6.4, where the period is shown as a function of wavelength, the period still decrease with increasing wavelength above 1.6 Å, indicating that the ramped field in the triangular coils in our set-up was not sufficiently matched to the requirements of the neutron pulse. This, however, is a simple limitation of the available equipment in our proof-of-principle set-up. With appropriate equipment the synchronisation of the magnetic fields with the neutron pulse and their accuracy will not be limited by the response of the power supply when the induction in the coils are taken into account carefully.

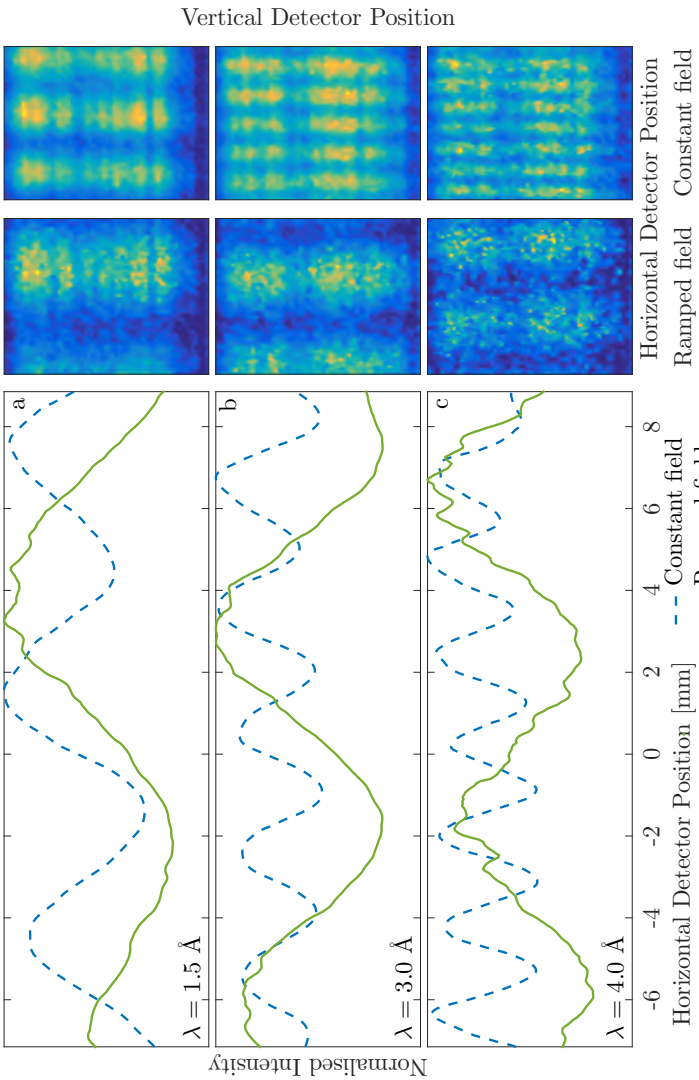

Figure 6.3 **a, b, c** show examples of modulation curves for three different wavelengths, with the corresponding detector images on the right.

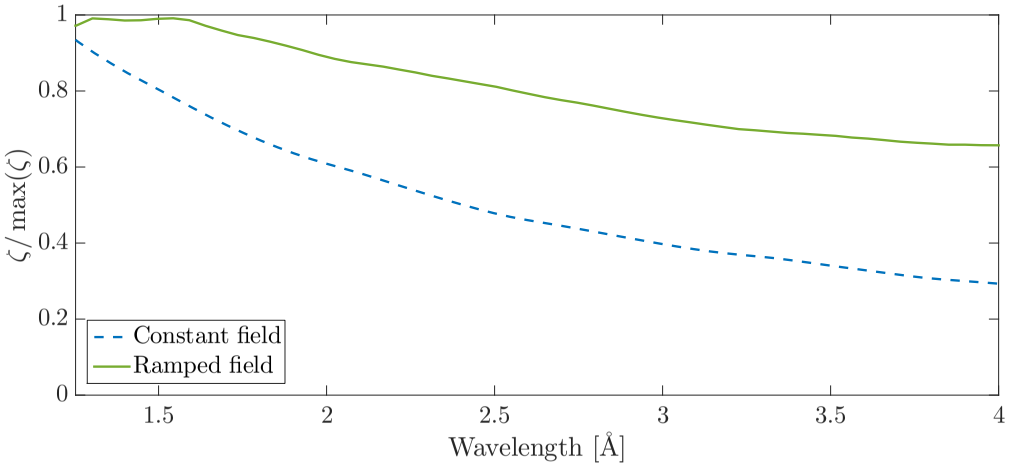

Figure 6.4 Comparison of the modulation period as a function of wavelength for constant and for ramped fields in the triangular coils.

6.5 Conclusion

We have successfully demonstrated with our proof-of-principle instrumental set-up that ramping the magnetic field in the triangular coils of a ToF SEMSANS instrument in synchronisation with ToF neutron pulses, makes it possible to keep the spatial modulation period constant during the experiment independent of the ToF and neutron wavelength. This opens up the possibilities for performing quantitative Dark Field Imaging in ToF mode and using a grating analyser to resolve periods beyond the resolution of the detector. This will enable to extend the structure size range amenable by Spin-Echo Modulated Dark Field Imaging (SEM-DFI) as well as in measuring (very) small angle scattering signals with relaxed collimation and a single pixel detector behind a grating also in ToF mode. The disadvantage of the approach is as demonstrated the limitations in the Spin-Echo range compared to the constant field set-up as long as not limited by detector resolution. However, this is more than balanced by an extended wavelength and period range amenable with this technique using a grating analyser in ToF.

Chapter 7

Final Conclusion

Through our first investigation into Spin-Echo Modulated Small Angle Neutron Scattering in Time-of-Flight mode using an absorption grating analyser and a single pixel detector for resolving the signal, and combining this with Monte-Carlo ray-tracing simulations, we gained valuable insight into the magnetic field dependence of the modulation pattern. Especially the importance of keeping the signal at the Spin-Echo position in order to obtain the highest signal quality was established.

After establishing the functionality of our instrument, we developed upon these initial results, where we were able to further improve our set-up, and with the addition of a both spatial and time sensitive detector, we successfully measured polychromatic quantitative Dark-Field imaging

on a multi-sample set-up. With this we could extract small angle scattering information of selected regions of interest in the obtained images corresponding to different samples. The extracted information corresponded well with reference curves, though with our proof-of-principle set-up at a low-flux thermal source, we were limited to a somewhat narrow Spin-Echo range. The curves were obtained through multiple sinusoidal curve fittings in order to obtain the visibility values from the modulation pattern. This method of data analysis is limited to spatial resolutions of minimum one modulation period.

Therefore we investigated an alternative method for analysing SEMSANS data, where the relationship between the attenuation corrected modulation in individual areas of sub-period size with and without sample was used to extract the small angle scattering information. Possible improvements in accuracy over the sine fitting method was observed and this in combination with the reduction in complexity and computational demand underlined the usability of the novel method of analysis. The downside of having areas without information when the modulation is close to zero was found to be negligible in most cases.

Finally we were able to ramp the field in triangular precession regions in synchronisation with the neutron pulse in order to diminish the wavelength dependence of the modulation period. With a constant modulation period

and phase it is possible to go to spatial resolutions beyond the limit set by the detector by using an absorption grating to resolve the signal. Moreover, this approach also opens up the possibility of using a single pixel detector and a grating to achieve spatial resolution.

All together our investigations of SEMSANS in ToF mode have shed light on a promising technique bridging the gap between small angle scattering and imaging, measuring both simultaneously, thereby covering length scales at several orders of magnitude in one measurement.

At the powerful pulsed neutron sources of the future, such as the European Spallation Source, our ToF SEMSANS instrument would be able to excel as an important tool for investigations of a wide variety of systems.

Appendix A

Experimental evidence for lamellar magnetism in hemo-ilmenite by polarized neutron scattering

The work presented in the article below was the basis of not only the article but also my PhD midway-project (corresponding to my Master's Thesis).

The article describes the investigation of the magnetic properties of Hemo-Ilmenite, in order to find an explanation for its anomalous remanent magnetisation, through the use of polarised neutron diffraction under various external magnetic fields and temperatures on a single crystal Hemo-Ilmenite sample from southern Norway [6].

My contribution was being part of the team carrying out the main neutron scattering experiments, that were the basis for the work presented. I performed the data treatment and analysis and created the figures in the article presenting the data. Furthermore I provided input to the article text written by Erik Brok. (Note that each inserted article page is spread across two pages in this text.)

PHYSICAL REVIEW B **89**, 054430 (2014)

Experimental evidence for lamellar magnetism in hemo-ilmenite by polarized neutron scattering

Erik Brok,[1,2] Morten Sales,[3,4] Kim Lefmann,[3] Luise Theil Kuhn,[5] Wolfgang F. Schmidt,[6] Bertrand Roessli,[7] Peter Robinson,[8] Suzanne A. McEnroe,[9] and Richard J. Harrison[10,*]

[1]*Department of Physics, Technical University of Denmark, DK-2800 Kgs Lyngby, Denmark*
[2]*Center for Electron Nanoscopy, Technical University of Denmark, DK-2800 Kgs Lyngby, Denmark*
[3]*Nano-Science Center, Niels Bohr Institute, University of Copenhagen, DK-2100 Copenhagen Ø, Denmark*
[4]*Department for Methods for Characterization of Transport Phenomena in Energy Materials, Helmholtz-Zentrum Berlin Für Materialen und Energie GmbH, D-14109 Berlin, Germany*
[5]*Department of Energy Conversion and Storage, Technical University of Denmark, DK-4000 Roskilde, Denmark*
[6]*Jülich Centre for Neutron Science JCNS, Forschungszentrum Jülich GmbH, Outstation at ILL, 38042 Grenoble, France*
[7]*Laboratory for Neutron Scattering, Paul Scherrer Institute, 5232 Villigen, Switzerland*
[8]*Geological Survey of Norway, N-7491 Trondheim, Norway*
[9]*Norwegian University of Science and Technology, N-7491 Trondheim, Norway*
[10]*Department of Earth Sciences, University of Cambridge, CB2 3EQ, United Kingdom*

(Received 13 November 2013; published 26 February 2014)

Large local anomalies in the Earth's magnetic field have been observed in Norway, Sweden, and Canada. These anomalies have been attributed to the unusual magnetic properties of naturally occurring hemo-ilmenite, consisting of a paramagnetic ilmenite host (α-Fe_2O_3-bearing $FeTiO_3$) with exsolution lamellae ($\approx 3\ \mu$m thick) of canted antiferromagnetic hematite ($FeTiO_3$-bearing α-Fe_2O_3) and the mutual exsolutions of the same phases on the micron to nanometer scale. The origin of stable natural remanent magnetization (NRM) in this system has been proposed to be uncompensated magnetic moments in the contact layers between the exsolution lamellae. This lamellar magnetism hypothesis is tested here by using polarized neutron diffraction to measure the orientation of hematite spins as a function of an applied magnetic field in a natural single crystal of hemo-ilmenite from South Rogaland, Norway. Polarized neutron diffraction clearly shows that the ilmenite spins do not contribute to the NRM and that hematite spins account for the full magnetization at ambient temperature. Hematite sublattice spins are shown to adopt an average angle of 56° with respect to a saturating magnetic field, which is intermediate between the angle of 90° predicted for a pure canted moment and the angle of 0° predicted for a pure lamellar moment. The observed NRM is consistent with the vector sum of lamellar magnetism and canted

antiferromagnetic contributions. The relative importance of the two contributions varies with the length scale of the microstructure, with the lamellar contribution increasing when exsolution occurs predominantly at the nanometer rather than the micrometer scale.

DOI: 10.1103/PhysRevB.89.054430 PACS number(s): 75.25.−j, 91.60.Pn, 75.70.Cn, 75.75.−c

I. INTRODUCTION

The mineral intergrowth hemo-ilmenite consists of an ilmenite host ($FeTiO_3$) with several populations of hematite (α-Fe_2O_3) exsolution lamellae. Hemo-ilmenite has been studied extensively because of its importance as a source of anomalies in the magnetic field of the Earth [1,2] and potentially also on Mars [3], and because of its unusual magnetic properties that are not explained by the magnetic properties of the individual constituent minerals. Natural samples of hemo-ilmenite have a large and extremely stable natural remanent magnetization, which is believed to be related to the fine exsolution structure of the intergrown hematite and ilmenite phases [2,4]. Solid solution hematite-ilmenite [xFeTiO$_3$-(1−x)Fe$_2$O$_3$] with compositions in the range $0.5 < x < 0.85$ are magnetic semiconductors [5,6] and a detailed understanding of the complex magnetic properties of natural samples of nanostructured hemo-ilmenite could lead to important discoveries that have application potential in spintronics devices [7–9]. Hemo-ilmenite consists of the minerals ilmenite ($FeTiO_3$) which is paramagnetic at room temperature, but is AFM ordered below a Néel temperature of about 58 K [10], and hematite (α-Fe_2O_3) which is antiferromagnetic (AFM) with a Néel temperature of 955 K [11]. The quoted Néel temperatures are for the pure minerals (end members) and the Néel temperatures of the hematite and ilmenite phases of our natural sample are expected to be lowered because of cation substitution.

Hematite crystallizes in the $R\bar{3}c$ (corundum) structure with the Fe^{3+} magnetic moments ferromagnetically aligned within the basal (ab) planes of the hexagonal structure, while moments on adjacent planes are antiparallel apart from a small canting of approximately 0.065° [11]. The canting, which is in the basal plane, gives a small net magnetic moment, and hematite is thus often referred to as a weak ferromagnet, rather than an antiferromagnet. There are three easy axes in the basal plane giving six possible antiferromagnetic domains. In all of these domains the spins are in the basal plane and nearly perpendicular to one of the hexagonal a axes. In pure bulk hematite the spins undergo the so-called Morin transition at ($T_M \approx 264$ K [12,13]). The Morin transition is a spin-flop transition, where the two AFM sublattices change their spin direction from perpendicular to parallel to the c axis. However, substitution of even small amounts (≈1%) of Ti in hematite is known to suppress the transition [12,13] and it does not occur

*rjh40@esc.cam.ac.uk

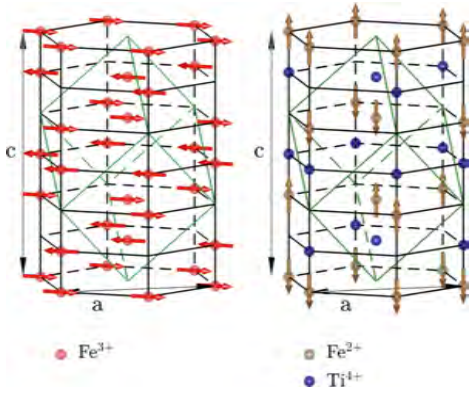

FIG. 1. (Color online) Antiferromagnetic structure of hematite and ilmenite. Left: Magnetic structure of hematite above the Morin transition. Right: Magnetic structure of ilmenite. The oxygen atoms are left out of the drawings, as is the small canting of the Fe^{3+} moments in hematite.

in hemo-ilmenite samples. The crystal structure of ilmenite is $R\bar{3}$ and is identical to the hematite structure, but with alternating layers of Fe^{2+} and Ti^{4+} ions instead of Fe^{3+}. In ilmenite below the Néel temperature the Fe^{2+} moments are

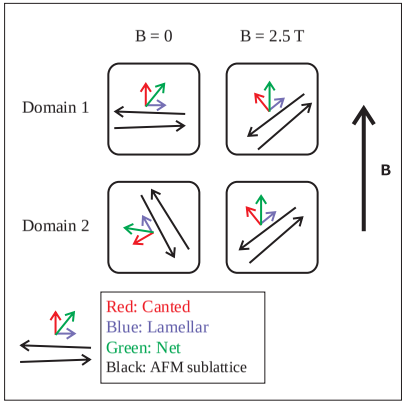

FIG. 2. (Color online) Sketch of the in-plane hematite spin directions and their response to a magnetic field applied applied in the plane. The net moment is the vector sum of the CAF moment, which is almost perpendicular to the AFM sublattice, and the lamellar moment which is parallel to the AFM sublattice. The two "domains" represent two of the possible six antiferromagnetic domains. In zero field the spin orientation depends on the remanent magnetization of the sample. If all six domains are equally represented, or if the spins are randomly oriented, the average spin angle with respect to **B** will be 45°. At a saturating field (2.5 T at room temperature) the net moment is aligned with the field and the average spin orientation is no longer random, but makes an angle with **B** that depends on the proportion of canted and lamellar moments.

aligned along the c axis and antiparallel between adjacent Fe^{2+} layers (see Fig. 1). The lattice parameters of hematite and ilmenite are very similar ($a = b = 5.038$ Å and $c = 13.772$ Å for hematite [11], and $a = b = 5.088$ Å and $c = 14.085$ Å for ilmenite [14,15]) and the two phases are thus able to grow epitaxially together. In natural samples of hemo-ilmenite that slowly cooled around a billion years ago [16], the two phases exhibit a complex exsolution structure that has been investigated with electron microscopy [17], revealing multiple generations of epitaxially aligned intergrown lamellae ranging in thickness from several microns to a few nanometers in the direction of the crystallographic c axis. The lamellae are flattened in the c direction and extended in the basal plane. While the AFM sublattice direction in hematite above the Morin temperature is usually assumed to be within the basal plane, a significant out-of-plane angle of about 30° has been observed in a natural ilmeno-hematite sample showing nanoscale exsolution structure [18].

Natural samples of hemo-ilmenite show a large natural remanent magnetization of around $(1.4–9.1) \times 10^{-3}$ A m^2/kg [19] that cannot be explained by the ferromagnetic contribution from the canted antiferromagnetic (CAF) hematite. The coercivity of the samples as well as the demagnetization temperature [4] is comparable to that of Ti-substituted hematite. The material is not only strongly magnetic, but the magnetism is also very stable. Uncompensated spins in contact layers between hematite lamellae and the ilmenite host, with magnetization aligned by the geomagnetic field at the time the sample exsolved [4,20–22] have been proposed as an explanation for the strong remanent magnetization. This hypothesis, which directly links the nanoscale exsolution structure of the hemo-ilmenite samples to their unusual magnetic properties is termed lamellar magnetism and has been backed by Monte Carlo simulations of the cation ordering during exsolution [4,20], and measurement of exchange bias below T_N of ilmenite have confirmed that the NRM is associated with magnetic moments at the lamellar interfaces [23,24].

The response of the magnetic moments to an applied field can give information about the configuration of the atomic spins. In particular, the response of the hematite spins to a saturating field applied in the basal plane can determine whether or not the lamellar magnetism hypothesis is a plausible explanation for the spin structure in the lamellar system. A sketch of the response of the in-plane magnetic moment to a magnetic field applied in the plane is given in Fig. 2.

Here we use the technique of polarized neutron diffraction to examine a natural hemo-ilmenite sample with an exsolution microstructure showing a range of lamellar sizes from coarse to fine. Through uniaxial polarization analysis we determine the average hematite spin direction in the basal plane as a function of applied magnetic fields up to 2.5 T to directly measure the response of the lamellar moments in order to confirm the validity of the lamellar magnetism hypothesis.

We find that the hematite magnetic moments saturate at an average angle of 56° to the applied field, which is consistent with lamellar magnetism as an important mechanism for the NRM.

II. EXPERIMENTAL DETAILS

A. Sample characterization

The sample is a rectangular solid piece, approximately $12 \times 8 \times 8$ mm^3, with a mass of 1.977 g, cut from a sample of a hemo-ilmenite dike at South Rogaland, Norway. The sample, labeled Pramsknuten 5-1 T, was selected from a larger number of similar pieces by electron backscatter diffraction (EBSD) [19]. The EBSD investigations revealed that the sample is a single crystal of hemo-ilmenite, and established the crystallographic axes with respect to the faces of the sample. X-ray fluorescence (XRF) revealed that the sample is (in percentages of end members) 16.18% hematite composition and 83.82% ilmenite composition [19,25]. The ilmenite part of the sample contains 19.2% of the $MgTiO_3$ end member as well as small amounts (less than 1%) of $MnTiO_3$, $ZnTiO_3$, and $NiTiO_3$. In the hematite part of the sample only small substitutions of Al_2O_3, Cr_2O_3, and V_2O_3 were found (less than 1% of end members). Importantly no ferromagnetic impurity phases were detected. The NRM of the sample was measured to 2.613×10^{-3} A m^2/kg and found to be oriented close to the basal plane (6.1° out of plane) and close to one of the basal plane crystallographic axes (6.8° in-plane angle with nearest hexagonal axis) [19]. The saturation magnetization of the sample is about 0.43 A m^2/kg and the coercivity approximately 60 mT (estimated from magnetization measurements on other pieces of the same rock slab). The saturation magnetization of CAF hematite is 0.404 A m^2/kg [11] and with a mass fraction of 16.88% hematite (assuming 16.18% pure hematite

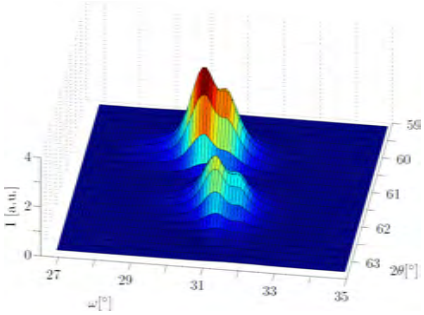

FIG. 3. (Color online) Mapping of the (003) peaks measured at MORPHEUS. 2θ is the scattering angle and ω is the azimuthal rotation angle of the sample. The most intense peak at $2\theta \approx 60°$ is the structural ilmenite reflection and the less intense peak at $2\theta \approx 62°$ is the magnetic hematite reflection. Both peaks have a shoulder, indicating that the sample consists of two distinct crystallites oriented at an angle of approximately 0.6° with respect to each other.

due to the low flipping ratio ($R \approx 4$), at the used wavelength of $\lambda = 4.05$ Å, we here present only the ILL data.

An additional high-field neutron experiment was performed at the RITA-2 triple-axis spectrometer at PSI [28]. Here the hematite (101) reflection was studied by unpolarized diffraction with the same sample orientation, but using a

and 83.82% pure ilmenite in the sample) this can at most amount to a magnetization of the sample of 0.0682 A m^2/kg. Thus, only about 16% of the saturation magnetization can be explained by the weak ferromagnetism of hematite.

B. Neutron scattering experiments

The orientation of the ilmenite and hematite spins was studied by polarized neutron diffraction at the three-axis spectrometer IN12 at Institute Laue-Langevin (ILL), Grenoble, France. We used an initial neutron wavelength of 4.05 Å, selected by a PG (002) monochromator. The beam was polarized by a supermirror bender after the monochromator. The analyzer consists of Heusler (111) crystals, selecting one spin state, and oriented to elastic scattering. To improve the q resolution of the instrument, we collimated the beam, using the sequence guide-open-PG-40'-bender-sample-40'-Heusler-60'-detector. A vertical guide field of 2 to 3 mT was applied along the beam path to prevent neutron depolarization. A Mezei-type spin flipper coil was inserted in the final beam path to allow for 180° rotation of the beam polarization. The flipping ratio of the setup was measured to $R \approx 40$. The sample was aligned with the $\mathbf{a}^*$ and $\mathbf{c}^*$ axes in the scattering plane and was placed in a cryomagnet, capable of applying a ± 2.5 T vertical field. The sample was oriented by the nuclear ilmenite (003) and hematite ($10\bar{2}$) reflections.

A preliminary polarized neutron diffraction experiment was performed at the triple-axis spectrometer TASP at PSI, Villigen, Switzerland [26]. The data from this experiment are in general agreement with the data presented here [27], but stronger cryomagnet, capable of applying a 15 T field.

The crystal structure of the sample was studied with high resolution unpolarized neutron diffraction at the two-axis spectrometer MORPHEUS at PSI. Here we used an incoming wavelength of 4.72 Å and tight collimations: guide-open-PG-20'-sample-30'-detector.

III. RESULTS

Before presenting the results of the polarization analysis experiment we show the results of the experiment on MORPHEUS, which establishes the crystalline quality of the sample. Figure 3 shows a mapping of the structural (003) ilmenite peak and magnetic (003) hematite peak, measured using unpolarized neutrons in the high resolution experiment at MORPHEUS. The peak "shoulders" reveal that the crystal consists of two crystallites that are oriented at an angle of about 0.6° with respect to each other. For the purpose of the investigations presented here this mosaicity of 0.6° is small enough that we consider the sample to be a single crystal.

In the uniaxial polarization analysis experiment performed at IN12 we measured the magnetic (003) hematite reflection to determine the in-plane spin direction. The experimental geometry was as sketched in Fig. 4. Magnetic moments parallel to the incident polarization $\mathbf{P}_i$ will only give rise to non spin flip (NSF) scattering, and the NSF cross section is [29]

$$\sigma^{\mathrm{NSF}} = K M_{\perp z}^2, \tag{1}$$

where K is a constant, and $M_{\perp z}$ is the z component of $\mathbf{M}_\perp$ parallel to $\mathbf{P}_i$, as defined in Fig. 4. $M_\perp(\mathbf{q})$ is the Fourier transform of the magnetic moment density perpendicular to

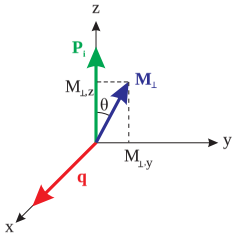

FIG. 4. (Color online) Geometry in the IN12 experiment. $\mathbf{P}_i$ is the incoming polarization vector, $\mathbf{q}$ is the scattering vector, and $\mathbf{M}_\perp$ is the magnetic sublattice magnetization perpendicular to $\mathbf{q}$. The magnetic field is applied in the z direction (parallel to $\mathbf{P}_i$). The angle between $\mathbf{M}_\perp$ and $\mathbf{P}_i$ is called θ.

$\mathbf{q}$, sometimes referred to as the magnetic interaction vector. Moments perpendicular to $\mathbf{P}_i$ will only give rise to spin flip (SF) scattering, and the SF cross section is

$$\sigma^{\mathrm{SF}} = K M_{\perp y}^2, \tag{2}$$

where K is the same constant as in (1), and $M_{\perp y}$ is the component of $\mathbf{M}_\perp$ perpendicular to $\mathbf{P}_i$. From the ratio of the SF to the NSF cross section we can calculate θ—the angle between $\mathbf{P}_i$ and $\mathbf{M}_\perp$,

$$\frac{\sigma^{\mathrm{SF}}}{\sigma^{\mathrm{NSF}}} = \frac{M_\perp^2 \cos^2\theta}{M_\perp^2 \sin^2\theta} = \tan^2\theta. \tag{3}$$

at the structural peak position even in the SF measurement. A nonmagnetic scattering event cannot change the spin state of the neutron and the nonzero SF intensity on the structural position is caused by the fact that the polarization of the beam is not perfect. The data were corrected for imperfect beam polarization using the following formalism:

$$p = \frac{n_\uparrow - n_\downarrow}{n_\uparrow + n_\downarrow} = \frac{R-1}{R+1}, \quad p_\uparrow = \frac{1+p}{2}, \quad p_\downarrow = \frac{1-p}{2}, \tag{4}$$

where p is the beam polarization, $n_\uparrow$ and $n_\downarrow$ are the numbers of neutrons with spin up ($|\uparrow\rangle$) and down ($|\downarrow\rangle$), respectively, and R is the so called flipping ratio. The probability of finding a neutron in $|\uparrow\rangle$ ($|\downarrow\rangle$) is given by $p_\uparrow$ ($p_\downarrow$). The relationship between the true cross sections defined in Eqs. (1) and (2) and the measured intensities I^{NSF} and I^{SF} is then

$$\begin{pmatrix} I^{\mathrm{NSF}} \\ I^{\mathrm{SF}} \end{pmatrix} = \begin{pmatrix} p_\uparrow & p_\downarrow \\ p_\downarrow & p_\uparrow \end{pmatrix} \begin{pmatrix} \sigma^{\mathrm{NSF}} \\ \sigma^{\mathrm{SF}} \end{pmatrix}. \tag{5}$$

The flipping ratio can be calculated from a measurement of a structural peak ($\sigma^{\mathrm{SF}} = 0$):

$$R = \frac{I^{\mathrm{NSF}}_{\mathrm{struct}}}{I^{\mathrm{SF}}_{\mathrm{struct}}} \tag{6}$$

and the true cross sections can then be calculated by inverting Eq. (5). Figure 6 shows the data in Fig. 5 after correction for imperfect polarization. For a full treatment of data corrections in a polarization analysis experiment see the excellent

With the external field applied in the z direction (along $\mathbf{P}_i$), θ is the in-plane spin angle with respect to the applied field. To obtain the true value of the spin angle from the measurement of the (003) magnetic hematite peak in the polarization analysis experiment we first have to correct the data for imperfect polarization of the neutron beam. Figure 5 shows NSF and SF scans of the (003) structural ilmenite and magnetic hematite peaks before the correction. It can be seen that there is a signal

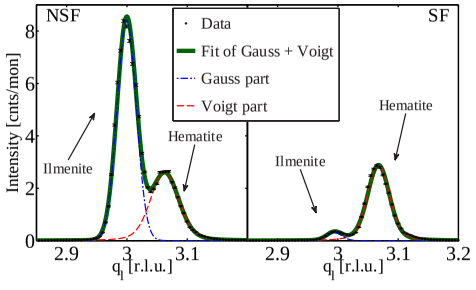

FIG. 5. (Color online) NSF and SF measurement of the (003) structural ilmenite peak and the (003) magnetic hematite peak. This measurement was in an applied field of 0.25 T and at a temperature of 65 K. This data have not been corrected for imperfect polarization as can be seen from the nonzero SF intensity at the position of the structural ilmenite peak.

review by Wildes [30]. The flipping ratio was obtained from measurements of the structural (003) ilmenite peak for each combination of temperature and applied field. These R values were used to obtain the true SF and NSF cross sections from all measurements.

To confirm the AFM to paramagnetic second order phase transition of ilmenite the $(10\bar{\frac{1}{2}})$ magnetic ilmenite peak was measured and the peak amplitude is displayed as a function of temperature in Fig. 7. The data was fitted to the function

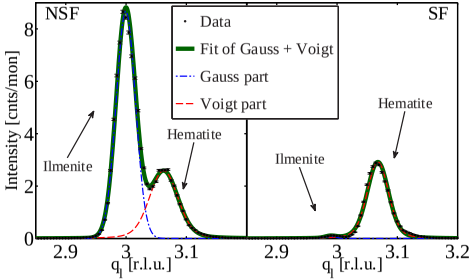

FIG. 6. (Color online) NSF and SF measurement of the (003) structural ilmenite peak and the (003) magnetic hematite peak. This measurement was in an applied field of 0.25 T and at a temperature of 65 K. This data has been corrected for imperfect polarization with a flipping ratio of $R = 43$. The ilmenite reflection is only present in the NSF signal, whereas the hematite peak is present in both the NSF and the SF signal.

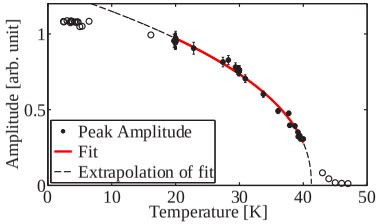

FIG. 7. (Color online) Temperature variation of the $(10\bar{\frac{1}{2}})$ magnetic ilmenite peak, showing the second order phase transition. Both black and hollow points are peak amplitude measurements, however, the fit is to the black points only, since the power law behavior is only valid within approximately this range.

$A = A_0(\frac{T_N - T}{T_N})^{2\beta}$, obtaining $T_N = 41.3 \pm 0.2$ K and $\beta = 0.22 \pm 0.01$. The Néel temperature of 41.3 K is smaller than the 58 K usually quoted for ilmenite, which is due to partial substitution of Mg^{2+} for Fe^{2+} within the ilmenite lattice, as well as minor solid solution of Fe_2O_3.

The intensities of the (003) peaks were obtained through a fit of a Gaussian plus a Voigtian profile to the data (see Fig. 6). The former fits the structural ilmenite peak (bulk material) and the latter fits the magnetic hematite peak (Lorentz broadened peak caused by nanosize effects). For each scan of the (003) peaks the data was corrected in the described way, using the obtained polarization. Figure 8 shows the in-plane spin orientation with higher, θ reaches approximately 56° at the maximum field of 2.5 T, while it only reaches angles of 50°–53° at lower temperatures. At 2, 65, and 288 K measurements in negative fields of increasing magnitude were performed to investigate the hysteresis of the sample. As can be seen in Fig. 8 no significant hysteresis was observed at 288 and 2 K, while there is a small, but distinct hysteresis feature in the 65 K data. In the measurement at 288 K the material is more magnetically soft than at lower temperatures and the magnetization looks to be approaching saturation at approximately 56°. The change in coercivity may be related to increased pinning of 60° and 120° domain walls in hematite at low temperatures. There is no significant change in the spin orientation or the susceptibility between 65 and 35 K, indicating that the hematite moments are not strongly coupled to the ilmenite which orders at 41.3 K.

The data in Fig. 8 are insufficient to conclude whether θ has reached saturation at the applied field of 2.5 T or not. Therefore the intensity of the (101) magnetic hematite peak was measured with unpolarized neutrons at RITA-II in applied fields up to 11 T. The field was applied in the (003) plane, while observing the (101) peak—the same geometry as in the IN12 experiment. The intensity of the (101) peak is proportional to the square of the projection of the magnetic moment perpendicular to the (101) scattering vector and its response to a magnetic field can therefore reveal the saturation field of the hematite moments. The (101) intensity was measured at 2 and 150 K and thus above and below the Néel temperature of ilmenite. The results are displayed in Fig. 9. In the 150 K data the (101) intensity decreases from 0 T to approximately 2.5 T

respect to the applied field calculated from Eq. (3), which is the main result of our investigations. At all temperatures θ is close to 45° in zero field, which is consistent with a nearly random alignment of the hematite magnetic moments within the basal plane. This reflects that the alignment of the hematite moments in zero field due to any remanent magnetization is small and produces a deviation of θ from 45° too small to be measured with any significant precision. When the field is applied θ increases. For the measurements at temperatures of 150 K and and then increases to 11 T. This is consistent with a saturation of the (net) hematite moments followed by a rotation of the

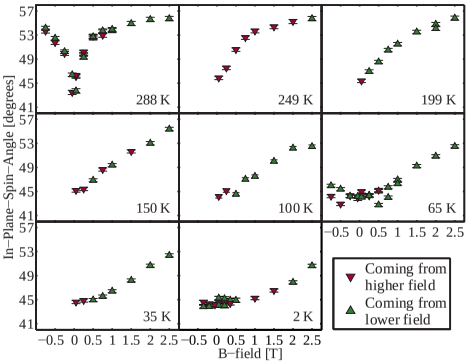

FIG. 8. (Color online) Spin orientation as a function of applied field for different temperatures. The error bars were obtained from Monte Carlo simulations based on the errors on the Voigtian fits.

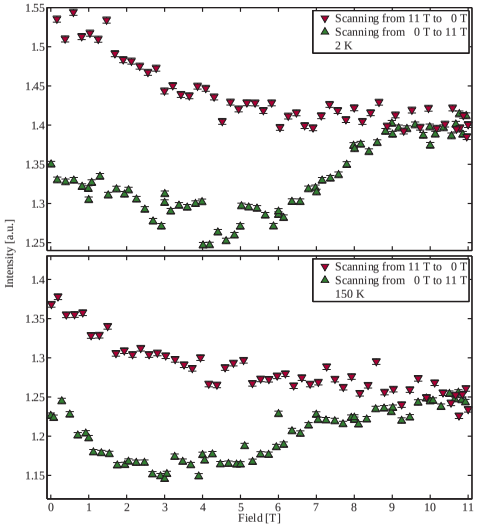

FIG. 9. (Color online) Unpolarized nuclear diffraction measurement at 2 and 150 K of the (101) peak, for applied fields between 0 and 11 T.

AFM sublattices away from antiparallel (AFM susceptibility). When the field is decreased to zero again there is a significant hysteresis. The picture is very much the same in the 2 K data, except that the saturation point is not reached before approximately 5 T. This confirms that for the data in Fig. 8 the value of θ reaches saturation in the measurements at temperatures above 150 K, whereas it is unsaturated at lower temperatures.

IV. DISCUSSION

The strong NRM in natural hemo-ilmenite samples is believed to be caused by uncompensated magnetic moments in contact layers between exsolution lamellae (lamellar magnetism). The magnetization would then be a combination of these lamellar moments and the CAF moments. In a saturating magnetic field the net moment is expected to align parallel to the field (see Fig. 2). It is important to note that the measured angle θ is not the orientation of the net moment, but the average spin orientation. In a model with CAF moments only, the spins would be expected to align nearly perpendicular to the applied field ($\theta = 90^\circ$). At saturation the only deviation from perpendicular will be the insignificant canting angle. For lamellar moments alone the moments would align themselves parallel to the applied field ($\theta = 0^\circ$), whereas a combined lamellar and CAF moment would align at an intermediate angle. The spin angles measured at temperatures above 150 K are saturated at the 2.5 T field, as confirmed by the high-field measurements at RITA-II displayed in Fig. 9. The saturation are uncompensated magnetic layers exactly as described in the lamellar magnetism hypothesis [4,20,23,24] or perhaps randomly placed uncompensated magnetic moments on the interfaces between the two phases like the uncompensated magnetic moment known to produce a significant net magnetization in antiferromagnetic nanoparticles of, e.g., NiO [31,32]. The hematite moments respond to the magnetic field in much the same way above and below the ordering temperature of ilmenite indicating that the effect of any coupling between the lamellar moments and the ilmenite moments is relatively weak in this particular sample.

V. CONCLUSION

We have reported results from a neutron diffraction experiment with uniaxial polarization analysis performed on a natural hemo-ilmenite sample with a fine exsolution structure. Measurements of the $(10\frac{1}{2})$ ilmenite peak confirms that the ilmenite undergoes a second order phase transition from paramagnetic to antiferromagnetic at a Néel temperature of 41.3 K. Measurements of the (003) hematite peak show that the hematite spin angle is close to 45° in zero applied field independent of temperature. This corresponds to a close to random alignment of the hematite moments. When a magnetic field is applied, the in-plane hematite moments rotate away from the field. At temperatures from 150 to 288 K the moment saturates in the maximum applied field of 2.5 T, making an angle of about 56° to the field. At lower temperatures the moment is not saturated in the 2.5 T field. The saturation angle of 56° with respect to the applied field strongly supports the

value of the angle is approximately 56° (Fig. 8). The measured spin angle is an average over all of the hematite spins in the sample and the result is thus consistent with a model with a combination of CAF moments aligning perpendicular to the field and lamellar moments aligning parallel to the field. If all the spins were aligned either perpendicular or parallel to the applied field the 56° would correspond to approximately 62% of the moments being CAF and 38% lamellar moments. The ratio of lamellar to CAF moments will in general depend on the relative surface area of the lamellae and it is likely that the lamellar contribution will be larger in samples with more fine scale lamellae compared to the rather coarse microstructure in the sample investigated here. While this picture is certainly too naive, the 56° angle is evidence that a significant proportion of the spins are aligned parallel to the field, consistent with a model with uncompensated moments in contact layers between lamellae as important for producing the large NRM. We note that our experiment cannot determine whether the magnetic moments here termed lamellar moments hypothesis of lamellar magnetism as part of the explanation for the natural remanent magnetism in natural hemo-ilmenite. Our data rule out a model with either lamellar moments or CAF moments as the sole explanation for the NRM and shows that the magnetization is a sum of contributions of similar size of uncompensated moments in contact layers and CAF moments.

ACKNOWLEDGMENTS

The authors would like to thank the late J. M. Knudsen and the late R. B. Hargraves for inspiring discussions and for suggesting this puzzling nanomagnetism topic for neutron studies. The research leading to these results has received funding from the European Research Council under the European Union's Seventh Framework Programme (FP/2007-2013), ERC Grant Agreement No. 320750, and the Natural Environment Research Council Grant NE/B501339/1. This work was supported by the Danish Agency of Science and Innovation through DANSCATT.

[1] S. A. McEnroe, R. J. Harrison, M. J. Jackson, A. M. Hirt, P. Robinson, F. Langenhorst, F. Heidelbach, T. Kasama, A. Putnis, L. L. Brown, and U. Golla-Schindler, J. Phys.: Conf. Ser. **17**, 154 (2005).

[2] S. A. McEnroe, P. Robinson, and P. T. Panish, Am. Mineral. **86**, 1447 (2001).

[3] S. A. McEnroe, J. R. Skilbrei, P. Robinson, F. Heidelbach, and F. Langenhorst, Geophys. Res. Lett. **31**, L19601 (2004).

[4] P. Robinson, R. J. Harrison, S. A. McEnroe, and R. B. Hargraves, Nature (London) **418**, 517 (2002).

[5] Y. Ishikawa and S.-I. Akimoto, J. Phys. Soc. Jpn. **12**, 1083 (1957).

[6] Y. Ishikawa, J. Phys. Soc. Jpn. **13**, 37 (1958).

[7] W. H. Butler, A. Bandyopadhyay, and R. Srinivasan, J. Appl. Phys. **93**, 7882 (2003).

[8] H. Hojo, K. Fujita, K. Tanaka, and K. Hirao, Appl. Phys. Lett. **89**, 082509 (2006).

[9] T. Fujii, M. Kayano, Y. Takada, M. Nakanishi, and J. Takada, Solid State Ionics **172**, 289 (2004).

[10] H. Kato, M. Yamada, H. Yamauchi, H. Hiroyoshi, H. Takei, and H. Watanabe, J. Phys. Soc. Jpn. **51**, 1769 (1982).

[11] A. H. Morrish, *Canted Antiferromagnetism: Hematite* (World Scientific, Singapore, 1994).

[12] F. J. Morin, Phys. Rev. **78**, 819 (1950).

[13] P. J. Besser, A. H. Morrish, and C. W. Searle, Phys. Rev. **153**, 632 (1967).

[14] R. M. Cornell and U. Schwertmann, *The Iron Oxides* (Wiley, Weinheim, 2003).

[15] D. H. Lindsley, Carnegie Inst. Washington Year Book **64**, 144 (1965).

[16] U. Schärer, E. Wilmart, and J. C. Duchesne, Earth Planet. Sci. Lett. **139**, 335 (1996).

[17] S. A. McEnroe, R. J. Harrison, P. Robinson, and F. Langenhorst, Geophys. J. Int. **151**, 890 (2002).

[18] R. J. Harrison, S. A. McEnroe, P. Robinson, and C. J. Howard, Am. Mineral. **95**, 974 (2010).

[19] P. Robinson, F. Heidelbach, A. M. Hirt, S. A. McEnroe, and L. L. Brown, Geophys. J. Int. **165**, 17 (2006).

[20] P. Robinson, R. J. Harrison, S. A. McEnroe, and R. B. Hargraves, Am. Mineral. **89**, 725 (2004).

[21] S. A. McEnroe, P. Robinson, F. Langenhorst, C. Frandsen, M. P. Terry, and T. Boffa Ballaran, J. Geophys. Res. **112**, B10103 (2007).

[22] P. Robinson, K. Fabian, S. A. McEnroe, and F. Heidelbach, Geophys. J. Int. **192**, 514 (2013).

[23] S. A. McEnroe, B. Carter-Stiglitz, R. J. Harrison, P. Robinson, K. Fabian, and C. McCammon, Nat. Nanotechnol. **2**, 631 (2007).

[24] K. Fabian, S. A. McEnroe, P. Robinson, and V. P. Shcherbakov, Earth Planet. Sci. Lett. **268**, 339 (2008).

[25] J. C. Duchesne, Mineral. Deposita **34**, 182 (1999).

[26] P. Böni and P. Keller, PSI Proc. **2**, 35 (1996).

[27] E. Brok, Master thesis, University of Copenhagen, 2009.

[28] K. Lefmann, C. Niedermayer, A. B. Abrahamsen, C. Bahl, N. Christensen, H. Jacobsen, T. Larsen, P. Häfliger, U. Filges, and H. Rønnow, Phys. B: Condens. Matter **385-386**, 1083 (2006).

[29] R. Moon, T. Riste, and W. Koehler, Phys. Rev. **181**, 920 (1969).

[30] A. R. Wildes, Neutron News **17**, 17 (2006).

[31] J. T. Richardson, D. I. Yiagas, B. Turk, K. Forster, and M. V. Twigg, J. Appl. Phys. **70**, 6977 (1991).

[32] C. R. H. Bahl, M. F. Hansen, T. Pedersen, S. Saadi, K. H. Nielsen, B. Lebech, and S. Mørup, J. Phys.: Condens. Matter **18**, 4161 (2006).

Appendix B

Simulation of a suite of generic long-pulse neutron instruments to optimize the time structure of the European Spallation Source

This article describes the work behind a study of the possible neutron source time structures of the European Spallation Source (ESS) and their impact on the ESS instrument suite. This work would be an important part of the decision process for the final time structure. The work was carried out by the Copenhagen Simulation Task Force Team [23].

My contribution to this article was to simulate a thermal powder diffractometer using Wavelength Frame Multiplication. In order to investigate the impact of the source

time structure (frequency and pulse length) on the instrument performance of a powder diffractometer, the effect of the instrument's elliptical guide shape, the wavelength band, the moderator hot-spot, and the chopper set-up was investigated and optimised for each source setting. For this study we simulated 20 settings. More on this can be found in Appendix C. (Note that each inserted article page is spread across two pages in this text.)

REVIEW OF SCIENTIFIC INSTRUMENTS **84**, 055106 (2013)

Simulation of a suite of generic long-pulse neutron instruments to optimize the time structure of the European Spallation Source

Kim Lefmann,[1,2] Kaspar H. Klenø,[1,2] Jonas Okkels Birk,[1,2,3] Britt R. Hansen,[4,5] Sonja L. Holm,[1,2] Erik Knudsen,[4,5] Klaus Lieutenant,[6,7,8] Lars von Moos,[9,5,10] Morten Sales,[1,2] Peter K. Willendrup,[4,5] and Ken H. Andersen[11]

[1]*Nanoscience and eScience Centers, Niels Bohr Institute, University of Copenhagen, Universitetsparken 5, 2100 Copenhagen Ø, Denmark*
[2]*Danish Workpackage for the ESS Design Update Phase, Universitetsparken 5, 2100 Copenhagen Ø, Denmark*
[3]*Laboratory for Quantum Magnetism, École Polytecnique Fédérale de Lausanne (EPFL), 1015 Lausanne, Switzerland*
[4]*Institute of Physics, Technical University of Denmark, 2800 Lyngby, Denmark*
[5]*Danish Workpackage for the ESS Design Update Phase, 2800 Lyngby, Denmark*
[6]*Institute for Energy Technology, Instituttveien 18, 2007 Kjeller, Norway*
[7]*Helmholtz Center for Energy and Materials, Hahn-Meitner Platz, 14109 Berlin, Germany*
[8]*German Work Package for the ESS Design Update, Hahn-Meitner Platz, 14109 Berlin, Germany*
[9]*Department of Energy Conversion and Storage, Technical University of Denmark, 4000 Roskilde, Denmark*
[10]*Institute for Energy Conversion, Technical University of Denmark, 4000 Roskilde, Denmark*
[11]*European Spallation Source ESS AB, 22100 Lund, Sweden*

(Received 18 January 2013; accepted 16 April 2013; published online 7 May 2013)

We here describe the result of simulations of 15 generic neutron instruments for the long-pulsed European Spallation Source. All instruments have been simulated for 20 different settings of the source time structure, corresponding to pulse lengths between 1 ms and 2 ms; and repetition frequencies between 10 Hz and 25 Hz. The relative change in performance with time structure is given for each instrument, and an unweighted average is calculated. The performance of the instrument suite is proportional to (a) the peak flux and (b) the duty cycle to a power of approximately 0.3. This information is an important input to determining the best accelerator parameters. In addition, we find that in our simple guide systems, most neutrons reaching the sample originate from the central 3–5 cm of the moderator. This result can be used as an input in later optimization of the moderator design. We discuss the relevance and validity of defining a single figure-of-merit for a full facility

and compare with evaluations of the individual instrument classes. © *2013 AIP Publishing LLC.*
[http://dx.doi.org/10.1063/1.4803167]

I. INTRODUCTION

The European Spallation Source (ESS) is designed to be a long-pulsed spallation neutron source – the first of its kind.[1,2] This opens new territory, including the challenges to design instruments that perform well for a long-pulsed source, to design the optimal moderator for these instruments, and to choose the pulsing time structure that matches these choices. Obviously, these optimizations are coupled, since, e.g., the instrument design depends upon the pulse length and the optimal moderator design depends on both desired pulse length and on the instrument geometries.

In this article, we are concerned with only one part of this optimization problem: the selection of the source time structure, i.e., its pulse length (τ) and repetition time (T). The original 2002 design was fixed at $\tau = 2$ ms, and $T = 60$ ms ($f = 16\frac{2}{3}$ Hz),[3] and we have therefore investigated time structures in the neighbourhood of these initial parameters.

In order to perform the time-structure optimization, we have selected a suite of generic instruments, covering a broad range of scientific utilizations. These instruments have then undergone a rough design and optimization for each setting of (T, τ), and the relative merits of the instruments at the different time structures have been compiled and compared.

The simulated instrument suite should not be seen as a draft day-one suite, neither should the individual instruments be seen as being close to their final design. Much design work and careful selection of an initial instrument suite is presently in progress. The present work is merely the first step in a long process.

Below, we present our generic neutron long-pulse instrument suite, the optimization procedure, and the obtained overall results. The simulation results of the 15 individual instruments are available online[4] and are or will be published individually in more detailed articles.[5–12]

As a result of this and other studies of the ESS time structure, covering its impact on the performance, reliability, construction cost, and operation of the facility, the time structure has now been fixed at $\tau = 2.86$ ms and $T = 71$ ms ($f = 14$ Hz). The results presented in this paper were an important input to this decision.

II. THE GENERIC INSTRUMENT SUITE

The instrument suite we discuss here was initiated by the Scientific Advisory Group (SAG) for ESS-Scandinavia, in September 2009. This list was expanded by the slightly different "straw-man-list" of instruments, decided upon by the

TABLE I. Properties of 15 generic ESS instruments, suggested by the ESS-S SAG and the ESS SAC. L_1 denotes the length of the instrument for a pulse length of $\tau = 1$ ms, while L_2 is the instrument length for $\tau = 2$ ms, and β is the "Frascati exponent," defined by (1).

Instrument	L_1 (m)	L_2 (m)	β
Cold chopper spect.	60	100	0
Therm. chopper spect.	100	100	0
Cold triple axis	40	40	0
Thermal triple axis	40	40	0
TOF triple axis	60	100	0
Backscatter spectrometer	151	302	0
Spin echo spectrometer	30	30	2.5
Short SANS (bio-)	12 + 1–4		2.5
Medium SANS	18 + 1–10		2.5
Long SANS (materials-)	28 + 2–20		2.5
Horizontal reflectometer	52	52	4
Vertical reflectometer	52	52	4
Cold powder diffract.	88	176	0
Thermal powder diffract.	102	102	0
Single crystal diffract.	31	42	0

Scientific Advisory Council for the ESS (SAC) in June 2010. Our starting list was found as a join of these two instrument suites, and is shown in Table I. It should be noted that due to time constraints, neither a tomography instrument, a protein diffractometer, nor a wide-angle spin-echo instrument have been included in these simulations, even though these classes of instruments were present in the straw-man suite. For an artists view on the present version of the straw-man suite, see contains the chosen values of β. Here, a value of zero indicates that all neutrons are considered equally valuable, while a positive value of β gives preference to long-wavelength neutrons.

III. DESIGN AND OPTIMIZATION OF INSTRUMENTS

Over the last decade or more, a number of authors have addressed the issue of long-pulse instrumentation.[14–17] The instrument concepts and designs simulated here are in general adapted from the earlier work, except that we have adjusted the instrument lengths as described below and listed in Table I. Most instruments on this list are typical time-of-flight instruments, except the reactor-type triple-axis instruments. One untraditional instrument type, labeled "TOF Triple Axis" has been included in the list. This is a hybrid (or inverted-geometry) spectrometer[11] with a time-of-flight front-end and a triple-axis-like crystal analyzer back-end.

A. Instrument length and resolution

To qualify the discussion, let us first recall the equation for the neutron time-of-flight, t,

$$t = \alpha \lambda L, \tag{2}$$

where L is the flight length and $\alpha = m_n/h \approx 252.7\,\mu$s/(m Å). The relative uncertainty of the neutron wavelength can then be expressed by the uncertainty in flight time by

Fig. 1.

In the optimizations, we have taken into account that neutrons of different wavelengths may not be equally useful for the individual instruments. In particular, spin-echo spectrometers, reflectometers, and small-angle diffractometers strongly prefer long wavelength neutrons. To account for this fact in a simplified way, we parametrize the relative "value," V, of each neutron by a simple expression

$$V(\lambda) = \lambda^{\beta}. \tag{1}$$

The values of β for different instrument types were selected by an expert meeting in Frascati, August 2009,[13] and Table I

$$\frac{\delta\lambda}{\lambda} = \frac{\delta t}{t} = \frac{\delta t}{\alpha\lambda L}. \tag{3}$$

For long-pulse instruments, δt is either given approximately by the pulse length, τ, (at a long pulsed source, the exponentially decaying tail of the pulse can to first order be neglected compared to τ), or by the opening time of a pulse-defining chopper, as described below. In the latter case, L will be the flight length from the pulse-defining chopper to the detector, in the former it will denote the full instrument length to the detector (for chopper spectrometers, see later).

In analogy, the useful wavelength band, $\Delta\lambda$, of neutrons which can reach the detector without creating frame overlap

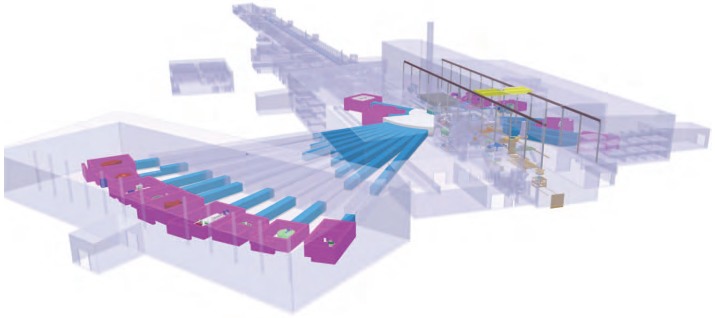

FIG. 1. Artists view of the ESS target/instrument buildings seen obliquely from above. Note that the long instruments are placed in a hall (foreground left) which is separated from the main target building (right). The accelerator is seen stretching into the background.

is given by

$$\Delta\lambda = \frac{\Delta t}{\alpha L}, \tag{4}$$

where for instruments using the full pulse, $\Delta t = T - \delta t \approx T$.

A number of the simulated instruments cannot directly utilize the full pulse length, τ, since this would result in a too bad resolution (too large $\delta\lambda/\lambda$). Therefore, pulse shaping must be performed at a fast pulse-defining chopper, close to the source. In this work, the distance between source and chopper is set to the smallest realistic value given by the biological shielding of the moderator: $L_{\mathrm{pc}} = 6$ m.) A pulse-defining chopper at the distance L_{pc} effectively selects a wavelength band, given by $\Delta\lambda = \tau/(\alpha L_{\mathrm{pc}})$. To let this wavelength band fill the whole time frame, T, at the detector, the instrument must be very long: $L = L_{\mathrm{pc}}(1 + T/\tau)$, which for the parameters investigated in this work lies between 126 m and 606 m, since the inverse duty cycle, T/τ, lies in the range 20–100.

B. Wavelength frame multiplication and repetition rate multiplication

At some instruments with pulse-defining choppers, we have used an alternative scheme to having very long instruments: A number of closely spaced shorter pulses is produced at the pulse-defining chopper, which are then kept separated

D. The guide systems

For the short guide systems (below 60 m), we have everywhere used guides with constant cross section, where fast-neutron background from direct line-of-sight to the moderators is avoided by inserting a kink or curved section. At the reflectometers, we have used elliptical focusing in the direction perpendicular to the sample surface, combined with a kink in the other direction.

For instruments of 60 m and longer, and for the 40 m triple-axis instruments, we have employed elliptical guides for beam transport, since recent experiments and simulations have shown this design to be strongly superior over traditional curved guides.[6,24]

For the values of guide reflectivities, we have everywhere used recent information from one supplier.[25] In general, we use $m = 3$ along the main length of all guides, and $m = 6$ in the beginning and end of elliptical guides.

Guides have everywhere been assumed to consist of straight sections, with perfect alignment and zero waviness. The effect of waviness and misalignment of (in particular) long elliptical guides is a topic of future simulations.[26] A similar work was carried out earlier for straight guide geometries.[27]

In the optimizations, we have assumed 40 cm as the maximal guide width for the longest guides, relying on information that guides of this width and matching slow frame-overlap choppers can be produced.[25,28] Should it be necessary to place stricter limits on the guide width this will affect the

by a number of sub-frame-overlap choppers. This has been denoted "Wavelength Frame Multiplication" (WFM), as first presented by the group of Mezei.[18,19] In the present simulations, the WFM method is used at the thermal powder diffractometer and the thermal chopper spectrometer.

The cold chopper spectrometer uses a similar technique, which bears the name "Repetition Rate Multiplication" (RRM). Here, the full pulse length is used, but a monochromating chopper close to the sample produces up to 15 different monochromatic pulses for each moderator pulse,[14,20] as simulated in Ref. 5. Recently, this technique has been experimentally proven feasible at NEAT, HZB[21] and 4SEASONS, J-PARC.[22] In the present simulations, also the thermal chopper spectrometer employs RRM (in addition to using WFM).

C. The source

Lacking precise information about the source power and moderator performance for the different time structures, we have initially considered the two following scenarios.

1. The source has a constant time-average neutron flux.
2. The accelerator is limited by a maximum beam current; i.e., the source peak flux is constant.

These two scenarios differ only by a τ/T scaling of the source flux, whence we were able to use the same set of simulations/optimizations. As a reference point at the baseline settings, we use the characteristics of a 12×12 cm^2 moderator with uniform flux distribution, as given in Ref. 23.

absolute flux values at some instruments,[26] but not the relative comparisons relevant for the present work. This statement is valid for most other design parameters.

For the long guides, no attempt has been made to avoid line-of-sight. The key issue is that bending of the guides, as known from traditional guide systems, would disturb the elliptical focusing properties,[26] whence a solution to this issue is more involved and was postponed to later studies.[29,34]

An additional possibility to reduce the fast-neutron background would be to insert either a crystal filter or a heavy "straight-beam-block" in the middle of the guide, probably early in the guide.[30] Another possibility for guide design is the combination parabolic-straight-parabolic, where the straight section can be curved. This combination transmits almost as well as an elliptical guide.[24]

E. Optimization of instruments by simulation

All present simulations were performed using the Monte Carlo ray-tracing package McStas v. 1.12,[31] where the instrument designs were typically performed on individual computers, while the final optimization and data taking was performed on the computer cluster of the ESS Data-Management Center in Copenhagen. Typical runs used between 10^8 and 10^{11} neutron rays, depending on the type of instrument.

Instruments were first simulated at the baseline time structure settings of $\tau = 2$ ms and $T = 60$ ms. The instrument length and chopper settings were adjusted as to obtain a predetermined instrumental resolution, while remaining above a certain length limit, relevant for the SANS and spin-echo

instruments. Subsequently, the guide system of each instrument was optimized using a Figure-of-Merit (FoM) found from the time average flux, $\Psi(\lambda)$, on the sample position in the useful wavelength band, $[\lambda_{\min}, \lambda_{\max}]$ weighted by $V(\lambda)$,

$$\mathrm{FoM} = \int_{\lambda_{\min}}^{\lambda_{\max}} \Psi(\lambda) V(\lambda) d\lambda. \quad (5)$$

Subsequently, the design of each of the 15 instruments was modified and optimized for each of 20 different time structure settings, in principle 300 optimizations and subsequent simulated data. In order to produce comparable simulations, all optimizations for a given instrument were restricted to have certain resolution characteristics. For spectrometers, this was given as $\delta\lambda/\lambda$ at the sample position for a certain value of λ. For diffractometers, this was given as a fixed $\delta\lambda/\lambda$ at the detector for a limited divergence matching this value, to obtain a certain low linewidth in the measured lattice spacing, $\delta d/d$, at a given scattering angle. For a few instrument types (spin-echo spectrometer and SANS), the worst resolution was in all cases deemed "sufficient," so these instruments were not restricted by resolution requirements and were thus simulated at their constant (minimum) lengths.

Since it has been proposed to place triple-axis spectrometers at the long-pulsed ESS, we have included a cold and a thermal instrument in these comparisons. For a triple-axis spectrometer at a pulsed source, the time structure is useful only for filtering of background and higher order harmonics. Hence, the instrument has identical FoM for all time structure

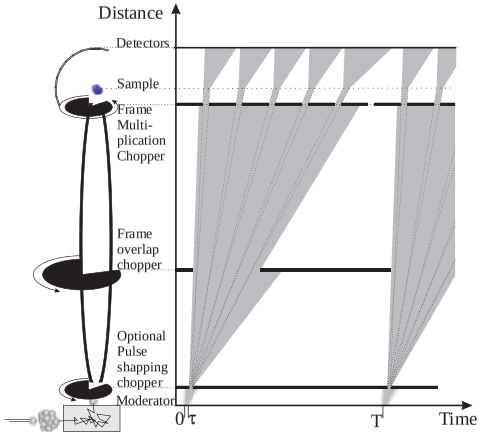

FIG. 2. (left) Sketch of the main elements of the cold chopper spectrometer. Picture is not to scale. (right) Time-of-flight diagram illustrating the selection of neutron pulses by choppers, with the spectrometer running in RRM mode with $N = 5$.

as presented earlier. This mode allows for each source pulse 9 monochromatic pulses on the sample, with a wavelength difference between neighbouring pulses of 0.25 Å, and 6 ms between pulses. In this way, the instrument reaches a combined

settings, and we needed to simulate only one time structure for each of the two triple-axis spectrometers.

IV. RESULTS OF INSTRUMENT OPTIMIZATIONS

We now present the results of our optimizations over the time structure range, as described above. To exemplify, we begin with the results for two individual instruments, before describing the combined results of the full instrument suite. Finally, we discuss the validity of our FoM approach.

A. Simulation example 1: Cold chopper spectrometer

Let us first consider the simulation of the cold-neutron chopper spectrometer, with a design similar to IN5 at ILL. In this present (simple) version of this instrument, the monochromatization is performed by the (full) length of the pulse, in combination with the opening time of fast choppers just before the sample, as illustrated in Fig. 2. The instrument length is determined by the pulse length, to fulfill a constant $\delta\lambda/\lambda = 1.6\%$ at 5 Å wavelength. At the baseline time structure settings, the distance between the source and the fast chopper is $L = 100$ m, and the useful band is 2.2 Å wide (here chosen to be 3.9–6.1 Å). This is described in detail in Ref. 5, where, however, a more simple guide system was used. Our results can thus be seen as an update of the previous publication.

The present cold chopper spectrometer uses an elliptical guide with quadratic cross section, which is 27.3 cm at its widest place. The guide focuses to the sample, which is defined to be 2×2 cm^2. The instrument uses the RRM scheme, monochromatic flux of 1.6×10^8 n/s/cm^2 for the wavelength band mentioned above, centered at 5 Å.

A shorter source pulse will allow for a shorter instrument; for pulses of 1.5 ms, 1.25 ms, and 1.0 ms, the instrument length becomes 80 m, 70 m, and 60 m, respectively. (The finite opening time of the monochromating choppers has the consequence that the 1.0 ms instrument is less than a factor two shorter than the 2.0 ms instrument.) A shorter instrument gives rise to a larger bandwidth and thus more neutrons on the sample (for constant time-average flux). For example, when going from 2 ms to 1 ms pulse length, the increase in FoM is more than 50%, as seen in Table II. A rather similar gain is found from lowering the source frequency from $16\frac{2}{3}$ Hz to 10 Hz, also due to the larger useful bandwidth.

Due to the point-to-point-like focusing of an elliptical guide, most neutrons at the sample originate from the

TABLE II. Relative Figure-of-Merit (FoM) values for the simulations of the IN5-like cold chopper spectrometer at ESS, under the assumption of constant time-average flux. Simulations are performed for 20 different settings of the time structure, (T, τ). The RRM scheme is parametrized by N, which indicates the number of possible monochromatic pulses at the sample per source pulse.

T (ms)	τ (ms)	1.0	1.25	1.5	2.0	N
100 (10 Hz)		2.39	2.24	2.05	1.67	15
80 (12.5 Hz)		2.08	1.83	1.59	1.26	11
60 (16.67 Hz)		1.72	1.48	1.29	1.00	9
50 (20 Hz)		1.35	1.17	0.98	0.76	7
40 (25 Hz)		0.91	0.81	0.68	0.56	5

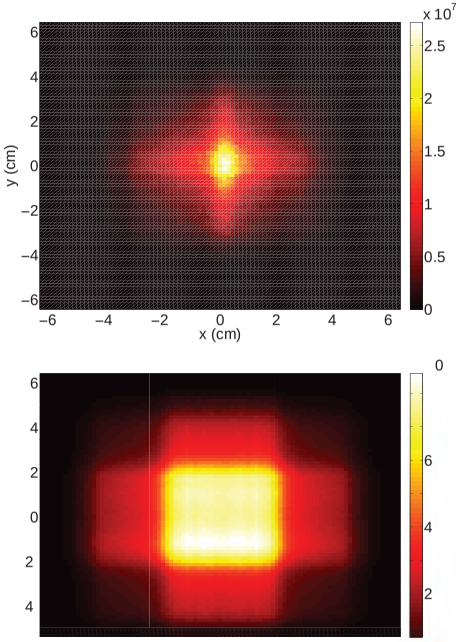

FIG. 3. Simulated plots of the moderator surface showing the number of neutrons which reach the sample at the IN5-like chopper spectrometer. Top panel shows the situation with a 60 m guide ($\tau = 1$ ms), while bottom panel shows the results for a 100 m guide ($\tau = 2$ ms).

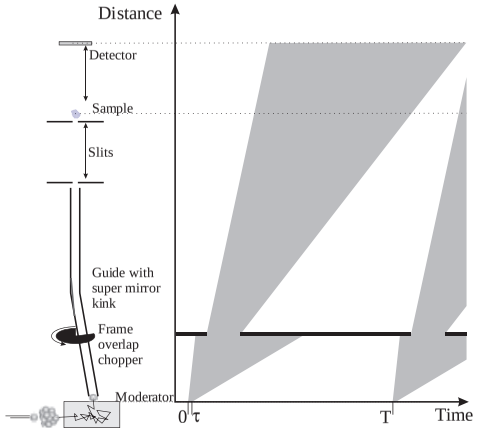

FIG. 4. (left) Sketch of the main elements of the long SANS instrument. Details are not to scale. (right) Time-of-flight diagram illustrating the selection of wavelength band by choppers, with the spectrometer running in the (20 + 20) m setting.

length uncertainty is determined by the full pulse length, since the incoming wavelength is determined by the measured time-of-flight in the detector (assuming elastic scattering at the sample).

innermost 4×4 cm^2 of the moderator surface, as shown in Fig. 3. Therefore, it would be beneficial if neutrons were emitted preferentially from the center of the moderator. A simulated hot spot with a factor 2.0 intensity gain over a circle of diameter $d = 3$ cm produces a gain in neutron flux at the sample of 30%.

Taken at face value, the flux number obtained at the base time structure settings represents an impressive factor 200 gain over IN5. However, care should be taken when comparing these numbers. First, the full gain is possible only if neutrons from all monochromatic pulses are equally useful to the actual experiment. Second, much of the flux increase comes from an increased divergence of neutrons in the elliptical guide system (compared to the straight/curved guide at IN5), and this part of the gain would be of value only to particular experiment types. Hence, the mentioned gain is for this instrument a best case scenario, where a worst case scenario (collimating down to IN5 divergence and using only one RRM frame) would lead to a gain factor of "just" 5.

B. Simulation example 2: Long SANS instrument

We now consider the longest of the three simulated cold-neutron small-angle scattering instruments. In analogy with the cold chopper spectrometer described above, the wavelength band selection is found in Fig. 4.

The length of the instrument is in practice determined by the 20 m long double-pinhole collimator section, combined with an initial 8 m of guide, which includes a kink to avoid direct line-of-sight. The source-sample distance is thus always 28 m, while the sample-detector distance can vary between 2 m and 20 m. The relevant time-of-flight length, L, thus varies between 30 m and 48 m. At these lengths, the wavelength uncertainty at the SANS instrument at $\lambda = 5$ Å and $\tau = 2$ ms is of the order $\delta\lambda/\lambda \approx 3\%$–$5\%$, which is almost always "too good," since the double-pinhole collimation of $d_1 = 10.5$ mm and $d_2 = 7.0$ mm has the dominating contribution to the q-resolution.

The bandwidth of the instrument is rather large, of the order 8 Å at the shortest detector setting. In combination with the large angular range covered at the detector, this allows a large q-range detected in the same setting. A sketch of the long SANS instrument and the corresponding wavelength

In our optimizations, we have employed three settings of the collimation length and the sample-detector distance: $(2 + 2)$ m, $(10 + 10)$ m, and $(20 + 20)$ m. The results presented are an average of the three results, each normalized by the result at the baseline setting. For the baseline setting, the instrument reaches neutron fluxes of 1.8×10^8 n/s/cm^2, 9.0×10^5 n/s/cm^2, and 9.7×10^3 n/s/cm^2 for the three choices of distance, respectively, and the wavelength band centered around 10 Å.

A shorter source pulse will give better wavelength resolution, but the instrument cannot be shortened due to the kink and the collimation section. Therefore, this gives no gain in

TABLE III. Relative Figure-of-Merit (FoM) values for the simulations of the long SANS instrument at ESS under the assumption of constant time-average flux. Simulations are performed for 20 different settings of the time structure, (T, τ).

T (ms)	τ (ms)	1.0	1.25	1.5	2.0
100 (10 Hz)		1.69	1.69	1.69	1.69
80 (12.5 Hz)		1.34	1.34	1.34	1.34
60 (16.67 Hz)		1.00	1.00	1.00	1.00
50 (20 Hz)		0.83	0.83	0.83	0.83
40 (25 Hz)		0.67	0.67	0.67	0.67

bandwidth (or integrated flux), but a small improvement in q-resolution. If, on the other hand, the source frequency is lowered, e.g., to 10 Hz, at constant time-average flux, the instrument will benefit from an increase in useful bandwidth and hence the FoM will increase. All FoM data are displayed in Table III.

At the longest collimation length, all neutrons at the sample originate from a circle of $d \approx 2.5$ cm at the center of the moderator surface. This effect is less pronounced at the shorter collimation lengths. This is illustrated in Fig. 5. On average, a simulated hot spot with a factor 2.0 intensity gain over a circle of diameter $d = 3$ cm produces a gain in neutron flux at the sample of 73%.

TABLE IV. Average relative Figure-of-Merit for the generic ESS instrument suite at different time structures, under the assumption of constant time-average flux.

T (ms)	τ (ms)	1.0	1.25	1.5	2.0
100 (10 Hz)		2.07	1.81	1.67	1.37
80 (12.5 Hz)		1.89	1.66	1.55	1.19
60 (16.67 Hz)		1.62	1.42	1.24	1.00
50 (20 Hz)		1.53	1.27	1.09	0.88
40 (25 Hz)		1.20	1.05	0.90	0.73

C. Optimization of the full instrument suite

After the optimization procedures, we record the resulting values of wavelength, bandwidth, flux at sample position, and FoM for each instrument and time structure setting. The results of the individual simulations are in general similar to the simulation results of the chopper spectrometer and the small-angle instrument shown above. (Results can be found from Ref. 4.) The obtained values of FoM have been normalized to the baseline setting of $T = 60$ ms and $\tau = 2$ ms.

For constant time-average flux, almost all instruments perform better towards the upper left-hand corner of the performance matrix. This is as expected, since (i) a longer T will allow for a larger useful wavelength band, $\Delta\lambda$, and

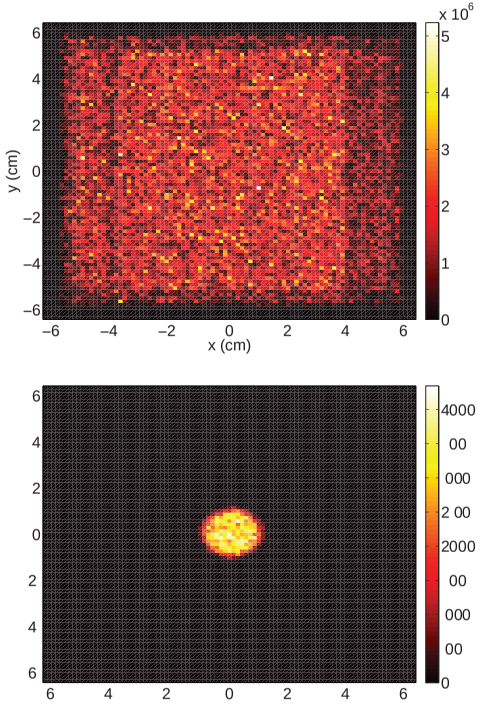

FIG. 5. Simulated plots of the moderator surface showing the number of neutrons which reach the sample for the 20 m SANS instrument. The results are valid for any time structure. (top) data for 2 m collimator-detector setting; (bottom) data for 20 m collimator-detector setting.

(ii) a smaller τ will either (iia) allow L to be smaller, giving an increased $\Delta\lambda$, or (iib) allow a higher fraction of the total flux through the pulse-defining choppers.

In contrast, for the constant-peak-flux scenario, most instruments perform better towards the lower right corner of the performance matrix. This is most simply explained by the fact that here, more neutrons are produced in total, overcompensating the advantages of short pulses and low frequencies mentioned above.

To perform a global comparison of the different time structure settings, we use the relative instrument performances for each instrument. A simple arithmetic mean value has been used, since no decision on the relative importance of instruments has been taken. The results for the average performances are listed in Tables IV and V for the constant-time-average-flux and constant-peak-flux scenarios, respectively.

We see that the effect of shortening the pulse from 2.0 ms to 1.0 ms is typically around 60% increase at constant time-average flux – or around 20% decrease at constant peak flux. Likewise, the effect of going from 20 Hz to 10 Hz is

TABLE V. Average relative Figure-of-Merit for the generic ESS instrument suite at different time structures, under the assumption of constant peak flux.

T (ms)	τ (ms)	1.0	1.25	1.5	2.0
100 (10 Hz)		0.62	0.68	0.75	0.82
80 (12.5 Hz)		0.71	0.78	0.87	0.89
60 (16.67 Hz)		0.81	0.89	0.93	1.00
50 (20 Hz)		0.92	0.95	0.98	1.05
40 (25 Hz)		0.90	0.98	1.01	1.09

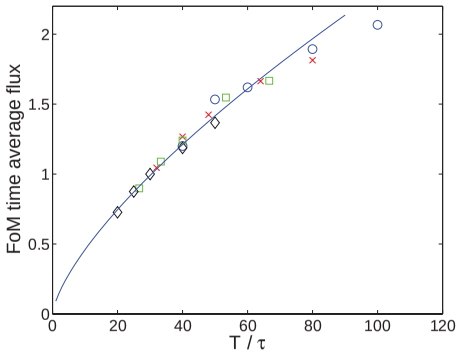

FIG. 6. Average Figure-of-Merit for the generic ESS instrument suite at different time structures, plotted as a function of the inverse source duty cycle, under the assumption of constant time-average flux. Diamonds, squares, crosses, and circles represent pulse lengths of 2.0, 1.5, 1.25, and 1.0 ms, respectively. The solid line is a fit to the power law (6), as explained in the text.

around a 50% increase at constant time-average flux – or around 30% decrease at constant peak flux.

The data for constant time-average flux is shown as a function of the inverse source duty cycle, T/τ, in Figure 6. It is seen that, except for the very smallest duty cycles, the data fall almost on a common curve, which can be approximately described by

into one single number, the FoM, and to express its variation by essentially one parameter, the duty ratio τ/T, as illustrated in Figure 6. This assumption shares one problem with most numerical optimization work: Details that cannot be compressed into the FoM are easily overlooked. For this reason, we will look more into some of these details. To simplify the argument, we will consider the effect on the instrument performance under the condition that the duty cycle τ/T is unchanged. The effect of varying the time structure under this boundary condition depends rather sensitively on the type of instrument.

- SANS, reflectometry and spin-echo instruments will benefit from the increased wavelength range which a longer repetition period will give them. Their performance will not suffer significantly from the degraded wavelength resolution, which an associated increase in pulse length would give. Any increase in bandwidth translates directly into improved performance.
- Crystal-monochromator instruments, such as triple-axis spectrometers, do not make much use of the source time structure at all. In these cases, only the time-average flux counts. The time structure has little or no effect.
- Chopper spectrometers, or other instruments that may employ RRM, have a weak preference for shorter repetition periods. These instruments use the RRM to compensate for the fact that their preferred repetition frequency is higher than the source frequency. Increas-

$$\mathrm{FoM} \approx \Psi_{\mathrm{peak}} \left(\frac{\tau}{T}\right)^{\alpha} = \Psi_{\mathrm{peak}}^{1-\alpha} \Psi_{\mathrm{time\,av}}^{\alpha} = \Psi_{\mathrm{time\,av}} \left(\frac{T}{\tau}\right)^{1-\alpha}, \tag{6}$$

with $\alpha = 0.30$. This value confirms the trivial result that the long-pulse source of the ESS is intermediate in nature between a short-pulse source and a continuous source. Instruments at short-pulse sources aim to be optimized to benefit from the peak flux, while instruments at steady-state sources are optimized to benefit from the time-average flux. The exact value of the exponent will clearly depend on the chosen instrument suite, but it is interesting to note first that the instrument performance scales more closely with the peak flux than with the time-average flux. Second, Eq. (6) predicts that the global instrument performance depends only on the time-average flux and duty cycle. If both are kept constant, e.g., by changing T and τ simultaneously, the instrument performance should be independent of the time structure.

Our results can be seen as a natural continuation of the discussion on the merits of long-pulse sources, initiated in Ref. 14. While the previous work has used an analytical approach to address the usefulness of long neutron pulses, our results serve to quantify this usefulness, including important features like moderator spectrum and instrument-specific details across the instrument suite.

D. Considerations beyond a simple figure-of-merit

The analysis above is based on the assumption that it is possible to reduce the full scientific usefulness of a facility to a single figure-of-merit. This is clearly not the case, and there are several important considerations that are not included in the above analysis.

- Instruments that rely on resonance spin echo (RSE) techniques, such as neutron spin echo spectrometers, have a preference for longer repetition periods. This is because the RSE technique is inherently a time-of-flight technique, and the flight path is limited by the repetition period. Increasing the source frequency reduces the need for RRM and makes their data-collection strategy more similar to existing instruments and simplifies the data analysis.
- Very high-resolution instruments, such as backscattering spectrometers and high-resolution diffraction also have a preference for shorter repetition periods. These instruments cut out only a small fraction of the pulse length to achieve the desired resolution and do not benefit significantly from the increased wavelength range offered by an increase in repetition period.

Overall, it seems clear that an increase in pulse length will translate into an increase in the average length of the instruments, which will, in turn, result in increased costs for guides and shielding along the guides. On the other hand, with modern ballistic-type guides, the transport of neutrons represents no essential problem,[24] while the instrument space becomes less restricted at the same time as the general background level decreases. In addition, certain combinations of T and τ may result in instruments with lengths which allow them to be grouped together in common instrument halls, rather than requiring separate buildings. In such a scenario, the cost savings associated with the reduction in the number of instrument buildings could cancel out the cost increase of the longer guides, as well as providing other benefits in terms of upgradeability and flexibility.

E. Optimizing the moderator parameters

The design and simulation of the target/moderator is much more computationally demanding than that of the

instruments. Hence, one aim of the instrument simulations has been to assist the moderator optimizations towards an improved functionality of the full ESS. We here describe the results obtained in this direction.

Often, the figure-of-merit in moderator optimizations is the number of neutrons produced, possibly in a given wavelength interval and for a given moderator size. However, the moderator simulations produce more detailed information than this. The result of each simulation is given as a history of neutron events, each event having 6 parameters: position at moderator surface ($\mathbf{r}$), time of emittance (t), wavelength (λ), and moderator emission angle ($\boldsymbol{\eta}$). By means of instrument simulations it was found possible to represent the transmission probability of a neutron from moderator surface to sample as

$$T(\mathbf{r}, \lambda) \approx T_r(\mathbf{r}) T_\lambda(\lambda). \tag{7}$$

Here, the dependence on divergence has been integrated out, since the moderator flux (even with complex geometries) is expected to vary insignificantly over the rather small solid angle of the guide entry, Furthermore, we have neglected the emission time, which corresponds to ignoring the tails from the moderators. For a total target/moderator optimization, the figure-of-merit to optimize is thus for each of the moderators (e.g., a cold and a thermal),

$$\mathrm{FoM}_{\mathrm{mod}} = \sum_j W_j \int N(\mathbf{r}, \lambda, t, \boldsymbol{\eta}) V_j(\lambda)$$

V. CONCLUSION

We have performed a series of systematic ray-tracing simulations of the performance of a generic instrument suite for the ESS. These simulations were carried out for a large number of time structure settings, for constant, typical instrument resolutions. The performance parameters were found to increase with increasing peak flux, as well as with increasing time-average flux, while varying only weakly with the details of the time structure.

The variation with time-average and peak flux can be expressed as $\mathrm{FoM} \propto \Psi_{\mathrm{peak}}(\tau/T)^{\alpha}$, with $\alpha = 0.30$. If both the peak flux and the duty cycle are kept constant, the average instrument performance is largely independent of pulse-length or frequency, within the frequency range of the current study.

Since most instruments use tight collimations or (elliptical) focusing guides, most neutrons hitting the sample stem from a central part of the moderator of a diameter 3–5 cm. We suggest to use this knowledge for the optimization of the moderator design, in particular by considering “hot spots” at the moderator. However, this can be finalized only when the guide systems of the instruments are designed.

A. Implications for design of long-pulsed sources, e.g., ESS

As part of the study which resulted in the decision to fix the time structure of the ESS to $\tau = 2.86$ ms and $T = 71$ ms

$$\times T_{j,r}(\mathbf{r})T_{j,\lambda}(\lambda)d^2\mathbf{r}d\lambda d^2\boldsymbol{\eta}dt, \qquad (8)$$

where the summation label, j, represents the instruments at the moderator, W_j is a normalization and weighting constant for each instrument, N is the simulated density of neutrons from the moderator, and $V_j(\lambda)$ is given in (1).

We have for each instrument calculated the spatial transmission function, $T_r(\mathbf{r})$, as shown in the examples above, and listed in Ref. 4. The results show that for most instruments, the transmission peaks strongly in a 3–5 cm diameter circle (or square) in the center of the moderator. This effect results for some instruments from the use of elliptical guides, for others from using tight collimation and straight guides. Thus, it can for these simple guide systems be advantageous to concentrate the flux in a hot spot, while the size of the emitting part of the moderator can be limited, e.g., by reflectors. In this way, it should be possible to simultaneously increase the useful neutron flux and decrease the emission of fast neutrons. For each instrument, we have calculated the effect of producing a circular, 3 cm diameter, hot spot with 100% higher emittance – while maintaining the total emittance of the moderator. This set-up is close to what was presented in Ref. 32. For most instruments, the gain factor of such a hot spot is around 30%, while few instruments show a full 100% gain.

It should be added that more elaborate guide systems, in particular, an optimized guide extraction system for instruments with a pulse shaping chopper close to the moderator, will modify this picture. This problem will be addressed by further simulation work.[29]

($f = 14$ Hz), two boundary conditions were considered: (1) the time-average power is planned to be 5 MW. (2) the peak accelerator current cannot exceed 50 mA. The 5 MW number is judged to be important, so as to at least match the best existing instruments over the largest possible range. The limitation on the peak current results from a judgement, based on the experience of the SNS linear accelerator, as to the optimal compromise between performance, reliability and cost. In the interest of maximizing the instrument performance, it is clearly advantageous to push for the highest peak flux which the accelerator and target assembly can provide. We can therefore consider the 50 mA peak current as our specification, rather than an upper limit. These boundary conditions reduce the number of degrees of freedom when choosing τ and T from 2 to 1, as follows. The peak power on target is given by the product of the peak current and proton energy of 2.5 GeV. At 50 mA peak current, the instantaneous power is 125 MW. In order to achieve a time-average power of 5 MW, the source therefore needs to operate at a duty cycle τ/T of 5 MW/125 MW $= 1/25$, as a direct consequence of our two boundary conditions. If we set the repetition period to 100 ms (10 Hz), the pulse length will be 4 ms. At $T = 50$ ms repetition period ($f = 20$ Hz), the pulse length is 2 ms. The range of τ and T covered in the present study only overlaps partially with the duty cycle $\tau/T = 1/25$. In order to study the instrument performance over the 10–25 Hz frequency range, while maintaining a duty cycle of 1/25, we extrapolate based on the data in Tables IV and V and Eq. (6) that the performance of the instrument suite does not depend upon the value of the source frequency.

In general, our results imply that factors other than the flux-related FoM used here should be decisive when determining the time structure for a long-pulse spallation source. For the case of ESS, the time structure has now been locked to $\tau = 2.86$ ms and $f = 14$ Hz, as the best compromise between performance, reliability, and cost. The detailed considerations are outside the scope of this article.

B. Further design and optimization of ESS instruments

The instrument design work for ESS is currently taking place in a setting which is very different from when the design work described in the present paper was taking place. A large number of the neutron laboratories and university groups working in neutron scattering in Europe are now engaged in the process of designing instruments for the ESS and the number is still increasing. About 40 different concepts for instruments are currently being optimized, some pursued by researchers in partner countries and some by ESS instrument scientists. A subset of these concepts has been assembled into a reference suite of instruments which is described in the ESS Technical Design Report.[33] The reference suite has been chosen to maximize the scientific impact of the ESS by addressing a broad science case, while in each case being fully optimized to benefit from the natural strengths of the long-pulse concept. The choice of instruments to be built at the ESS will take place as a staged process in consultation with the

[1]See www.ess-scandinavia.eu for the home page of the ESS project.
[2]*The ESS Project*, edited by D. Richter (Jülich Research Center, 2002), Vol. I.
[3]*The ESS Project*, edited by D. Richter (Jülich Research Center, 2002), Vol. IV.
[4]See sim.esss.dk for the home page.
[5]K. Lefmann, H. Schober, and F. Mezei, Meas. Sci. Technol. **19**, 034025 (2008).
[6]K. Lefmann, U. Filges, F. Treue, J. J. K. Kirkensgård, B. Plesner, K. S. Hansen, and K. H. Klenø, Nucl. Instrum. Methods A **634**, S1 (2011).
[7]M. Sales, S. L. Holm, K. Lieutenant, and K. Lefmann, J. Phys. Soc. Jpn. **80**, SB018 (2011).
[8]K. H. Klenø and K. Lefmann, J. Phys. Soc. Jpn. **80**, SB004 (2011).
[9]K. H. Klenø, P. K. Willendrup, E. Knudsen, and K. Lefmann, Nucl. Instrum. Methods A **634**, S100 (2011).
[10]K. H. Klenø, S. Kynde, G. Nagy, K. Mortensen, K. Lefmann, J. Kohlbrecher, and L. Arleth, "A compact time-of-flight SANS instrument optimised for measurements of small sample volumes at the European Spallation Source," J. Appl. Crystallogr. (submitted).
[11]J. O. Birk *et al.*, "Simulations of the inverse-geometry time-of-flight spectrometer CAMEA for the European Spallation Source" (unpublished).
[12]A. Vickery *et al.*, "Comparing thermal spectrometers for a long-pulse spallation source" (unpublished).
[13]R. K. Crawford *et al.*, Report of the Long-pulse Neutron Instrumentation Workshop, Frascati, August 2009, 2010.
[14]F. Mezei, J. Neutron Res. **6**, 3 (1997).
[15]G. Zsigmond *et al.*, Appl. Phys. A **74**, S224 (2002).
[16]H. Schober *et al.*, Nucl. Instrum. Methods A **589**, 34 (2008).
[17]K. Lefmann *et al.*, Report from the Ven 2008 meeting (unpublished).
[18]K. Lieutenant and F. Mezei, J. Neutron Res. **14**, 177 (2006).
[19]M. Russina and F. Mezei, Proc. SPIE **4785**, 24 (2002).
[20]F. Mezei, M. Russina, and S. Schorr, Physica B **276**, 128 (2000).
[21]M. Russina and F. Mezei, Nucl. Instrum. Methods A **604**, 624 (2009).
[22]M. Nokamura *et al.*, J. Phys. Soc. Jpn. **78**, 093002 (2009).
[23]F. Mezei, *ESS Reference Moderator Characteristics for Generic Instrument Performance Evaluation* (ESS Project, Jülich, 2000), see also

European scientific community and will result in the reference suite gradually evolving into the actual instrument which will be available at the ESS.

ACKNOWLEDGMENTS

First of all we are strongly indebted to Ch. Vettier for initiating this project and to D. Argyriou for keeping up the urgency of the simulations. We would further like to thank the ESSS SAG, the ESS SAC, and H. M. Rønnow for illuminating discussions.

This project was supported by the Danish, Norwegian, and German contributions to the Design Update phase of the ESS. J. O. Birk was supported by PSI and the Danish Research Council through the graduate school C:O:N:T.

http://rencurel.essworkshop.org/documents/ess_itg/ESS-moderators.pdf.
[24]K. H. Klenø, K. Lieutenant, K. H. Andersen, and K. Lefmann, Nucl. Instrum. Methods A **696**, 75 (2012).
[25]SwissNeutronics AG, personal communication (2012), see also www.swissneutronics.ch.
[26]K. H. Klenø *et al.*, "Effects of non-idealities in long neutron guides" (unpublished).
[27]P. Allenspach, P. Böni, and K. Lefmann, Proc. SPIE **4509**, 157 (2001).
[28]Mirrotron Ltd., personal communication (2012), see also www.mirrotron.kfkipark.hu.
[29]M. Bertelsen *et al.*, "Exploring performance of neutron guide systems using pinhole beam extraction," Nucl. Instrum. Methods. A (submitted).
[30]U. Filges, personal communication (2012).
[31]K. Lefmann and K. Nielsen, Neutron News **10/3**, 20 (1999), see also www.mcstas.org.
[32]Y. Kiyanagi *et al.*, in Proceedings of the ICANS conference, PSI report, 2010.
[33]*ESS Technical Design Report*, edited by S. Peggs (European Spallation Source ESS AB, 2013).
[34]L. D. Cussen *et al.*, Nucl. Instrum. Methods A **705**, 121 (2013).

Appendix C

Powder Diffractometers at Long-pulsed Sources

This proceeding article below describes the two powder diffractometers simulated for the study of the impact of the source time structure of the European Spallation Source for a generic instrument suite found in appendix B [40].

My contribution to the article was simulating the thermal powder diffractometer using Wavelength Frame Multiplication in addition to composing the text. (Note that each inserted article page is spread across two pages in this text.)

Proc. Int. Workshop NASCES11
J. Phys. Soc. Jpn. **80** (2011) SB018

Powder Diffractometers at Long-pulsed Sources

Morten Sales[1,2], Sonja Lindahl Holm[1,2], Klaus Lieutenant[3], and Kim Lefmann[1,2]

[1]*European Spallation Source, St. Algaten 4, 223 50 Lund, Sweden*
[2]*Niels Bohr Institute, Universitetsparken 5, 2100 Copenhagen, Denmark*
[3]*Helmholtz Zentrum Berlin, Hahn-Meitner-Platz 1, 14109 Berlin, Germany*

(Received April 30, 2011)

We have investigated the performance of a cold and a thermal neutron powder diffractometer installed at at long-pulsed source with the use of Monte Carlo ray tracing simulations. We show that the cold powder diffractometer will be a very powerful instrument when a relaxed resolution can be accepted - e.g. for magnetic studies. A comparison between a thermal powder diffractometer with and without Wavelength Frame Multiplication (WFM) show that the WFM technique can be used to achieve shorter instrument length without losing flux. The thermal powder diffractometer will be competitive with the existing high resolution powder diffractometers.

KEYWORDS: Instrumentation, Powder diffractometer, ESS, Wavelength Frame Multiplication, Monte Carlo ray tracing, McStas

1. Introduction

Neutron instrumentation for long-pulsed target stations (LPTS) is a rather new field of study, spawned by the forthcoming construction of the European Spallation Source[1,2] (ESS); the first long-pulsed spallation source ever to be built.

At short-pulsed target stations (SPTS), powder diffractometers have a natural high resolution that is not immediately realised by installing conventional powder diffractometers at a LPTS. However, in order to accommodate a broad user community for ESS, it is highly desirable to include diffraction wavelength band is fixed around $\lambda_{mean} = 4.5$ Å which means that this instrument should use neutrons coming from a cold (H_2) moderator. The wavelength resolution of this instrument is set to be $\delta\lambda/\lambda = 0.01$ at λ_{mean}. The CPD is a simple instrument using the full pulse length and using choppers only to avoid frame overlap. Due to the instrument length an elliptical guide is used to transport the neutrons from the source to the sample. The guide has m = 6 at the end parts and m = 1 in the middle.[6] The detector is a cylindrical time of flight detector with a radius of 2 m. For the base line setting of the source (period, $T = 60$ ms and pulse length, $\tau = 2.0$ ms) the length of

studies in the ESS design. Hence, to achieve high resolution for powder diffractometers installed at the ESS, it is necessary to cut the pulse by using a pulse shaping chopper.

Earlier studies comparing the performance of a powder diffractometer at a SPTS to its performance if installed at a LPTS has been performed by Lieutenant and Mezei.[3] In their design of the LPTS instrument they used a technique called Wavelength Frame Multiplication (WFM)[4] where the pulse shaping chopper creates several sub-pulses per source period in this way cutting the pulse to get higher resolution, shorter instrument, and larger wavelength band.

The work we here present is an investigation of the performance of two different types of powder diffractometers:

- A Cold Powder Diffractometer (CPD) with low resolution designed to study magnetic structures and phase transitions.[5]
- Two Thermal Powder Diffractometers (TPD) with a high resolution for structural analysis.

The TPD simulation will include an evaluation of the benefits of WFM. The instruments studied are fairly long and have been simulated with an elliptical guide design that excels when long flight paths are needed.[6]

The Monte Carlo simulations and instrument optimisations have been done using the McStas[7] software package.

2. Cold Powder Diffractometer

This prototype high-flux low-resolution diffractometer is meant for magnetic structure determination and phase transition studies, possibly under extreme environments.[5] The the CPD is L = 175.7 m and the wavelength band goes from λ_{min} = 3.85 Å to λ_{max} = 5.15 Å.

2.1 *Design and Simulations*

The layout of the instrument is shown in figure 1.

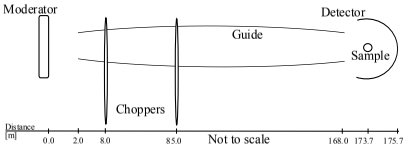

Fig. 1. Layout of the CPD when using the full pulse length of 2 ms. The 175.7 m long instrument with an elliptical guide has two choppers to avoid frame overlap. The sample size is 1×1 cm^2 and the detector is a cylindrical time of flight detector with a radius of 2 m. The length of the CPD varies with the choice of the pulse length. The layout is not to scale.

The length of the instrument at constant wavelength resolution ($\delta\lambda/\lambda = 0.01$ at $\lambda = 4.5$ Å) depends of the pulse length. The length (L) of the instrument depends on the pulse length, as derived from the time-of-flight equation:

$$t = \alpha L \lambda \qquad (1)$$

where $\alpha = 2.528 \cdot 10^{-4}\ \frac{s}{m\text{Å}}$.

$$L = \frac{\tau}{\frac{\delta\lambda}{\lambda}\alpha\lambda_{mean}} \tag{2}$$

The lengths from moderator to detector of the CPD for the four investigated values of τ are shown in table I. The wavelength band will change with both pulse length and period and can be calculated by using:

Table I. Instrument lengths from moderator to detector of the CPD as a function of pulse length and with constant wavelength resolution ($\delta\lambda/\lambda$ = 0.01 at λ = 4.5 Å).

τ [ms]	1.0	1.25	1.5	2.0
L [m]	87.9	109.9	131.9	175.8

$$\lambda_{max} - \lambda_{min} = \frac{T - \tau}{\alpha L} \tag{3}$$

The band widths are shown in table II for 20 different moderator settings studied for the ESS design update.[8)]

The maximum allowed divergence at the sample is set to ±0.45° for the CPD. This is derived with error propagation of the Bragg law:

$$\left(\frac{\delta d}{d}\right)^2 = \left(\frac{\delta\lambda}{\lambda}\right)^2 + \left(\frac{\delta\theta}{\tan\theta}\right)^2 \tag{4}$$

So for $(\delta\lambda/\lambda) \approx (\delta\theta/\tan\theta)$, $\delta\lambda/\lambda = 0.01$ and a scattering angle, 2θ, of 115°, thereby aiming to simulate typical, not best, 20×20 cm^2. The wavelength distribution from the moderator is described by the McStas ESS long-pulsed cold source.[9)]

2.2 *Performance*

The CPD has a very good performance at a long-pulsed source. We have investigated the performance of the CPD for a number of time structures for the ESS moderator, assuming that the peak moderator flux is constant.[8)] Here, the instrument length has been adjusted by the value of τ to obtain the same $\delta\lambda/\lambda$ wavelength resolution for all simulations. For the base line time structure of the moderator the neutron flux at the sample (1×1 cm^2) is $5.89(10)\cdot10^8$ neutrons/s/cm^2. For the other moderator time structures investigated, the neutron flux values have been normalised to the base line flux and are displayed in table III.

Table III. Relative flux values for the CPD with constant peak flux, normalised to the moderator base line setting value.

T/τ [ms]	1.0	1.25	1.5	2.0
100	1.2	1.2	1.1	1.0
80	1.1	1.1	1.1	1.0
60	1.1	1.1	1.0	1.0
50	1.0	1.1	1.0	1.0
40	1.0	1.0	1.0	1.0

2.3 *Effect of moderator hot spot*

It has been shown that grooved moderators with hot spots

wavelength resolution, this gives a divergence limitation of 0.9° = ±0.45°. This result should be seen as an approximation, since the correct uncertainties in divergence and wavelength can only be achieved from analysing their distribution functions at the sample.

Table II. Width of wavelength bands [Å] of the CPD for 20 different moderator time structures.

T/τ [ms]	1.0	1.25	1.5	2.0
100	4.46	3.56	2.96	2.21
80	3.56	2.84	2.36	1.76
60	2.66	2.12	1.76	1.31
50	2.21	1.76	1.46	1.08
40	1.76	1.40	1.16	0.86

We used an elliptical guide for neutron transport and chose to terminate the guide 6 m before the sample position because there is no significant intensity loss of neutrons with a divergence below ±0.45°. However, by doing so the background of neutrons with a higher divergence is strongly reduced, since it is the last part of the elliptical guide that is responsible for these neutrons. Only neutrons with a divergence lower than the limit of ±0.45° were included in the flux values given in section 2.2. The shape of the guide is optimised to make neutrons with a divergence below the divergence threshold hit a sample with the size of 1×1 cm^2 coming from a moderator that emits an uniformly distributed flux from a 12×12 cm^2 surface area. The broadest section of the guide in figure 1 is can be useful for long-pulsed spallation sources,[10] and so we have studied the point of origin in the CPD of useful neutrons (with a divergence below ±0.45°) that hits the sample. Results are shown in figure 2. It is seen that the CPD would benefit from a neutron hot spot at the center of the moderator surface since most neutrons stem from the central part of the moderator as a consequence of the elliptical guide shape. To quantify this, the uniformly distributed moderator has been replaced by a moderator with the same overall summed flux but a hot spot with a diameter of 3 cm and twice the intensity. For the baseline setting the CPD gains 28 % more flux on the sample by having such a moderator hot spot.

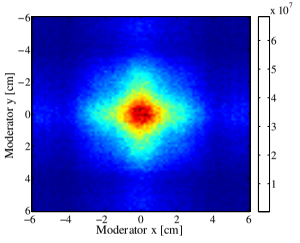

Fig. 2. Colour plot of the moderator surface showing how the useful neutrons (with a divergence below ±0.45°) hitting the sample are distributed for the CPD. This origin plot is made from the simulation of the moderator base line setting. Colour bar is in neutrons/second/pixel.

3. Thermal Powder Diffractometer

The TPD is a work horse instrument at any neutron facility, used for the study of crystal structure and chemical phases of materials. We chose to investigate such an instrument with a wavelength resolution of $\delta\lambda/\lambda = 0.1$ % and almost 4π detector coverage comparable to GEM at ISIS.[11)]

To obtain this high resolution a diffractometer needs to be adequately long or use a short pulse; e.g. a diffractometer using neutrons with wavelengths around 1.5 Å, 0.1 % wavelength resolution, a pulse length of 2 ms, and filling the whole time frame, will need to be more than 5 kilometres long! So in order to have a reasonable instrument length the pulse needs to be shortened by a pulse shaping chopper.

3.1 Wavelength Frame Multiplication

In order to fill the time frame, the instrument length is $L = L_{ps} \cdot T/\tau$, where L_{ps} is the distance from the moderator to the pulse shaping chopper. For the baseline source time structure and the shortest possible value of $L_{ps} = 6$ m the instrument length will be 186 m. A further shortening of the instrument length can be obtained by implementing the WFM[4)] method where several short pulses in combination fill the frame as shown in figure 3.

The main ideas behind the design of the instrument using WFM is taken from an article by K. Lieutenant and F. Mezei.[3)] The fast rotating pulse shaping chopper acts as a new virtual short-pulsed source with shorter pulse length and period. The aim of this investigation is to give an overview of the benefits and disadvantages of using WFM.

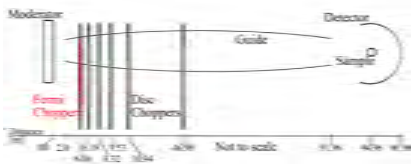

Fig. 4. Layout of the thermal powder diffractometer with WFM. The guide is elliptical with m = 6 at the guide ends and m = 1 in the middle section.[6)] The detector is cylindrical and placed 2 m from the 3×3 mm^2 sample.

λ is the wavelength for which the required wavelength resolution is wanted. This has for the TPD been set to 1.5Å. The maximum allowed divergence on the sample is set to match the wavelength resolution ($\pm 0.045°$ for $\delta\lambda/\lambda = 1 \cdot 10^{-3}$ and $2\theta = 115°$) calculated in the same way as for the CPD (see equation (4)).

Just after the pulse shaping chopper the pulse selecting chopper is situated. This chopper is rotating with the same period as the source, T, and it picks out the required number of pulses, n.

$$\mathrm{n} = \left\lceil \frac{T}{\tau} \cdot \frac{L_{\mathrm{ps}}}{L - L_{\mathrm{ps}}} \right\rceil \tag{6}$$

See table IV for the number of frames used for different combinations of T and τ.

The rest of choppers further defines the pulses, prevents frame

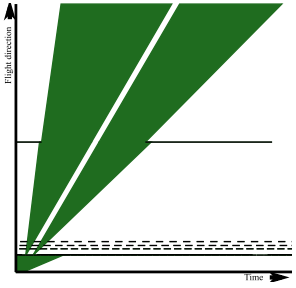

Fig. 3. Time of flight diagram showing the principle Wavelength Frame Multiplication for $n = 2$. The tail of the source pulse has not been included.

3.2 Design and Simulations

We have investigated the powder diffractometer both with and without WFM.

The overall layout of the instrument is similar to the CPD and can be seen in figure 4. The 12×12 cm^2 moderator has been simulated with a wavelength distribution described by the McStas ESS long-pulsed thermal source.[9] The first chopper is the fast rotating pulse shaping chopper that creates several sub-pulses per source period. Its opening time, τ', is calculated to match the required wavelength resolution:

$$\tau' = \alpha \left(L - L_{\mathrm{ps}}\right) \lambda \frac{\delta\lambda}{\lambda} \tag{5}$$

overlap between pulses or sub-pulses and eliminates cross talk.[3] Figure 4 depicts an instrument using WFM and having a length of $L_{\mathrm{Total}} = 96.96$ m. To obtain the same wavelength resolution without WFM the length would have been: $L_{\mathrm{no\ WFM}} = (L - L_{\mathrm{ps}}) \cdot \mathrm{n}$. The wavelength bandwidth for the TPD using WFM is given by $T/(\alpha \cdot (L - L_{\mathrm{ps}}))$ and is presented in table V.

Table IV. Number of sub pulses per original pulse, n, using WFM and keeping the instrument length at 96.96 m.

T/τ [ms]	1.0	1.25	1.5	2.0
100	7	6	5	4
80	6	5	4	3
60	4	4	3	2
50	4	3	3	2
40	3	3	2	2

Table V. Width of wavelength band with $L_{\mathrm{Total}} = 96.96$ m and using WFM

T [ms]	100	80	60	50	40
Wavelength bandwidth [Å]	4.35	3.48	2.61	2.18	1.74

3.3 Performance

For the baseline setting the flux at the sample position is found to be $3.25(4) \cdot 10^5$ neutrons/second/cm^2 for $\delta\lambda/\lambda = 1 \cdot 10^{-3}$ and using WFM. Without the use of WFM for the

same wavelength resolution and source time structure, the flux at the sample is higher: $5.137(18) \cdot 10^5$ neutrons/second/cm^2. Without WFM the bandwidth is halved and the higher flux is caused by a narrower wavelength band with more intense wavelengths being selected. For an instrument without WFM at the baseline time structure to have the same wavelength band as the instrument with WFM, it needs to be run with two different time delays of the choppers. In this case the average flux at the sample position is $3.256(9) \cdot 10^5$ neutrons/second/cm^2. So if the wavelength band is unimportant, using WFM will give a loss of 37 % of the useful neutrons. However, comparing instruments with the same wavelength band the instrument length is halved and the flux is the same when using WFM. The downside is that more choppers are needed to use WFM and that data analysis may become more difficult.

Figure 5 shows the flux at the sample for the baseline setting with WFM for different wavelength resolutions. It can be seen that a significant gain in intensity at the sample can be achieved by relaxing the resolution. Comparing to the GEM[11,12] instrument at ISIS that for a resolution of $\delta d/d$ of $\sim 4 \cdot 10^{-3}$ at 115° scattering angle has a flux of $\sim 2 \cdot 10^6$ neutrons/second/cm^2 our simulations show a powerful instrument with around four times the flux.

moderator surface the useful neutrons originate. It is seen that almost all the neutrons originate from the central 3×3 cm^2 of the moderator. So by having a moderator hot spot with a diameter of 3 cm and twice the intensity (but still keeping the same overall intensity) the flux at the sample position is found to rise by 93 % in the case of $T = 60$ ms, $\tau = 2$ ms and using WFM. Simulations of the longer instrument without WFM show that it will gain 100 % in flux at the sample from having a moderator hot spot.

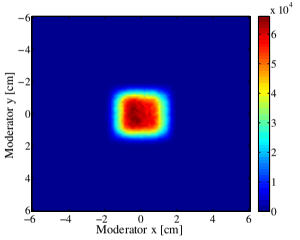

Fig. 6. Origin plot for the TPD with WFM, $T = 60$ ms, $\tau = 2$ ms and $\frac{\delta\lambda}{\lambda} = 10^{-3}$. Colour bar is in neutrons/second/pixel.

4. Conclusion

Our simulations show that it is feasible to install powder diffractometers at a long-pulsed source like the ESS.

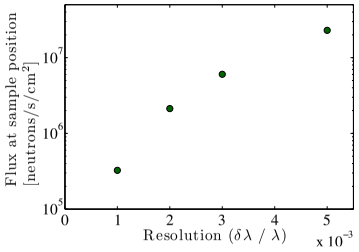

Fig. 5. Flux at sample position for the thermal powder diffractometer with WFM and T = 60 ms, τ = 2 ms. Simulations are performed for different wavelength resolutions with matching divergence limitations (at $2\theta = 115°$) on the sample.

Table VI shows the relative flux at the sample position simulated for different combination of T and τ.

Table VI. Relative flux at sample position for the TPD with WFM for constant peak flux and normalised by the T = 60 ms and τ = 2 ms result. $\delta\lambda/\lambda = 1 \cdot 10^{-3}$ and maximum divergence at the sample is ±0.045°.

T/τ [ms]	1.0	1.25	1.5	2.0
100	0.38	0.45	0.51	0.61
80	0.48	0.57	0.63	0.79
60	0.63	0.74	0.83	1.00
50	0.74	0.86	0.96	1.10
40	0.89	1.02	1.09	1.18

3.4 Effect of moderator hot spot

As with the CPD we have studied the effect of having a moderator hot spot. Figure 6 shows from what part of the

The cold powder diffractometer with relaxed resolution is a very potent instrument with a tremendous flux and is due to utilise the full pulse.

A high resolution thermal powder diffractometer can use wavelength frame multiplication to shorten the instrument length, without losing flux at the sample. If only a narrow wavelength band is needed, however, an instrument without WFM has the highest flux at the sample position.

For both the cold and the thermal powder diffractometers there is a significant gain by having a moderator with a 3 cm diameter, factor 2 hot spot. Our simulations show that this can increase the flux at the sample position significantly up to a full factor 2.

1) H. Schober et al. Nuclear Instruments and Methods in Physics Research A 589 (2008) 34-46. 2008.
2) F. Mezei. J. Neutron Research, Vol. 6, pp. 332. 1997.
3) K. Lieutenant and F. Mezei. *Journal of Neutron Research*, 14(2):177–191, June 2006.
4) M. Russina and F. Mezei, Proc. SPIE (Int. Soc. f. Opt. Eng.) 4785 24 (2002).
5) The ESS design report, Vol III, Jülich 2002.
6) K.H. Klenø et al, in preparation (2011).
7) P.K. Willendrup, E. Farhi, K. Lefmann, Physica B 350, e735 (2004).
8) K. Lefmann et al. to be submitted (2011).
9) The McStas library. http://www.mcstas.org/.
10) Y. Ogawa et al. J. Neutron Research, Vol. 6, pp. 197-204.
11) W.G. Williams et al. Physica B 241 243 (1998) 234 236.
12) A.W. Hewat. Physica B 385-386 (2006) 979-984.

Appendix D

McStas Code

This is Monte Carlo Ray-Tracing Simulation code used in Chapter 3. The code is for use with the McStas 2.0 simulation package [56].

D.1 SEMSANS instrument

The `Analyser_ideal` component is written by Erik Knudsen and works as an (unphysical) ideal analyser of neutron spin direction. The `Pol_pi_2_rotator` component is also written by Erik Knudsen and rotates the neutron spin 90 degrees around a given vector. It is an ideal unphysical version of a V-coil. The `Pol_triafield` is witten by me and is an ideal unphysical triangular field (see section D.2). The amount of precession a neutron spin would experience

passing through the field is calculated and applied. More information can be found in the code for the component. The position of the two V-coils in the middle responsible for the 180 degree spin flip can be scanned with the parameter `flippos`. The start orientation of the neutron spin is controlled with the parameter `FLIP` where 1 is down and -1 is up. This parameter works in the first V-coil. Before the detector a choice of single slit, double slit or grating can be made by commenting the other options. After the simulation where `flippos` has been scanned for both `FLIP` 1 and -1, the output from the ToF detector can be combined into e.g. a 2D colorplot of Visibility signal vs ToF (wavelength) and `flippos` such as in Fig. 3.3 and 3.4.

Instrument code:

```
/*******************************************************************************
* McStas instrument definition URL=http://www.mcstas.org
* Written by: Morten Sales
* Date: 2014
* Origin: Copenhagen, Berlin, Delft
* Release: McStas 2.0
* Instrument site: TU Delft.
* Instrument: Time-of-Flight SEMSANS instrument
* with 2 isosceles triangular field coils
*******************************************************************************/

DEFINE INSTRUMENT Delft_SEMSANS(
 triacoil_depth  =  1.93500e-01, //Half of the tria. coil depth (1 right tria.) [m]
 triacoil_width  =  7.04282e-02, //xwidth of triangular coil [m]
 triacoil_height =  3.00000e-01, //yheight of triangular coil [m]
 pol_zdepth      =  9.30000e-01, //Depth of the polariser along z [m]
 vcoil_zdepth    =  1.50000e-01, //Depth along z of the v-coil flipper [m]
 Guide1_depth    =  1.65000e-02, //Depth of first precession field section [m]
 Guide2_depth    =  3.31500e-01, //Depth of second precession field section [m]
 Guide3_depth    =  3.31500e-01, //Depth of third precession field section [m]
 Guide4_depth    =  5.65000e-02, //Depth of fourth precession field section [m]
 Bguide          = -5.00000e-04, //Field strength of precession field [T]
 Bextra          = -2.12000e-02, //Field strenth of extra field in guide field 1 [T]
 Bt2             = -4.44000e-03, //Field in first triangular coil [T]
```

```
  Bt1             = -2.56000e-03, //Field in second triangular coil [T]
  DLambda         =  4.16637e+00, //Wavelength spread from source (half of it) [AA]
  Lambda          =  4.55950e+00, //Mean wavelength [AA]
  flippos         =  3.10000e-02, //Position (rel. to vcoil_34_pos) of pi-flipper [m]
  FLIP            =  1.00000e+00, //Choose polarisation (1 is down, -1 is up)
  chop1_pos       =  5.00000e-01, //Position of first chopper [m]
  chop2_pos       =  9.74000e-01, //Position of second chopper [m]
  pol_pos         =  1.90700e+00, //Position of polariser [m]
  analyser_pos    =  6.07200e+00, //Position of analyser [m]
  grating_w       =  1.57000e-03, //Width of transmitting part of grating [m]
  grating_a       =  2.93000e-03, //Width of absorbing part of grating [m]
  slit_1_pos      =  2.95700e+00, //Position of first slit [m]
  slit_2_pos      =  5.43700e+00, //Position of second slit [m]
  Guide1_pos      =  3.30700e+00, //Position of first precession field [m]
  Guide2_pos      =  3.71050e+00, //Position of second precession field [m]
  Guide3_pos      =  4.34200e+00, //Position of third precession field [m]
  Guide4_pos      =  5.06050e+00, //Position of fourth precession field [m]
  vcoil_12_pos    =  3.15700e+00, //Position of first v-coil pair [m]
  vcoil_34_pos    =  4.19200e+00, //Position of second v-coil pair [m]
  vcoil_56_pos    =  5.26700e+00, //Position of third v-coil pair [m]
  triacoil_1_pos  =  3.51700e+00, //Position of first triangular coil (centre) [m]
  triacoil_2_pos  =  4.86700e+00, //Position of second triangular coil (centre) [m]
  grating_pos     =  6.75700e+00, //Position of grating [m]
  detector_pos    =  6.95700e+00, //Position of detector [m]
  tlow            =  2.19052e+03, //tmin of detector [mu-s]
  thigh           =  1.21474e+04) //tmax of detector [mu-s]

/* The DECLARE section allows us to declare variables or small  */
/* functions in C syntax. These may be used in the whole instrument. */
DECLARE
%{
%}

/* The INITIALIZE section is executed when the simulation starts  */
/* (C code). You may use them as component parameter values.   */
INITIALIZE
%{
%}
/* Here comes the TRACE section, where the actual  */
/* instrument is defined as a sequence of components. */
TRACE

COMPONENT Origin = Progress_bar()
 AT(0,0,0) ABSOLUTE

// SOURCE
COMPONENT source = Source_simple(
   radius=0, dist = slit_1_pos, focus_xw=20e-3, focus_yh=20e-3,
   xwidth = 2e-3, yheight = 2e-3,
   lambda0 = Lambda,dlambda = DLambda)
 AT (0, 0, 0) RELATIVE Origin

```

```
77 // FIRST
78 COMPONENT chop1 = DiskChopper(radius=0.21, theta_0=20, nu=25,
79   nslit=2, phase=-10, isfirst=1)
80  AT (0, 0, chop1_pos) RELATIVE Origin
81
82 // Second chopper
83 COMPONENT chop2 = DiskChopper(radius=0.21, theta_0=20, nu=25,
84   nslit=2, phase=20-10, isfirst=0)
85  AT (0, 0, chop2_pos) RELATIVE Origin
86
87 // POLARISER
88 COMPONENT polarizer = Set_pol(py=1)
89  AT (0, 0, pol_pos+0.5*pol_zdepth) RELATIVE Origin
90
91 // FIRST SLIT
92 COMPONENT slit_1 = Slit(
93   xwidth=15e-3,yheight=15e-3)
94  AT (0,0,slit_1_pos) RELATIVE Origin
95
96 // FIRST V-COIL OF FIRST V-COIL PAIR
97 COMPONENT vcoil1=Pol_pi_2_rotator(
98   xwidth=0.15,yheight=0.15,zdepth=vcoil_zdepth,rx=0,ry=0,rz=FLIP*1)
99  AT (0,0,vcoil_12_pos-vcoil_zdepth) RELATIVE Origin
100
101 // SECOND V-COIL OF FIRST V-COIL PAIR
102 COMPONENT vcoil2=Pol_pi_2_rotator(
103   xwidth=0.15,yheight=0.15,zdepth=vcoil_zdepth,rx=0,ry=1,rz=0)
104  AT (0,0,vcoil_12_pos) RELATIVE Origin
105
106 // START GUIDEFIELD 1
107 COMPONENT Guide_field1 = Pol_simpleBfield(xwidth=0.4, yheight=0.4,
108   zdepth=Guide1_depth,Bx=0, By=Bguide+Bextra, Bz=0,
109   fieldFunction=const_magnetic_field)
110  AT (0,0,Guide1_pos) RELATIVE Origin
111
112 // STOP GUIDE FIELD 1
113 COMPONENT Guide_field1_cp = Pol_simpleBfield_stop(magnet_comp_stop=Guide_field1)
114  AT (0,0,Guide1_pos+Guide1_depth) RELATIVE Origin
115
116 // TRIA COIL 1
117 COMPONENT triacoil_1=Pol_triafield(
118   xwidth=triacoil_width,yheight=triacoil_height,zdepth=2*triacoil_depth,
119   B=Bt1, Bguide=Bguide)
120  AT (0,0,triacoil_1_pos-triacoil_depth) RELATIVE Origin
121
122 // START GUIDEFIELD 2
123 COMPONENT Guide_field2 = Pol_simpleBfield(xwidth=0.4, yheight=0.4,
124   zdepth=Guide2_depth+flippos, Bx=0, By=Bguide, Bz=0,
125   fieldFunction=const_magnetic_field)
126  AT (0,0,Guide2_pos) RELATIVE Origin
127
128 // STOP GUIDE FIELD 2
```

```
COMPONENT Guide_field2_cp = Pol_simpleBfield_stop(magnet_comp_stop=Guide_field2)
 AT (0,0,Guide2_pos+Guide2_depth+flippos) RELATIVE Origin

// FIRST V-COIL OF SECOND V-COIL PAIR
COMPONENT vcoil3=Pol_pi_2_rotator(
  xwidth=0.15,yheight=0.15,zdepth=vcoil_zdepth,rx=0,ry=0,rz=1)
 AT (0,0,vcoil_34_pos-vcoil_zdepth+flippos) RELATIVE Origin

// SECOND V-COIL OF SECOND V-COIL PAIR
COMPONENT vcoil4=Pol_pi_2_rotator(
  xwidth=0.15,yheight=0.15,zdepth=vcoil_zdepth,rx=0,ry=0,rz=1)
 AT (0,0,vcoil_34_pos+flippos) RELATIVE Origin

// START GUIDEFIELD 3
COMPONENT Guide_field3 = Pol_simpleBfield(xwidth=0.4, yheight=0.4,
  zdepth=Guide3_depth-flippos, Bx=0, By=Bguide,
  Bz=0,fieldFunction=const_magnetic_field)
 AT (0,0,Guide3_pos+flippos) RELATIVE Origin

// STOP GUIDE FIELD 3
COMPONENT Guide_field3_cp = Pol_simpleBfield_stop(magnet_comp_stop=Guide_field3)
 AT (0,0,Guide3_pos+Guide3_depth) RELATIVE Origin

// START TRIA COIL 2
COMPONENT triacoil_2=Pol_triafield(
  xwidth=triacoil_width,yheight=triacoil_height,zdepth=2*triacoil_depth,
  B=Bt2, Bguide=Bguide)
 AT (0,0,triacoil_2_pos-triacoil_depth) RELATIVE Origin

// START GUIDEFIELD 4
COMPONENT Guide_field4 = Pol_simpleBfield(xwidth=0.4, yheight=0.4,
  zdepth=Guide4_depth, Bx=0, By=Bguide, Bz=0,
  fieldFunction=const_magnetic_field)
 AT (0,0,Guide4_pos) RELATIVE Origin

// STOP GUIDE FIELD 4
COMPONENT Guide_field4_cp = Pol_simpleBfield_stop(magnet_comp_stop=Guide_field4)
 AT (0,0,Guide4_pos+Guide4_depth) RELATIVE Origin

// FIRST V-COIL OF THIRD V-COIL PAIR
COMPONENT vcoil5=Pol_pi_2_rotator(
  xwidth=0.15,yheight=0.15,zdepth=vcoil_zdepth,rx=0,ry=1,rz=0)
 AT (0,0,vcoil_56_pos-vcoil_zdepth) RELATIVE Origin

// SECOND V-COIL OF THIRD V-COIL PAIR
COMPONENT vcoil6=Pol_pi_2_rotator(
  xwidth=0.15,yheight=0.15,zdepth=vcoil_zdepth,rx=0,ry=0,rz=1)
 AT (0,0,vcoil_56_pos) RELATIVE Origin

// SECOND SLIT
COMPONENT slit_2=Slit(
  xwidth=15e-3,yheight=15e-3)
```

```
AT(0,0,slit_2_pos) RELATIVE Origin

// ANALYSER
COMPONENT analyser=Analyser_ideal(mx=0,my=1,mz=0)
AT(0,0,analyser_pos) RELATIVE Origin

// THIS IS GRATING
COMPONENT GratingSlit1_1 = Slit(xwidth=grating_w,yheight=5e-3)
 AT (-2.0*grating_w - 2.0*grating_a, 0, grating_pos) RELATIVE Origin
GROUP Grating

COMPONENT GratingSlit1_2 = Slit(xwidth=grating_w,yheight=5e-3)
 AT (-1.0*grating_w - 1.0*grating_a, 0, grating_pos) RELATIVE Origin
GROUP Grating

COMPONENT GratingSlit1_3 = Slit(xwidth=grating_w,yheight=5e-3)
 AT (0, 0, grating_pos) RELATIVE Origin
GROUP Grating

COMPONENT GratingSlit1_4 = Slit(xwidth=grating_w,yheight=5e-3)
 AT (1.0*grating_w + 1.0*grating_a, 0, grating_pos) RELATIVE Origin
GROUP Grating

COMPONENT GratingSlit1_5 = Slit(xwidth=grating_w,yheight=5e-3)
 AT (2.0*grating_w + 2.0*grating_a, 0, grating_pos) RELATIVE Origin
GROUP Grating

/* //THIS IS DOUBLE SLIT
COMPONENT GratingSlit2_1 = Slit(xwidth=grating_w,yheight=5e-3)
 AT (-0.5*grating_w - 0.5*grating_a, 0, grating_pos) RELATIVE Origin
GROUP Grating

COMPONENT GratingSlit2_2 = Slit(xwidth=grating_w,yheight=5e-3)
 AT (0.5*grating_w + 0.5*grating_a, 0, grating_pos) RELATIVE Origin
GROUP Grating */

/* //THIS IS SINGLE SLIT
COMPONENT GratingSlit3_1 = Slit(xwidth=grating_w,yheight=5e-3)
 AT (0, 0, grating_pos) RELATIVE Origin */

// DETECTOR
COMPONENT TOF_det = TOF_monitor(xwidth = 0.05, yheight = 0.05,
   nt=251, tmin=tlow, tmax=thigh, filename="TOF_det")
 AT (0, 0, detector_pos) RELATIVE Origin

FINALLY
%{
%}

/* The END token marks the instrument definition end */
END
```

D.2 Triangular coil component

Component code:

```
/*******************************************************************************
*
* McStas, neutron ray-tracing package
* Component: Pol_triafield
* Written by: Morten Sales, based on Pol_constBfield by Peter Christiansen
* Date: 2013
* Version: $Revision: 0.1 $
* Origin: Helmholtz-Zentrum Berlin
* Release: McStas 2.0
*
* Constant magnetic field in a isosceles triangular coil
* Rectangular box with constant B field along y-axis (up) in a isosceles triangle.
* There is a guide (or precession) field as well.
* It is along y in the entire rectangular box.
* A neutron hitting outside the box opening or the box sides is absorbed.
*
*      ________________
*     |        /\      |
*     | Bguide/  \Bguide |      x
*     |      /    \     |      ^
*     |     /      \    |      |
*     |    /   B    \   |      |-----> z
*     |   /   and    \  |
*     |  /   Bguide   \ |
*     | /              \|
*     |/________________\|
*
* The angle of the inclination of the triangular field boundary is given by
* the arctangent to xwidth/(0.5*zdepth)
*
* This component does NOT take gravity into account.
*
* Example: Pol_triafield(xwidth=0.1, yheight=0.1, zdepth=0.2, B=1e-3, Bguide=0.0)
*
* INPUT PARAMETERS:
*
* xwidth:      Width of opening [m].
* yheight:     Height of opening [m].
* zdepth:      zdepth of field [m].
* B:           Magnetic field along y-direction inside triangle [T]
* Bguide:      Magnetic field along y-direction inside entire box [T]
*******************************************************************************/

DEFINE COMPONENT Pol_triafield
SETTING PARAMETERS(xwidth, yheight, zdepth, B=0, Bguide=0)
OUTPUT PARAMETERS(omegaL, omegaLguide)
/* Neutron parameters: (x,y,z,vx,vy,vz,t,sx,sy,sz,p) */
```

```
48
49 SHARE
50 %{
51  double IntersectWall(double pos, double vel, double wallpos) {
52  /* Function to calculate where the neutron hit the wall */
53
54   if(vel==0)
55    return -1;
56   if(vel>0)
57    return (wallpos-pos)/vel;
58   else
59    return (-wallpos-pos)/vel;
60   }
61 %}
62
63 DECLARE
64 %{
65  /* Larmor frequency */
66  double omegaL = 0;
67  double omegaLguide = 0;
68 %}
69
70 INITIALIZE
71 %{
72  double velocity = 0, time = 0;
73
74  if ((xwidth<=0) || (yheight<=0) || (zdepth<=0)) {
75   fprintf(stderr, "Pol_filter: %s: Null or negative volume!\n"
76    "ERROR       (xwidth, yheight, zdepth). Exiting\n",
77    NAME_CURRENT_COMP);
78   exit(1);
79  }
80  omegaL    = -1.832472e8 * (B - Bguide); // B and Bguide is in Tesla
81  omegaLguide = -1.832472e8 * Bguide; // Bguide is in Tesla
82 %}
83
84 TRACE
85 %{
86 double deltaT, deltaTx, deltaTy, sx_in1, sz_in1, sx_in2, sz_in2,
87   iz1, iz2, denom1, denom2, deltaTtria;
88
89 PROP_Z0;
90 if (!inside_rectangle(x, y, xwidth, yheight))
91 ABSORB;
92
93 // Time spent in Bguide-field
94 deltaT = zdepth/vz;
95
96 // This calculates the intersections on the xz-plane
97 // between the neutron trajectory and the triangular field boundaries
98 // The neutron trajectory is given by the points
99 // (x,0,0) and (x+vx,0,vz)
```

```
100 // The first field boundary is given by the points
101 // (-xwidth/2,0,0) and ( xwidth/2, 0, zdepth/2)
102 // The second field boundary is given by the points
103 // (xwidth/2,0,zdepth/2) and (-xwidth/2,0,zdepth)
104 // iz1 and iz2 are the z-values for the intersection
105 denom1 = (-vz)*((-xwidth/2)-xwidth/2)-(x-(x+vx))*(-zdepth/2);
106 iz1    = ((-x*vz)*(-zdepth/2)-(-vz)*(-(-xwidth/2)*zdepth/2))/denom1;
107 denom2 = (-vz)*(xwidth/2-(-xwidth/2))-(x-(x+vx))*(zdepth/2-zdepth);
108 iz2    = ((-x*vz)*(zdepth/2-zdepth)-(-vz)*(zdepth/2*(-xwidth/2)-xwidth/2*zdepth))/
109 denom2;
110 // Time spent in triangular B-field
111 deltaTtria  = (iz2-iz1)/vz;
112
113 // check that track goes throgh without hitting the walls
114 if (!inside_rectangle(x+vx*deltaT, y+vy*deltaT, xwidth, yheight)) {
115
116  // Propagate to the wall and absorb
117  deltaTx = IntersectWall(x, vx, xwidth/2);
118  deltaTy = IntersectWall(y, vy, yheight/2);
119
120  if (deltaTx>=0 && deltaTx<deltaTy)
121       deltaT = deltaTx;
122  else
123       deltaT = deltaTy;
124
125  PROP_DT(deltaT);
126  ABSORB;
127 }
128
129 PROP_DT(deltaT);
130
131 // These are the incoming spin directions
132 sx_in1 = sx;
133 sz_in1 = sz;
134
135 // This calculates the spin rotation caused by the guide/precession field
136 sz_in2 = cos(omegaLguide*deltaT)*sz_in1 - sin(omegaLguide*deltaT)*sx_in1;
137 sx_in2 = sin(omegaLguide*deltaT)*sz_in1 + cos(omegaLguide*deltaT)*sx_in1;
138
139 // This calculated the spin rotation caused by the triangular field
140 sz = cos(omegaL*deltaTtria)*sz_in2 - sin(omegaL*deltaTtria)*sx_in2;
141 sx = sin(omegaL*deltaTtria)*sz_in2 + cos(omegaL*deltaTtria)*sx_in2;
142 %}
143
144 MCDISPLAY
145 %{
146   magnify("xy");
147   box(0, 0, 0, xwidth, yheight, zdepth);
148 %}
149
150 END
```

This thesis is dedicated to my wife and my daughter.
The former who has been there to support me from the beginning of the project to its end, and the latter who came just in time to see its completion.

Thank you,
Morten

References

[1] Andersson, R. et al. "Analysis of spin-echo small-angle neutron scattering measurements". In: *J. Appl. Crystallogr.* 41.5 (2008), pp. 868–885. URL: http://dx.doi.org/10.1107/S0021889808026770.

[2] Bouwman, W. G., Duif, C. P., and Gähler, R. "Spatial modulation of a neutron beam by Larmor precession". In: *Phys. B Condens. Matter* 404.17 (2009), pp. 2585–2589. URL: http://dx.doi.org/10.1016/j.physb.2009.06.052.

[3] Bouwman, W. G. et al. "Combined SANS-SESANS, from 1nm to 0.1mm in one instrument". In: *Phys. B Condens. Matter* 406.12 (2011), pp. 2357–2360. URL: http://dx.doi.org/10.1016/j.physb.2010.11.069.

[4] Bouwman, W. G. et al. "SESANS studies of colloid phase transitions, dairy products and polymer fibres". In: *Phys. B Condens. Matter* 350.1 (2004), pp. 140–146. URL: http://dx.doi.org/10.1016/j.physb.2004.04.013.

[5] Bragg, W. "The diffraction of short electromagnetic waves by a crystal". In: *Proceedings of the Cambridge Philosophical Society*. Vol. 17. 1913, pp. 43–57. URL: http://dx.doi.org/10.1016/b978-0-08-011999-1.50015-8.

[6] Brok, E. et al. “Experimental evidence for lamellar magnetism in hemo-ilmenite by polarized neutron scattering”. In: *Phys. Rev. B* 89.5 (2014), p. 054430. URL: http://dx.doi.org/10.1103/PhysRevB.89.054430.

[7] Coulter, K. et al. “Neutron polarization with a polarized 3He spin filter”. In: *Nucl. Instruments Methods Phys. Res. Sect. A Accel. Spectrometers, Detect. Assoc. Equip.* 288.2-3 (1990), pp. 463–466. URL: http://dx.doi.org/10.1016/0168-9002(90)90139-W.

[8] Gähler, R. “A certain class of beam modulation techniques and its potential applications @ Sixth Conference on Polarised Neutrons in Condensed Matter Investigations (PNCMI 2006)”. In: *Phys. B Condens. Matter* 397.1-2 (2007), pp. 1–200. URL: http://dx.doi.org/10.1016/j.physb.2007.02.034.

[9] Grünzweig, C et al. “Design, fabrication, and characterization of diffraction gratings for neutron phase contrast imaging.” In: *Rev. Sci. Instrum.* 79.5 (2008), p. 053703. URL: http://dx.doi.org/10.1063/1.2930866.

[10] Hilger, A. et al. “Revealing microstructural inhomogeneities with dark-field neutron imaging”. In: *J. Appl. Phys.* 107.3 (2010), p. 036101. URL: http://dx.doi.org/10.1063/1.3298440.

[11] Hughes, D. J. and Burgy, M. T. “Reflection of Neutrons from Magnetized Mirrors”. In: *Phys. Rev.* 81.4 (1951), pp. 498–506. URL: http://dx.doi.org/10.1103/PhysRev.81.498.

[12] Kaestner, A., Lehmann, E., and Stampanoni, M. "Imaging and image processing in porous media research". In: *Adv. Water Resour.* 31.9 (2008), pp. 1174–1187. URL: http://dx.doi.org/10.1016/j.advwatres.2008.01.022.

[13] Keller, T. et al. "Features and performance of an NRSE spectrometer at BENSC". In: *Neutron News* 6.3 (1995), pp. 16–17. URL: http://dx.doi.org/10.1080/10448639508217694.

[14] Kinning, D. J. and Thomas, E. L. "Hard-sphere interactions between spherical domains in diblock copolymers". In: *Macromolecules* 17.9 (1984), pp. 1712–1718. URL: http://dx.doi.org/10.1021/ma00139a013.

[15] Knudsen, E. et al. "McStas-model of the delft SESANS". In: *Phys. B Condens. Matter* 406.12 (2011), pp. 2361–2364. URL: http://dx.doi.org/10.1016/j.physb.2010.11.060.

[16] Knudsen, E. et al. "Investigation of propagation algorithms for ray-tracing simulation of polarized neutrons". In: *J. Neutron Res.* 17.1 (2014), pp. 27–34. URL: http://dx.doi.org/10.3233/JNR-130003.

[17] Kraan, W., Rekveldt, M., and Por, P. "Adiabatic rotators for 3-D neutron polarisation analysis". In: *Nucl. Instruments Methods Phys. Res. Sect. A Accel. Spectrometers, Detect. Assoc. Equip.* 300.1 (1991), pp. 35–42. URL: http://dx.doi.org/10.1016/0168-9002(91)90703-S.

[18] Kraan, W. et al. "Test of adiabatic spin flippers for application at pulsed neutron sources". In: *Nucl. Instruments Methods Phys. Res. Sect. A Accel. Spectrometers, Detect. Assoc. Equip.* 510.3 (2003), pp. 334–345. URL: http://dx.doi.org/10.1016/S0168-9002(03)01812-6.

[19] Krist, T., Lartigue, C., and Mezei, F. "Transmission geometry supermirror neutron polarizer device". In: *Phys. B Condens. Matter* 180-181 (1992), pp. 1005–1006. URL: http://dx.doi.org/10.1016/0921-4526(92)90535-Z.

[20] Krouglov, T. et al. "Real-space interpretation of spin-echo small-angle neutron scattering". In: *J. Appl. Crystallogr.* 36.1 (2003), pp. 117–124. URL: http://dx.doi.org/10.1107/S0021889802020368.

[21] Lefmann, K. *Neutron Scattering: Theory, Instrumentation and Simulation*. 2011 ed. Nano- & eScience Centres, University of Copenhagen and ESS, 2015.

[22] Lefmann, K. and Nielsen, K. "McStas, a general software package for neutron ray-tracing simulations". In: *Neutron News* 10.3 (1999), pp. 20–23. URL: http://dx.doi.org/10.1080/10448639908233684.

[23] Lefmann, K. et al. "Simulation of a suite of generic long-pulse neutron instruments to optimize the time structure of the European Spallation Source". In: *Rev. Sci. Instrum.* 84.5 (2013), pp. 055106–055106–9. URL: http://dx.doi.org/10.1063/1.4803167.

[24] Lehmann, E. H., Hartmann, S., and Speidel, M. O. "Investigation of the content of ancient Tibetan metallic Buddha statues by means of neutron imaging methods". In: *Archaeometry* 52.3 (2009), pp. 416–428. URL: http://dx.doi.org/10.1111/j.1475-4754.2009.00488.x.

[25] Lehmann, E. H. et al. "Neutron imaging—detector options and practical results". In: *Nucl. Instruments Methods Phys. Res. Sect. A Accel. Spectrometers, Detect. Assoc. Equip.* 531.1-2 (2004), pp. 228–237. URL: http://dx.doi.org/10.1016/j.nima.2004.06.010.

[26] Manke, I. et al. “Three-dimensional imaging of magnetic domains”. In: *Nat. Commun.* 1.8 (2010), p. 125. URL: http://dx.doi.org/10.1038/ncomms1125.

[27] McStas. *Code for SEMSANS McStas instrument and necessary components*. 2014. URL: http://mcstas.org/download/share/McStas_code_SEMSANS.zip (visited on 2015).

[28] Mezei, F. “Neutron spin echo: A new concept in polarized thermal neutron techniques”. In: *Zeitschrift für Phys.* 255.2 (1972), pp. 146–160. URL: http://dx.doi.org/10.1007/BF01394523.

[29] Mezei, F., ed. *Neutron Spin Echo*. Vol. 128. Lecture Notes in Physics. Berlin, Heidelberg: Springer Berlin Heidelberg, 1980. URL: http://worldcat.org/oclc/59819226.

[30] Mezei, F., Pappas, C., and Gutberlet, T., eds. *Neutron Spin Echo Spectroscopy*. Vol. 601. Lecture Notes in Physics. Berlin, Heidelberg: Springer Berlin Heidelberg, 2003. URL: http://dx.doi.org/10.1007/3-540-45823-9.

[31] Mitchell, D. P. and Powers, N. P. “Bragg Reflection of Slow Neutrons”. In: *Physical Review, Letters to the editor* (1936).

[32] Pfeiffer, F. et al. “Neutron Phase Imaging and Tomography”. In: *Phys. Rev. Lett.* 96.21 (2006), p. 215505. URL: http://dx.doi.org/10.1103/PhysRevLett.96.215505.

[33] Plomp, J. “Spin-echo development for a time-of-flight neutron reflectometer”. PhD thesis. Technical University of Delft, 2009.

[34] Pynn, R. et al. "Neutron spin echo scattering angle measurement (SESAME)". In: *Rev. Sci. Instrum.* 76.5 (2005), p. 053902. URL: dx.doi.org/10.1063/1.1884187.

[35] Rekveldt, M. T. "Neutron Spin Echo Spectroscopy". In: ed. by Mezei, F., Pappas, C., and Gutberlet, T. Vol. 601. Lecture Notes in Physics. Berlin, Heidelberg: Springer Berlin Heidelberg, 2003. Chap. Elastic Neutron Scattering Measurements Using Larmor Precession of Polarized Neutrons, pp. 87–99. URL: http://dx.doi.org/10.1007/3-540-45823-9.

[36] Rekveldt, M. T. "Novel SANS instrument using Neutron Spin Echo". In: *Nucl. Instruments Methods Phys. Res. Sect. B Beam Interact. with Mater. Atoms* 114.3-4 (1996), pp. 366–370. URL: http://dx.doi.org/10.1016/0168-583X(96)00213-3.

[37] Rekveldt, M. T. et al. "Spin-echo small angle neutron scattering in Delft". In: *Rev. Sci. Instrum.* 76.3 (2005), p. 033901. URL: http://dx.doi.org/10.1063/1.1858579.

[38] Sales, M. et al. "A Pixel Based Approach for Spatially Resolved Analysis of Time-of-Flight Spin-Echo Modulated Scattering Data". In: *Journal of Applied Crystallography* (2015 (submitted)).

[39] Sales, M. et al. "Investigating time-of-flight spin-echo modulation for small-angle neutron scattering through experiments and simulation". In: *J. Appl. Crystallogr.* 48.1 (2015), pp. 92–96. URL: http://dx.doi.org/10.1107/S1600576714025916.

[40] Sales, M. et al. “Powder Diffractometers at Long-Pulsed Sources”. In: *J. Phys. Soc. Japan* 80.Suppl. B (2011). URL: http://dx.doi.org/10.1143/JPSJS.80SB.SB018.

[41] Sales, M. et al. “Wavelength-Independent Constant Period Spin-Echo Modulated Small Angle Neutron Scattering”. In: (2015 (to be submitted)).

[42] Šaroun, J. “Evaluation of double-crystal SANS data influenced by multiple scattering”. In: *J. Appl. Crystallogr.* 33.3 (2000), pp. 824–828. URL: http://dx.doi.org/10.1107/S0021889899013370.

[43] Strobl, M. “General solution for quantitative dark-field contrast imaging with grating interferometers.” In: *Sci. Rep.* 4 (2014), p. 7243. URL: http://dx.doi.org/10.1038/srep07243.

[44] Strobl, M., Udby, L., and Carlsen, H. *Odin Instrument Proposal for the ESS, 1-3 Description of Instrument Concept and Performance*. 2012. URL: http://europeanspallationsource.se/sites/default/files/odin_instrument_proposal_1-3_description_of_instrument_concept_and_performance.pdf (visited on 2015).

[45] Strobl, M et al. “Advances in neutron radiography and tomography”. In: *J. Phys. D. Appl. Phys.* 42.24 (2009), p. 243001. URL: http://dx.doi.org/10.1088/0022-3727/42/24/243001.

[46] Strobl, M. et al. “Neutron Dark-Field Tomography”. In: *Phys. Rev. Lett.* 101.12 (2008), p. 123902. URL: http://dx.doi.org/10.1103/PhysRevLett.101.123902.

[47] Strobl, M. et al. "TOF-SEMSANS – Time-of-flight spin-echo modulated small-angle neutron scattering". In: *J. Appl. Phys.* 112.1 (2012), p. 014503. URL: http://dx.doi.org/10.1063/1.4730775.

[48] Strobl, M. et al. "Using a grating analyser for SEMSANS investigations in the very small angle range". In: *Phys. B Condens. Matter* 407.21 (2012), pp. 4132–4135. URL: http://dx.doi.org/10.1016/j.physb.2012.06.036.

[49] Strobl, M. et al. "Quantitative Neutron Dark-field Imaging through Spin-Echo Interferometry." In: *Sci. Rep.* 5 (2015), p. 16576. URL: http://dx.doi.org/10.1038/srep16576.

[50] Svergun, D. I. and Feigin, L. A. *Structure analysis by small-angle x-ray and neutron scattering*. Ed. by Taylor, G. W. New York: Plenum Press, 1987. URL: http://worldcat.org/oclc/16680922.

[51] Tremsin, A. S. "High resolution neutron counting detectors with microchannel plates and their applications in neutron radiography, diffraction and resonance absorption imaging". In: *Neutron News* 23.4 (2012), pp. 35–38. URL: http://dx.doi.org/10.1080/10448632.2012.725341.

[52] Tremsin, A. et al. "Optimization of high count rate event counting detector with Microchannel Plates and quad Timepix readout". In: *Nucl. Instruments Methods Phys. Res. Sect. A Accel. Spectrometers, Detect. Assoc. Equip.* 787 (2015), pp. 20–25. URL: http://dx.doi.org/10.1016/j.nima.2014.10.047.

[53] Weitkamp, T. et al. "X-ray phase imaging with a grating interferometer". In: *Opt. Express* 13.16 (2005), p. 6296. URL: http://dx.doi.org/10.1364/OPEX.13.006296.

[54] Well, A. van. "Double-disk chopper for neutron time-of-flight experiments". In: *Phys. B Condens. Matter* 180-181 (1992), pp. 959–961. URL: http://dx.doi.org/10.1016/0921-4526(92)90521-S.

[55] Willendrup, P. et al. *User and Programmers Guide to the Neutron Ray-Tracing Package McStas, version 2.1*. 2015. URL: http://www.mcstas.org/manual/ (visited on 2015).

[56] Willendrup, P. et al. "McStas: Past, present and future". In: *J. Neutron Res.* 17.1 (2014), pp. 35–43. URL: http://dx.doi.org/10.3233/JNR-130004.

[57] Williams, S. H. et al. "Detection system for microimaging with neutrons". In: *J. Instrum.* 7.02 (2012), P02014–P02014. URL: http://dx.doi.org/10.1088/1748-0221/7/02/P02014.